ABSTRACT

OVERCOMING CONVENTIONAL MODELING LIMITATIONS USING IMAGE- DRIVEN LATTICE-BOLTZMANN METHOD SIMULATIONS FOR BIOPHYSICAL APPLICATIONS

by
Olufemi E. Kadri

The challenges involved in modeling biological systems are significant and push the boundaries of conventional modeling. This is because biological systems are distinctly complex, and their emergent properties are results of the interplay of numerous components/processes. Unfortunately, conventional modeling approaches are often limited by their inability to capture all these complexities. By using *in vivo* data derived from biomedical imaging, image-based modeling is able to overcome this limitation.

In this work, a combination of imaging data with the Lattice-Boltzmann Method for computational fluid dynamics (CFD) is applied to tissue engineering and thrombogenesis. Using this approach, some of the unanswered questions in both application areas are resolved.

In the first application, numerical differences between two types of boundary conditions: "wall boundary condition" (WBC) and "periodic boundary condition" (PBC), which are commonly utilized for approximating shear stresses in tissue engineering scaffold simulations is investigated. Surface stresses in 3D scaffold reconstructions, obtained from high resolution microcomputed tomography images are calculated for both boundary condition types and compared with the actual whole scaffold values via image-based CFD simulations. It is found that, both boundary conditions follow the same *spatial* surface stress patterns as the whole scaffold simulations. However, they under-predict the

absolute stress values approximately by a factor of two. Moreover, it is found that the error grows with higher scaffold porosity. Additionally, it is found that the PBC always resulted in a lower error than the WBC.

In a second tissue engineering study, the dependence of culture time on the distribution and magnitude of fluid shear in tissue scaffolds cultured under flow perfusion is investigated. In the study, constructs are destructively evaluated with assays for cellularity and calcium deposition, imaged using μCT and reconstructed for CFD simulations. It is found that both the shear stress distributions within scaffolds consistently increase with culture time and correlate with increasing levels of mineralized tissues within the scaffold constructs as seen in calcium deposition data and μCT reconstructions.

In the thrombogenesis application, detailed analysis of time lapse microscopy images showing *yielding* of thrombi in live mouse microvasculature is performed. Using these images, image-based CFD modeling is performed to calculate the fluid-induced shear stresses imposed on the thrombi's surfaces by the surrounding blood flow. From the results, estimates of the yield stress (A critical parameter for quantifying the extent to which thrombi material can resist deformation and breakage) are obtained for different blood vessels. Further, it is shown that the yielding observed in thrombi occurs mostly in the outer shell region while the inner core remains intact. This suggests that the core material is different from the shell. To that end, we propose an alternative mechanism of thrombogenesis which could help explain this difference.

Overall, the findings from this work reveal that image-based modeling is a versatile approach which can be applied to different biomedical application areas while overcoming the difficulties associated with conventional modeling.

OVERCOMING CONVENTIONAL MODELING LIMITATIONS USING IMAGE-DRIVEN LATTICE-BOLTZMANN METHOD FOR BIOPHYSICAL APPLICATIONS

by
Olufemi E. Kadri

A Dissertation
Submitted to the
Faculty of
New Jersey Institute of Technology
In Partial Fulfilment of the Requirement for the Degree of
Doctor of Philosophy in Chemical Engineering

Department of Chemical and Materials Engineering

December 2018

APPROVAL PAGE

OVERCOMING CONVENTIONAL MODELING LIMITATIONS USING IMAGE-DRIVEN LATTICE BOLTZMANN-METHOD SIMULATIONS FOR BIOPHYSICAL APPLICATIONS

Olufemi E. Kadri

Dr. Roman S. Voronov, Dissertation Advisor — Date
Assistant Professor of Chemical Engineering, NJIT

Dr. Piero M. Armenante, Committee Member — Date
Distinguished Professor of Chemical Engineering, NJIT

Dr. Laurent Simon, Committee Member — Date
Associate Professor of Chemical Engineering, NJIT

Dr. Sagnik Basuray, Committee Member — Date
Assistant Professor of Chemical Engineering, NJIT

Dr. Gennady Gor, Committee Member — Date
Assistant Professor of Chemical Engineering, NJIT

Dr. Linda J. Cummings, Committee Member — Date
Professor of Mathematics, NJIT

BIOGRAPHICAL SKETCH

Author: Olufemi E. Kadri

Degree: Doctor of Philosophy

Date: December 2018

Undergraduate and Graduate Education:

- Doctor of Philosophy in Chemical Engineering,
  New Jersey Institute of Technology, Newark, NJ, 2018

- Master of Science in Chemical Process Engineering,
  University College London, London, UK, 2011

- Bachelor of Science in Chemical Engineering,
  University of Lagos, Lagos, Nigeria, 2006

Major: Chemical Engineering

Presentations and Publications:

Olufemi Kadri, Vishnu Deep Chandran, Surblyte Migle, Roman S Voronov. "Endothelial cells could be responsible for the observed core-and-shell thrombus architecture" (Under review).

Olufemi Kadri, Vishnu Deep Chandran, Surblyte Migle, Roman Voronov. "*In vivo* Measurement of Blood Clot Strength from Computational Fluid Dynamics based on Intravital Microscopy Images" (Under review).

Olufemi Kadri, Cortes Williams III, Vassilios Sikavitsas, Roman Voronov. "Numerical Accuracy Comparison of Two Boundary Conditions Commonly used to Approximate Shear Stress Distributions in Tissue Engineering Scaffolds Cultured under Flow Perfusion". *International Journal for Numerical Methods in Biomedical Engineering*, 2018. 34 (11): p. e3132.

Cortes Williams, Olufemi Kadri, Roman Voronov, Vassilios Sikavitsas. "Time-Dependent Shear Stress Distributions during Extended Flow Perfusion Culture of Bone Tissue Engineered Constructs". *Fluids*, 2018. 3 (2), 25.

Dimitrios Papavassiliou, Ngoc Pham, Olufemi Kadri, Roman Voronov. Chapter 23 – Lattice-Boltzmann Methods for Bioengineering Applications, in *Numerical Methods and Advanced Simulation in Biomechanics and Biological Processes*. 2018, London, UK: Academic Press. p. 415-429.

Olufemi Kadri, Roman Voronov, Vassilios Sikavitsas, Cortes Williams, Robert Shambaugh. "On the Numerical Validity of Commonly-Employed Scaffold Mimicks for Shear Stress and Flow Field Calculations in Tissue Engineering Models". Presented at the *American Institute of Chemical Engineering (AIChE) Annual Meeting,* Minneapolis, MN. 2017.

Olufemi Kadri, Roman Voronov, Vassilios I. Sikavitsas, Cortes Williams, Robert L. Shambaugh,2017. "Modeling the Micro-dynamic Environment of Tissue Scaffolds via Representative Volume and Full Domain Lattice-Boltzmann Method Simulations". Presented at the *American Physical Society (APS) Mid-Atlantic Meeting,* Newark NJ. 2017.

Vishnu Deep Chandran, Olufemi Kadri, and Roman Voronov. "Thrombus yield stress calculation from LBM based on intravital laser injury images in mice". Presented at the *Northeast Bioengineering Conference (NEBEC),* Newark NJ. 2017.

Vishnu Deep Chandran, Olufemi Kadri, Roman Voronov. "High performance Lattice-Boltzmann method yield-stress calculations based on intravital images of clot formation in live mice". *Bulletin of the American Physical Society*. 2017

This work is dedicated to my entire family and everyone out there who is committed to making the world a better place.

ACKNOWLEDGMENT

I would like to express my very deep gratitude to my Advisor, Dr. Roman Voronov, for his mentorship and support. His continuous guidance, motivation and patience were helpful at every stage of this PhD journey.

Additional thanks to Dr. Gennady Gor, Dr. Sagnik Basuray, Dr. Laurent Simon, Dr. Piero Armenante and Dr. Linda Cummings for their time and support as committee members.

I am also thankful for the financial support from the Department of Chemical and Materials Engineering, the Gustavus and Louise Pfeiffer Foundation and New Jersey Research Foundation. Special thanks to the University of Oklahoma Supercomputing Center for Education & Research (OSCER), Texas Advanced Computing Center (TACC) at the University of Texas at Austin, Blue Waters Super Computing cluster at the University of Illinois and NJIT Academic Research and Computing Systems (ARCS) for granting us access to their high-performance computing facilities.

I am grateful to our collaborators at the University of Oklahoma - Dr Cortes Williams and Prof. Vassilios Sikavitsas for providing us with micro-CT images of tissue scaffolds.

I want to sincerely thank Anh, Vishnu, Migle, Long, Vatsal, Leela, Vikram, Cheng, Akshay, David, Austin, Diomar. It’s been fun knowing and working with you guys.

Finally, very special thanks to my entire family (especially TKK2) for their unconditional love!

TABLE OF CONTENTS

TABLE OF CONTENTS
(Continued)

Chapter **Page**

TABLE OF CONTENTS
(Continued)

TABLE OF CONTENTS
(Continued)

LIST OF TABLES

LIST OF FIGURES

LIST OF FIGURES
(Continued)

LIST OF FIGURES
(Continued)

LIST OF FIGURES
(Continued)

CHAPTER 1

INTRODUCTION

Diseases have significant health and economic costs to societies. According to the CDC, 86% of the United States USD 2.6 trillion annual expenditure are for treating people with chronic and mental health conditions[1]. It is anticipated that this amount will rise to USD 42 trillion in 2030.[2] This situation is due to the high prevalence of diseases within the population and exorbitant costs of treatment. Unfortunately, current health care methods for disease treatment and management are inefficient because they are generalized and are not customized to the needs of individuals.

Hence, the life-sciences research community has witnessed a substantial push towards personalized medicine – the customization of prediction, prevention and treatment of illnesses to the unique needs of an individual's organism. In a seminal report[3] titled "The Case for Personalized Medicine", the Personalized Medicine Coalition – a group representing innovators, scientists, patients, providers and payers argued that: 1) Disease itself is *personal*; 2) Conversely, the currently-available medicine is *impersonal* and, therefore, is *ineffective*. 3) At the same time, medical technology is maturing to the point where it can become personalized. Concurrently, computational resources, powerful enough to handle the rising scale and complexity have become increasingly accessible as well. And finally, numerical algorithms are becoming mature enough to handle the large data with speed and efficiency. Combining the power of medical data and numerical techniques to develop *in silico* models is an attractive way to harness current resources.

Unfortunately, models developed using conventional approaches are not equipped to make the most of this opportunity.

1.1 Limitations OF Conventional Modeling

The challenges involved in modeling biological systems are significant and push the limits of conventional modeling approaches. This is because biological systems are distinctly complex, and their emergent properties are results of the interplay of numerous components/processes. Conventional modeling approaches are limited by: (i) their reliance on multiple oversimplifications (e.g., boundary conditions, coarse graining, unknown parameter estimation, etc.) which do not depict actual biological reality; (ii) their inability to mathematically describe all the simultaneously occurring complex processes such as inter-cellular signaling, cell mechanics, cell migration, nutrients/cell waste transport, biochemical interactions etc. These limitations are due to incomplete understanding of the biology and unknown modeling parameters. For example, a comprehensive model of thrombus formation under flow will have to incorporate - all reactions of the coagulation cascade, interactions within and between cells (red blood cells, platelets and white blood cells),[4] nonnewtonian flow regimes which range from creeping to turbulent flow,[5] interactions between cells and plasma, interactions between blood flow and vessel wall, as well as other hemodynamic considerations etc. This will be difficult to model, and the challenge is not only mathematical but also biological (particularly with respect to uncertainty arising from insufficient knowledge of the underlying mechanisms).

1.2 A Better Alternative: Image-based Modeling

In order to overcome the challenges discussed above, while taking advantage of high resolution experimental and clinical imaging data, image-based computational models have emerged as alternative with several key advantages. These types of models utilize digital geometries generated from actual high resolution clinical or experimental images for simulation. Computational models developed using this approach are physiologically realistic because they are derived from the subject's own real-time/*in vivo* anatomy and structural features. Thus, they can be used for simulating processes such as blood flow in the cardio-vascular system,[6-11] air flow in the respiratory system[11-16], material transport in the bone/brain[17-19], etc. under very realistic conditions and at multiple scales. A flow diagram for the image-based modeling approach is shown in **Figure 1.1.**

It is pertinent to state that image-based models also rely on physical and mathematical equations like their conventional counterparts. However, they are able to bypass the challenge of modeling the complex biological processes that limit conventional models. Yet, they are more realistic because they are derived from the individual subject's actual biological features. The use of imaging ensures accurate mapping between biological and computational domains by providing real time visualization of organisms, from which temporal and spatial distributions of biological information (e.g., imaging dyes that can bind to specific proteins) regulating their activities can be obtained. Many times, the choice of imaging method used for experimental/clinical applications is determined by factors such as cost, imaging time, adverse effects, type of obtained information (functional or structural), penetration depth and resolution. While the first three impose practical limitations, the last three are arguably more important from a modeling perspective.

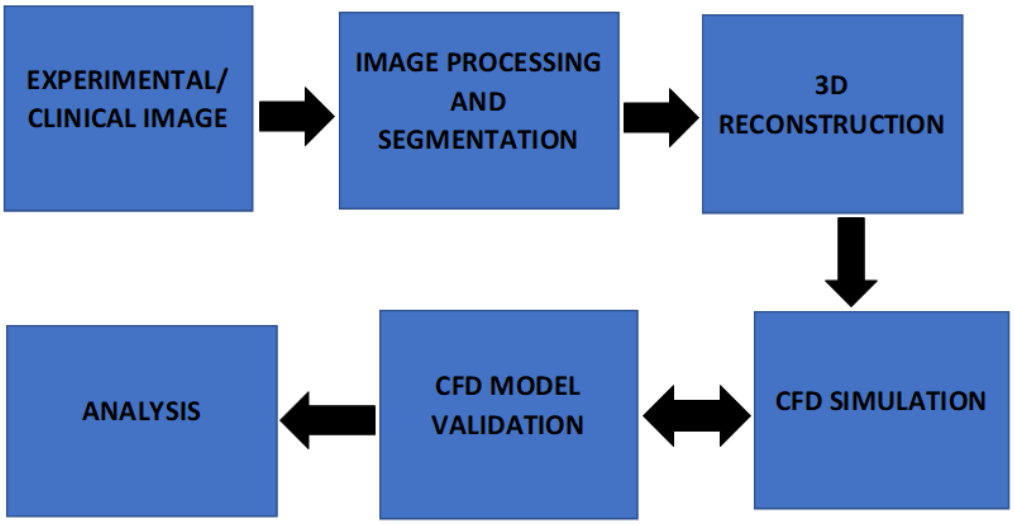

Figure 1.1 Image-based modeling methodology diagram. Medical image is first obtained. After which it is processed before being assembled into a 3D-reconstruction. Next, the reconstruction is fed into computational fluid dynamics (CFD) solver. After CFD simulation, the model is then validated against experimental or analytical data. Finally, simulation results are analyzed.

1.3 Biomedical Imaging and High Performance Computing Technology Advancements Enable Image-Based Modeling for Personalized Medicine

Current experimental and medical imaging techniques have advanced to the point of being able to provide high-resolution insights into the human body. Detailed images of major organs like the heart, lung, bone, brain in their physiological and diseased states can be obtained in real time (see **Figure 1.2**).

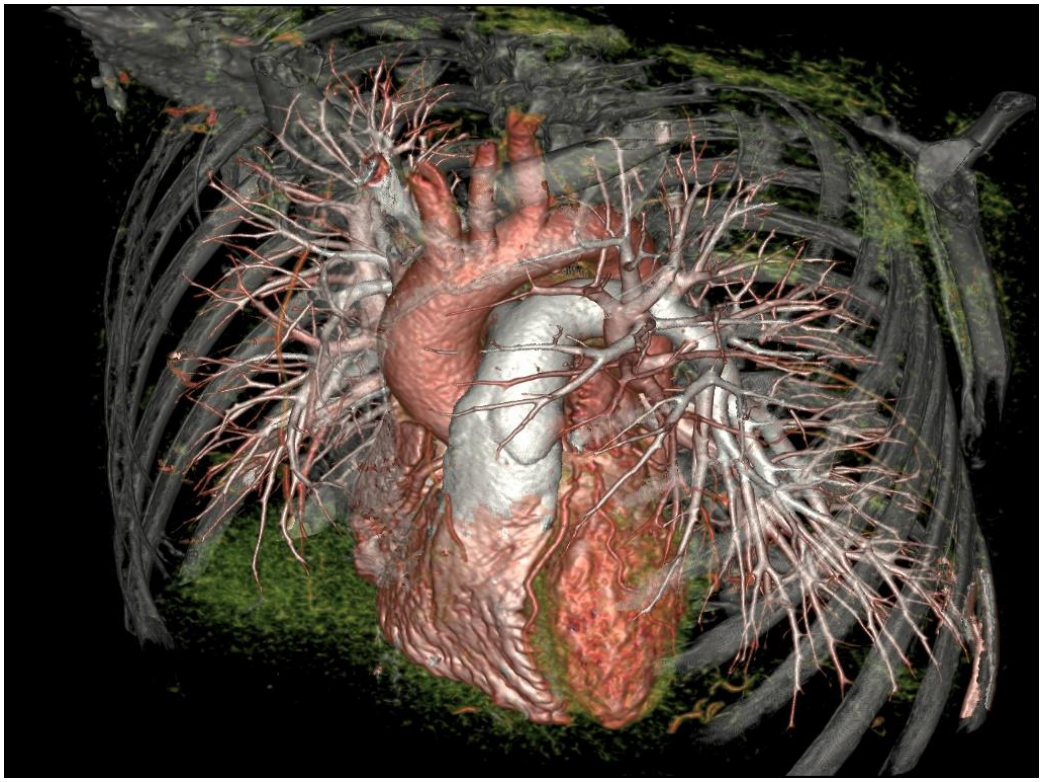

Figure 1.2 Low kV gated chest CT angiography (Image courtesy of GE Healthcare).

Similarly, computational power and speed have been consistently increasing over the years following Moore's law. Thus, computational resources, powerful enough to handle the rising scale and complexity, are becoming more accessible as well (see **Figure 1.3**). Also, numerical algorithms are becoming mature enough to handle the large data with greater speed and efficiency. Therefore, it is logical to leverage the merger of these data -gathering, -processing and numerical tools to develop realistic image-based models. The expectation is that image-based models will serve as one of the key platforms for using computerized technologies to facilitate and improve personalized medicine.

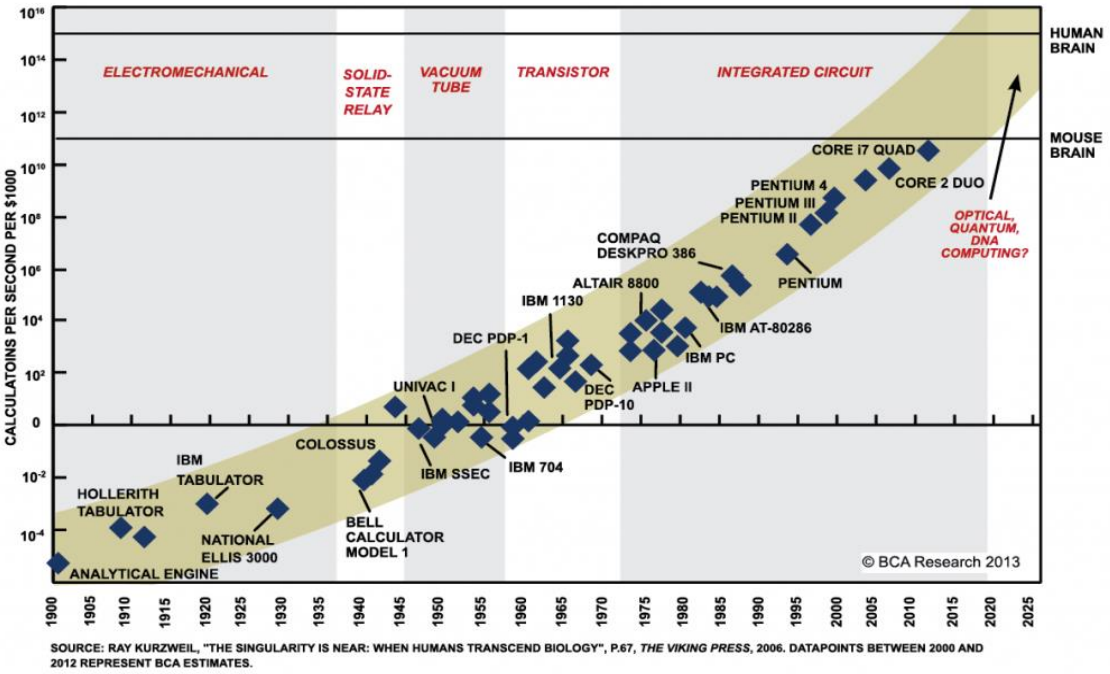

Figure 1.3 Cost of computing over time. *Source: [20]*

1.4 Research Scope and Outline

In order to accomplish the goals of image-based modeling, simulation methods that can efficiently handle the large image data and take advantage of high performance computing hardware and algorithms are required. To that end, Chapter 2 describes the computational methodology and algorithm used in this research. Chapters 3 and 4 present results of work done in resolving some unanswered questions in the area of bone tissue engineering. Chapter 5 presents results of work done in thrombus biomechanics using image-based modeling. In Chapter 6, a novel mechanism of thrombogenesis based on observations of the microscopy images used in Chapter 5 is presented.

Table 1.1 Overview of Imaging Methods and Applications

Ref.	Imaging method	Main application	Spatial resolution	Contrast agent/Imaging probe	Penetration depth	Limitations
[21]	Magnetic Resonance Imaging/MRI	Observing anatomical structure and physiological function	Millimeters	Gadolinium-diethylenetriamine pentaacetic acid	Whole body	Lengthy and noisy; Requires being still and conformity with breath-holding instructions to obtain best quality images
[22, 23]	Micro-MRI	Imaging anatomical structure	100 microns approx.	Gadolinium-diethylenetriamine pentaacetic acid	Whole body	Relatively expensive; Imaging time is long
[22, 24]	Functional MRI (fMRI)	Imaging brain blood flow	1mm approx.	Hemoglobin	Whole tissue	Relatively expensive; lower spatial resolution
[25, 26]	Computed Tomography/ CT	Imaging of lung and bone tumors	Millimeters	Iodine	Whole body	Uses high doses of ionizing radiation; Very expensive
[23, 27, 28]	Micro-CT	Imaging of bones	100 microns approx.	Iodine	Whole body	Poor contrast; Experimental outcomes can be altered due to use of high doses of radiation contrast agent
[29, 30]	Dual-Energy X-ray Absorptiometry (DEXA)	Quantifying bone mineral density (BMD)	1-3mm	None	Whole body	Not suitable for pregnant women due to possibility of fetus damage by radiation; it is a two dimensional measurement
[30-33]	Quantitative Computed Tomography (QCT)	Measuring BMD	41 microns	Hexabrix; Barium	Whole body	Uses fairly high dose of radiation

Overview of Imaging Methods and Applications (Continued)

[34, 35]	High Resolution Computed Tomography (HR-CT)	Imaging lung parenchyma	40 microns approx.	Iodine	Whole body	Uses high dose of radiation; The contrast agents used can cause undesirable reactions in people with allergies.
[21, 22, 36]	Positron Emission Tomography/ PET	Metabolic imaging	1-2mm	Radiolabeled fluorodeoxy-glucose (FDG)	Up to a meter depth	Expensive to use due to: high costs of cyclotrons, which produce radioactive isotopes used in radioactive tracers for PET imaging;
[37]	Photo acoustic Tomography/ PAT	Imaging breast tumors and melanoma	700 microns approx.	Optical absorption	50 millimeters approx.	Limited imaging depth due to attenuation; Not capable of imaging gas cavities or lung tissues due to strong reflection of sound from gas-liquid or gas-solid interfaces.
[38, 39]	Optical Coherence Tomography (OCT)	Imaging of the retina	10 microns approx.	Optical scattering	1-3 millimeters	Limited penetration depth due to optical scattering;
[40-42]	Ultrasonography	Cardio-vascular imaging	300 microns approx.	Bubbles	60 millimeters	Imprecise: Quality of image depends on skill level of operator; Cannot be used to image through bone or gas.
[43]	Confocal microscopy	Imaging of cells/tissues	1-2 microns	Fluorescence proteins/dyes	0.2 millimeters approx.	Limited penetration depth; Photo bleaching of probes and photo toxicity of live samples is a challenge
[44]	Two-photon microscopy	Live imaging of cells/tissues	1-2 microns	Fluorescence proteins/dyes	0.5 millimeters approx.	Resolution is slightly lower; Two photon excitation is not characterized for all fluorophores
[45]	Photoacoustic Microscopy/PAM	In vivo micro-vascular imaging	15 microns approx.	Optical absorption	3 millimeters approx.	Ultrasonic attenuation limits imaging penetration depth

Overview of Imaging Methods and Applications (Continued)

[22, 46]	Atomic Force Microscopy	Measuring surface morphology of cells	20 nanometers	Intermolecular forces	Not Applicable	Limited imaging area; Limited vertical range; Scanning speed is low
[47-49]	Stimulated emission depletion microscopy (STED)	Imaging of at the cellular/sub-cellular scale	50 nanometers approx. (lateral)	Green Fluorescent Protein (GFP)	20 microns approx.	Photo bleaching can be a problem; Resolution is limited by intrinsic optical resolution, labeling density and size of fluorescent labels
[48, 50, 51]	Photo activated localization microscopy (PALM)	Imaging intra-cellular proteins	30nm approx.(lateral)	Organic fluorophores/ fluorescent protein	100nm approx.	Resolution is limited by intrinsic optical resolution, labeling density and size of fluorescent labels
[52, 53]	Lattice Light Sheet Microscopy	Imaging cellular proteins	Dithered mode-230 nm by 370 nm; SIM-150nm by 230nm	Fluorescent protein/dyes	Up to 100 microns	Image quality degrades with deeper tissue samples.Only good for transparent tissues
[54]	Optoacoustic Mesoscopy	Imaging skin tissues	3-30microns	None	3-5mm	Optical blurring can lead to loss of resolution in imaged tissue
[48, 55]	Stochastic optical reconstruction microscopy (STORM)	Imaging nanoscopic cellular structures/intra-cellular proteins	30 nanometers approx. (lateral)	Organic fluorophores/ fluorescent protein	100 nanometers approx.	Resolution is limited by intrinsic optical resolution, labeling density and size of fluorescent labels

CHAPTER 2

METHODS: Lattice-Boltzmann Method as a CFD Solver for Image-Based Models

Among classical and emerging computational (CFD) simulation techniques, the Lattice-Boltzmann Method (LBM) stands out for image-based modeling for two main reasons:

First, LBM is highly parallelizable on supercomputing platforms.[56] This advantage is important because image-based models use high resolution imaging (experimental or clinical) data which are often large; running simulations with computational domains generated using these data are computationally intensive. Hence, fast and large memory supercomputing clusters are required to achieve results within a "reasonable time". Secondly, LBM is capable of easily addressing the complicated boundaries and irregular domains encountered in modeling complex flows within biological systems. This is because LBM uses structured meshes for complex geometries, unlike classical CFD approaches which will rather utilize unstructured meshes. Other advantages of LBM over classical methods are - it uses a direct method based on first principles at the mesoscopic scale rather than modeling terms of the fluid flow governing equations at the macroscopic scale.[57, 58] Specifically, it is based on the solution of a discretized Boltzmann equation,[59-63] instead of solving the equations for momentum or energy transfer used by classical CFD techniques. Also, LBM is a versatile CFD method as demonstrated by its application areas (e.g., turbulence,[64] multi-phase flows,[65, 66]non-Newtonian flows,[67-69]flow through blood vessels,[6] lungs,[70] and porous

Some of the material presented in this section have been published in *Papavassiliou, D.V., Pham, N.H., Kadri, O.E., Voronov, R.S. Chapter 23 - Lattice Boltzmann Methods for Bioengineering Applications, in Numerical Methods and Advanced Simulation in Biomechanics and Biological Processes. 2018, Academic Press. p. 415-429.*

tissue scaffolds).[57, 71-78] Finally, LBM can be used to simulate fluid-wall interactions and mass transfer problems by coupling with other techniques such as fluid solid interaction (FSI) algorithms,[79-81] lattice-spring methods,[82] and particle tracking methods.[76, 83]

2.1 LBM Algorithm

LBM is a mesoscopic fluid simulation technique since it is based on a link between microscopic flow phenomena and the macroscopic fluid flow behavior. A typical LBM model applies a multi-speed model consisting of either a two- or a three-dimensional multi-component velocity. For example, a 3D configuration is commonly denoted as (D3Qn) and a 2D configuration would be denoted as (D2Qn).[59, 61] The number of velocity lattice vectors for 3D simulations can be 15, 19 or 27.

The LBM is based on the discrete Lattice-Boltzmann equation describing the evolution of a particle distribution function calculated in space and time[84] as follows:

$$\underbrace{f_i(\vec{x}+\vec{e}_i\Delta t, t+\Delta t) = f_i(\vec{x},t)}_{STREAMING} + \underbrace{\Omega_i(\vec{x},t)}_{COLLISION} \pm \underbrace{ff_i}_{FORCING} \tag{2.1}$$

where $\vec{x}$ is the position vector, t is time, Δt is the time step, $\vec{e}$ is the unit velocity vector along direction i, Ω is the collision operator, ff is the forcing factor and the subscript 'i' is the lattice direction index. The terms on the right and left hand sides of Equation (2.1) are the three steps of the LBM algorithm. First is the streaming step, when the fluid flows from one node location to another along direction i, then is the collision step and finally the forcing step, representing body forces acting on the fluid. At time t, during the streaming step the rest component f_0 remains at the center of the face-centered cubic lattice, while the

6 Class I components (f_i, i = 1, … ,6) move at time $t+\Delta t$ to new positions at the nearest neighboring nodes, and the Class II components (f_i, i = 7, …, n-1) move along the diagonals towards corners of the cubic lattice (See **Figure 2.1**). To restore any fluid that distributes in solid matrix nodes as a result of streaming, the bounce-back boundary conditions are then applied. In the next algorithmic step, the fluid relaxes to equilibrium by applying collision rules. The collision operator has been a subject of intense research, and several collision models have been proposed. The most common is the approximation according to single- relaxation-time (SRT) Bhatnagar, Gross and Krook, which is known as the BGK approximation.[85, 86] The BGK collision operator, Ω is given as:

$$\Omega_i(\vec{x},t) = -\frac{1}{\tau}(f_i - f_i^{eq}) \tag{2.2}$$

τ is relaxation time and is the time scale that is characteristic of the relaxation of the local particle distribution function towards equilibrium. The relaxation time is the parameter that incorporates the kinematic viscosity of the fluid (In lattice units), ν in the computations as:

$$\nu = \frac{1}{3}\left(\tau - \frac{1}{2}\right) \tag{2.3}$$

From Equation (2.3), it is obvious that numerical stability issues can arise as $\tau \to 1/2$ since viscosity must be positive and non-zero. Therefore, it is always desirable that τ >> 0.5. However, caution must also be taken because a very high value of τ will make the simulation take longer to converge. Another approach to resolving the problem of possible numerical instability is to use a multiple-relaxation-time (MRT) LBM model. Unfortunately, MRT LBM models require significantly more computation time than SRT

types. The SRT LBM model is used in this work. Details on MRT LBM models are given in the works of Du and Shi,[87] and Perumal and Dass.[58]

The equilibrium particle distribution, f^{eq}, is given by[60]

$$f_i^{eq}(\vec{x}) = w_i \rho(\vec{x}) \left[1 + 3\frac{\vec{e}_i \cdot \vec{U}}{c^2} + 9\frac{(\vec{e}_i \cdot \vec{U})^2}{c^4} - \frac{3}{2}\frac{\vec{U}^2}{c^2} \right] \tag{2.4}$$

where $c=\Delta x/\Delta t$ is the lattice speed, Δx is the lattice constant, w is a lattice specific weighing factor, ρ is local density and U is the macroscopic fluid velocity. For a D3Q15 discretization, the weighting factors are $w_0 = 2/9$, $w_{1\text{-}6} = 1/9$, $w_{7\text{-}14} = 1/72$.[88] For a D3Q19 discretization, the weighting factors are $w_0 = 1/3$, $w_{1\text{-}6} = 1/18$, and $w_{7\text{-}18} = 1/36$.

In the last step of the algorithm (the forcing step), body forces acting on the fluid such as electromagnetic forces can be applied as well as the pressure drop across the domain. Pressure drop is specified by adding the forcing factor, *ff*, to the components of the fluid particle distribution function that move in the positive streamwise direction and by subtracting it from those moving in the opposite direction. The fraction of the forcing factor applied to each component of the particle probability function can be determined, for example as described in Noble et al.[89]

At the end of the computational steps, the density of the fluid can be calculated using:

$$\rho = \sum_{i=0}^{n} f_i \tag{2.5}$$

The macroscopic velocity of the fluid at each computational mesh point is calculated from the conservation of momentum equation, which is as follows:

$$\rho\vec{U} = \sum_{i=0}^{n} f_i \vec{e}_i \tag{2.6}$$

n is the number of possible directions that the fluid particles are permitted to move. Simulations can be carried out at steady state, or in a transient manner.

The LBM algorithm is summarized as:

a) Initialize ρ, *U*, f_i and f_i^{eq}

b) Streaming: Move $f_i \rightarrow f_i^{temp}$ in the direction of $\vec{e}_i$

c) Compute ρ and *U from* f_i^{temp} using Equations (2.5) and (2.6)

d) Compute f_i^{eq} from Equation (2.4)

e) In the collision step, update the value of f_i using (2.1)

f) Repeat steps (b) to (e) until convergence.

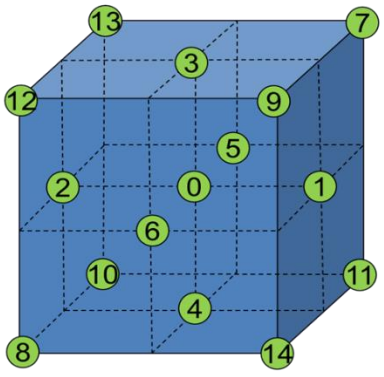

Figure 2.1 A typical D3Q15 computational cell for LBM simulations. The position 0 is the fluid particle rest position, while the 14 nodes shown on the figure designate the directions to which the particle probability function "streams" in each time step. *Source: [57]*

2.2 LBM Boundary Conditions

Boundary conditions (BCs) are pivotal to the numerical stability and accuracy of any CFD technique. For fluid flow problems solved with classical CFD approaches, the BCs are expressed using macroscopic variables, such as pressure or velocity. However, in the LBM frame, the governing equations are given in terms of particle distribution functions. Therefore, the macroscopic BCs have to be transformed to the mesoscopic frame and formulated for particle distribution functions. In the streaming step of the LBM algorithm, distribution functions can be determined for all grid nodes, except those located on boundary nodes. In **Figure 2.2,** the distribution functions on boundary nodes for a three-dimensional channel in the x-y plane is shown. According to this figure, for boundary nodes, some of the distribution functions move out of the computational domain (solid arrows) while others point into the fluid domain (dashed arrows). Since there are no grid nodes outside of the fluid domain, distribution functions coming into the boundary nodes cannot be determined and are unknown. In **Figure 2.2**, solid arrows represent known distribution functions while dashed arrows depict unknown distribution functions on different sides of the domain. Imposing the right BC can help calculate the unknowns. One of the simplest and the most convenient BC in CFD problems is the periodic BC. In implementing this condition, the solid walls are eliminated and a small part of an infinite system, having a periodically repeating behavior is considered. Therefore, in LBM, unknown boundary distribution functions at each side of the computational domain are determined by equating them with known distribution functions from the opposite side of the domain. For example, in **Figure 2.2**:

f_3 (top wall) = f_3 (bottom wall); f_{10} (inlet) = f_{10} (outlet)

f_7 (top wall) = f_7 (bottom wall); f_2 (inlet) = f_2 (outlet)

f_{10} (top wall) = f_{10} (bottom wall); f_{18} (inlet) = f_{18} (outlet)

f_{11} (top wall) = f_{11} (bottom wall); f_{16} (inlet) = f_{16} (outlet)

f_{13} (top wall) = f_{13} (bottom wall); f_8 (inlet) = f_8 (outlet)

Also, no-slip conditions on solid boundaries are implemented using Bounce-back BCs. The idea of the bounce back is that when a fluid particle (depicted by distribution function) encounters a solid boundary, it scatters back into the fluid along with its incoming direction. Hence, unknown distribution functions outside the fluid domain are replaced with their known opposite functions. i.e. $f_{-i}\left(x, t+\Delta t\right) = f_i\left(x, t_+\right)$.

where -*i* depicts opposite direction.

In **Figure 2.2** for example,

f_3 (top wall) = f_4 (top wall); f_{10} (inlet) = f_9 (inlet)

f_7 (top wall) = f_8 (top wall); f_2 (inlet) = f_1 (inlet)

f_{10} (top wall) = f_9 (top wall); f_{18} (inlet) = f_{15} (inlet)

f_{11} (top wall) = f_{14} (top wall); f_{16} (inlet) = f_{17} (inlet)

f_{13} (top wall) = f_{12} (top wall); f_8 (inlet) = f_7 (inlet)

Similar expressions can be written for the bottom wall and outlet.

Additional details regarding LBM BC types and their implementations are given in refs.[90-92]

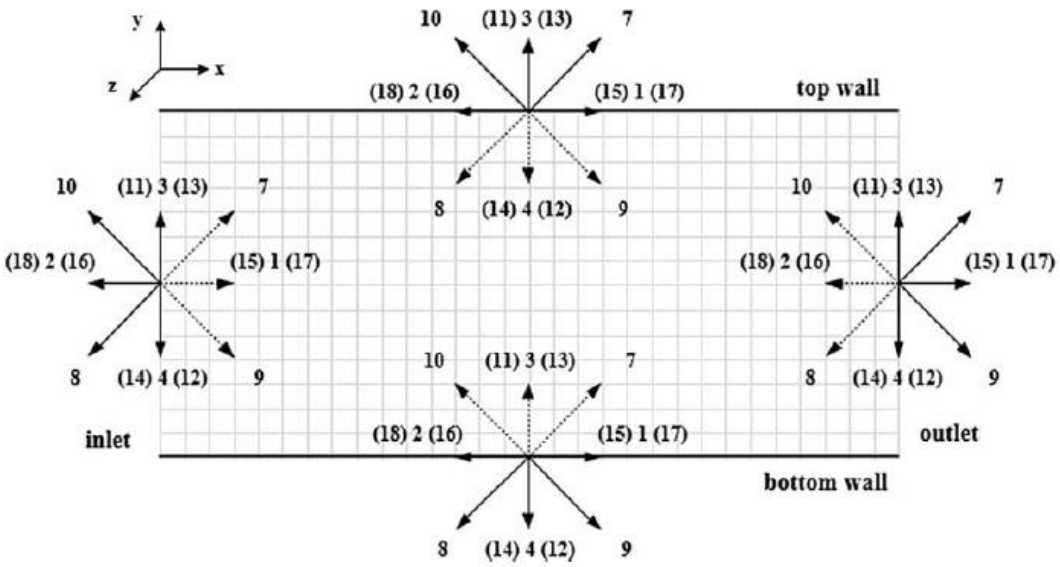

Figure 2.2 Description of known (solid arrows) and unknown (dashed arrows) distribution functions in x-y plane of a 3D channel. Image is shown for a D3Q19 lattice. *Source*: [93]

2.3 Algorithm Parallelization

Computationally, LBM is very attractive due to its effective and inherently parallelizable numerical algorithm.[57] The LBM solver used in this work is an in-house Fortran 90 code that is parallelized using Message Passing Interface (MPI). The parallelization technique is based on the one implemented by Voronov[94] where each MPI process works on a portion of the problem (data parallelism), while keeping a "ghost" copy of its nearest neighbor's boundaries for implementation of boundary conditions. Typically, in parallel implementations of LBM, the MPI computational domain is decomposed using one of either: "slice (1-D), box (2D), and cube (3D)" partitioning scheme or "recursive bisection" techniques, although other approaches such as the "cell based" methods have also been proposed.[56] In this work, an algorithm that allows for the program to choose between the slice (1-D), the box (2D) and the cube (3D) partitioning schemes depending on the problem

dimensions, such that the load balance is optimized by this choice is implemented. **Figure 2.3** illustrates the "box" partitioning scheme as an example of MPI domain decomposition.

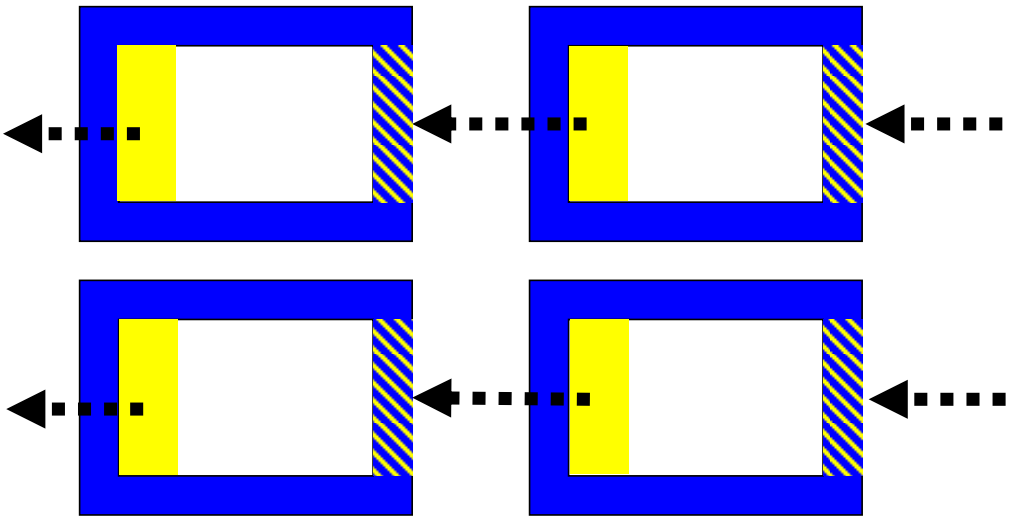

Figure 2.3 Example of MPI parallelization in 2D and four MPI processes. *Source: [94]*

In **Figure 2.3**, the problem is initially divided into four subdomains, with each one to be solved by one of the four MPI processes. Each block in the figure represents the part of the 2D, XY domain assigned to each of the four MPI processes. The white part of the blocks indicates nodes of the computational mesh that are local to each MPI process and can be updated by the LBM calculation within that MPI process. The solid blue color indicates the part of the computational mesh that is on the boundary of each of the four subdomains, the values on these nodes cannot be updated without MPI communication between the subdomains. These are referred to as "ghost" nodes and they require information from their nearest neighbors, either in the horizontal or vertical direction. Yellow and shaded colors show MPI communication taking place in the horizontal X direction: shaded "ghost" cells are updated from right to left. The data for the

computational mesh nodes that reside in the yellow area are passed to the subdomain neighbor to the left (as indicated by the black, dashed arrows). All the "ghost" nodes are then updated from left to right, such that all the blue "ghost" nodes become shades (i.e., updated with the most current values from the neighboring MPI process). After all the "ghost" nodes have been updated in the horizontal direction, the procedure is repeated in the vertical direction (up-down and down-up).

Speedup is a concept used in parallel computing to describe how much a parallel algorithm is faster than its corresponding non-parallel algorithm. It is defined as:

$$Speedup_P = \frac{Non\,Parallel\,Execution\,Time_1}{Parallel\,Execution\,Time_P} \tag{2.7}$$

where p is the number of processes

The speedup graph of the parallelized LBM algorithm for different simulation lattice sizes are shown **in Figure 2.4**.

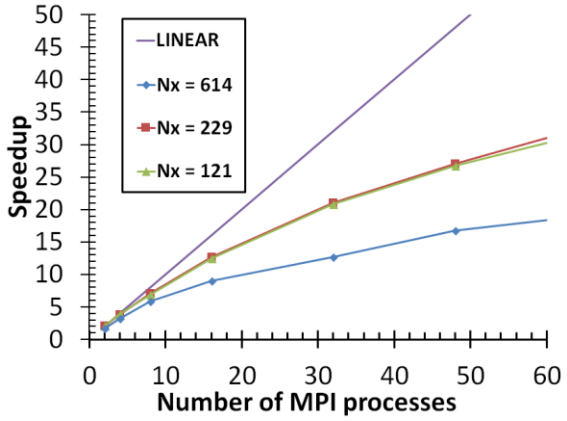

Figure 2.4 Speedup performance of LBM code versus number of MPI Processes for different simulation box sizes (N_X is number of nodes along one side of the cubic simulation domain), as measured on stampede supercomputer. The code was compiled with the Intel 17.0.4 compiler with no optimization options.

Linear speedup refers to when speedup increases linearly with number of MPI processes. When it occurs, it can be concluded that the code is scalable. **Figure 2.4** shows that the LBM code displays good scalability for many large problem sizes. This is not unexpected because the LBM algorithm is a memory-bound problem.[56, 95] Therefore, as the problem is broken up into smaller chunks among processes, its scalability improves. But, as the number of processes become very large, the communication between processes can dominate over computation. A typical flow chart for a single-phase flow MPI parallelized LBM algorithm is shown in **Figure 2.5**.

2.4 Stress Calculations

Shear stress is a critical parameter in many biological processes. For example, in arterial circulation, it provides information on where most vascular pathological activities originate;[96] while in tissue engineering, it is a metric for cell stimulation and tissue growth.[97] Hence, knowledge of this fluid dynamic parameter is useful for image-based modeling of many biophysical systems .

The fluid-induced shear stresses acting on solid surfaces can be obtained from the velocity fields calculated via LBM. In this work, stresses were estimated following a scheme suggested by Porter et al.[98] The total stress tensor σ is represented by a sum of the hydrostatic pressure p and viscous (deviatoric) stress tensor τ:

$$\sigma_{ij} = -p\delta_{ij} + \tau_{ij} \tag{2.8}$$

where δ_{ij} is the unit tensor, such that δ_{ij} is 1 if $i=j$ and 0 if $i \neq j$.

While the hydrostatic pressure is negligible, the latter stress is often of interest because it is responsible for shearing the solid surface. Also, since it describes how momentum is transported across the fluid layers due to velocity shear, it must be related to the deformation tensor:

$$D_{ij} = \frac{1}{2}\left(\nabla U + \nabla U^T\right) + \frac{1}{2}\left(\nabla U - \nabla U^T\right) \tag{2.9}$$

Also, this tensor can be decomposed into symmetric (rate of strain) and anti-symmetric (vorticity) parts. Furthermore, since fluid used in this work is assumed to be Newtonian, the viscous stress tensor depends only on the symmetric component of the deformation tensor. Hence, the shear stress at every location on solid is calculated using the following equation:

$$\underline{\underline{\sigma}} \approx \mu\left(\frac{1}{2}\right)\left(\nabla U + \nabla U^T\right) \tag{2.10}$$

where $\underline{\underline{\sigma}}$ is the shear stress tensor and U is local velocity vector.

Derivatives of the velocity field given in Equation (2.10) can be approximated numerically using finite difference methods. A centered finite difference method (Equations (2.11) – (2.13)) is shown here. The same can be done for partial derivatives of U_y and U_z. Following this, the symmetric strain matrices can be found by adding the 3 × 3 partials matrix for each field location to its own transpose.

$$\frac{\partial U_x(i,j,k)}{\partial x} = \frac{U_x\left(i+lu, j, k\right) - U_x\left(i-lu, j, k\right)}{2 \times lu} \tag{2.11}$$

$$\frac{\partial U_x(i,j,k)}{\partial y} = \frac{U_x(i,j+lu,k) - U_x(i,j-lu,k)}{2 \times lu} \tag{2.12}$$

$$\frac{\partial U_x(i,j,k)}{\partial z} = \frac{U_x(i,j,k+lu) - U_x(i,j,k-lu)}{2 \times lu} \tag{2.13}$$

where *lu* is the length of one side of an element in the LBM model.

Finally, eigenvalues of the symmetric matrix are obtained using the Jacobi method, and the largest absolute-value eigenvalue (i.e., largest principal component of the tensor) for each fluid voxel is used to determine the stresses.

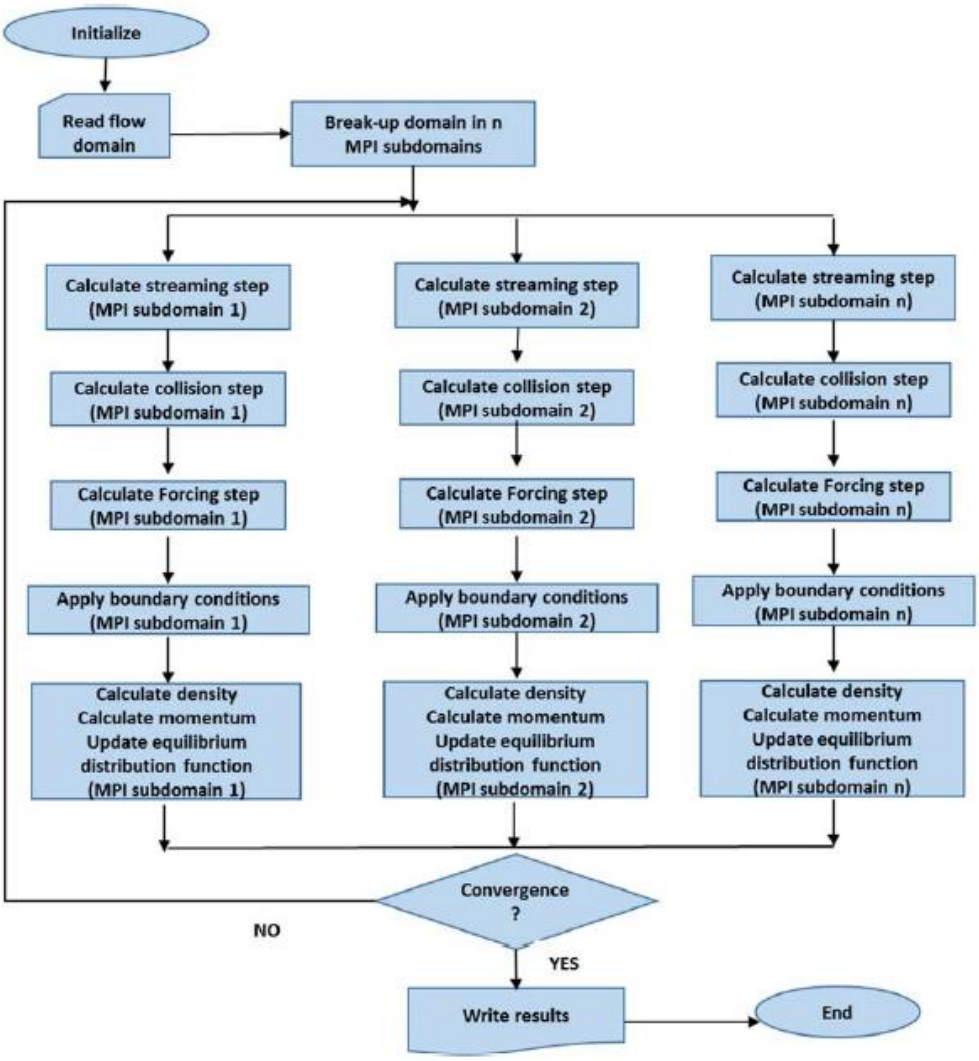

Figure 2.5 Flow chart of a typical lattice Boltzmann method algorithm for single-phase flow and MPI. *Source: [57]*

CHAPTER 3

APPLICATION I: NUMERICAL ACCURACY COMPARISON OF TWO BOUNDARY CONDITIONS COMMONLY USED TO APPROXIMATE SHEAR STRESS DISTRIBUTIONS IN TISSUE ENGINEERING SCAFFOLDS CULTURED UNDER FLOW PERFUSION

3.1 Abstract

Flow-induced shear stresses have been found to be a stimulatory factor in pre-osteoblastic cells seeded in 3D porous scaffolds and cultured under continuous flow perfusion. However, due to the complex internal structure of the scaffolds, whole scaffold calculations of the local shear forces are computationally-intensive. Instead, representative volume elements (RVEs), which are obtained by extracting smaller portions of the scaffold, are commonly used in literature without a numerical accuracy standard. Hence, the goal of this study is to examine how closely the whole scaffold simulations are approximated by the two types of boundary conditions used to enable the RVEs: "wall boundary condition" (WBC) and "periodic boundary condition" (PBC).

To that end, Lattice-Boltzmann Method fluid dynamics simulations were used to model the surface shear stresses in 3D scaffold reconstructions, obtained from high resolution microcomputed tomography images. It was found that despite the RVEs being sufficiently larger than six times the scaffold pore size (which is the only accuracy guideline found in literature), the stresses were still significantly under-predicted by both

---

Some of the material presented in this section have been published in *Kadri, O.E., Williams, C., Sikavitsas, V.I. and Voronov, R.S. "Numerical Accuracy Comparison of Two Boundary Conditions Commonly used to Approximate Shear Stress Distributions in Tissue Engineering Scaffolds Cultured under Flow Perfusion". International Journal for Numerical Methods in Biomedical Engineering.* ***34****(11): p. e3132.*

types of boundary conditions: between 20 and 80% average error, depending on the scaffold's porosity. Moreover, it was found that the error grew with higher porosity. This is likely due to the small pores dominating the flow field, and thereby negating the effects of the unrealistic boundary conditions, when the scaffold porosity is small. Finally, it was found that the PBC was always more accurate and computationally efficient than the WBC. Therefore, it is the recommended type of RVE.

3.2 Introduction

Incidences of bone disorders constitute a significant economic burden to societies globally. In the United States alone, over $213 billion is the total annual cost (direct and indirect) of treating the estimated 126.6 million people affected by musculoskeletal disorders.[99] Unfortunately, with an increasingly obese and ageing population, this trend is expected to continue further. Current approaches for replacing the damaged bone tissues include the use of bone grafts (i.e., autografts or allografts). However, these methods have several shortcomings, limited availability and risk of disease transmission.[100-102] To address those disadvantages, bone tissue engineering has emerged as an alternative regenerative strategy.

In bone tissue engineering, a combination of osteo-inductive biological factors, mesenchymal stem cells obtained from patients' own bone marrow and porous biodegradable scaffolds are used. Typically, the process involves seeding the cells within the 3D scaffolds, followed by culturing under flow in perfusion bioreactors. The flow is a necessary part of the culture, because the stimulatory shear that it imposes on the stem cells mimics the natural microenvironment in bone canaliculi.[103, 104] Moreover, it has been

shown to promote tissue regeneration.[97, 105-107] Thus, the applied shear stresses should be within the physiological range required for stimulation: 0.1 - 25 dynes/cm^2,[108-110] because excessive shear of 26-54 dynes/cm^2 can cause cell lysing and/or detachment from the scaffold.[111, 112]

Therefore, the ability to predict the shear stress distribution in different scaffold micro-architectures can provide insight into whether or not a particular scaffold design will promote tissue growth. Moreover, when used in conjunction with the latest advances in 3D microfabrication technologies, such predictive capabilities can be used to create optimized scaffold geometries. Unfortunately, however, the complex internal structure of the porous scaffolds makes estimation of the required shear stresses via experimental or analytical techniques impractical. Hence, computational fluid dynamics models, based on either idealized pore geometries [104, 106, 113-118] or actual scaffold images,[73, 74, 76, 98, 109, 119-127] are commonly utilized.

The latter is the more realistic approach since it is based on the actual microscopic pore structures, which are typically obtained via a 3D scanning technique such as micro-computed tomography (μCT). Yet, due to the computationally intensive nature of the scaffold reconstructions resulting from such high-resolution imaging, researchers are forced to resort to implementing approximations.[73, 74, 76, 98, 109, 119-127] For example, rectangular "representative volume elements" (RVE) are cut from whole scaffolds and implemented in conjunction with various boundary conditions along the artificially created periphery. Two common types of boundary conditions that are typically implemented for this purpose are the "wall boundary condition" (WBC)[106, 109, 116, 119-127] and the "periodic boundary condition" (PBC).[73, 74, 76, 98, 115, 117] In the

former case, the RVE is surrounded by solid walls in the non-flow directions, while the latter is an application of periodicity in all three dimensions.

Although these approaches save on computation time, it is not obvious how accurate the resulting shear stresses are, or which of the two boundary conditions yields the better results. Consequently, the RVE approach is commonly questioned by journal reviewers, as no standards or guidance regarding their use exist. We have found only one publication that investigated the accuracy of the RVE-WBC, as compared to the whole scaffold simulation.[119] Here, a guideline was provided stating that for scaffolds with a homogenous pore distribution *the domain size should be at least 6 times the average pore size*. However, this suggestion was made based on *average* wall stresses only, while in reality the *spatial distribution* of the stresses is also important to tissue growth. For example, the cells within the scaffold migrate around in a nonrandom manner,[128] are therefore more likely to experience stresses at some preferred locations. Furthermore, only scaffolds prepared using the same fabrication technique were studied, though two different materials were used in their manufacturing. Nonetheless, the scaffold's structure depends more on the fabrication method than it does on the material.[73-75] Moreover, just a single scaffold sample was used for each type of the material. Hence, a more thorough investigation of the RVEs' accuracy is warranted, especially given that no PBC studies were found at all.

Therefore, in this work we set out to quantify how the two relevant boundary conditions compare against each other, when applied to scaffolds manufactured using different fabrication methods (see **Figure 3.1**), and for a large number of samples with varying porosities.

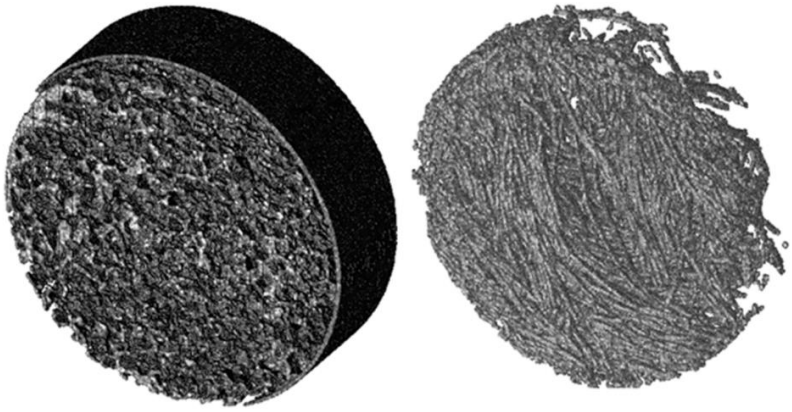

Figure 3.1 3D-reconstructions of the two scaffold architecture types used in this study. LEFT - Porous foam scaffold. RIGHT – Fiber Mesh scaffold. Dimensions are 1.61mm x 5.1mm x 5.1mm and 1.10mm x 5.1mm x 5.1mm for salt-leached and nonwoven fiber-mesh scaffolds, respectively.

To achieve this, an in-house Lattice-Boltzmann Method (LBM) code is used to simulate fluid flow through reconstructions of salt-leached foam and nonwoven fiber mesh scaffolds, all of which are imaged using μCT. The overall computational approach used in this work is summarized in **Figure 3.2**. Ultimately, the accuracy of the spatial stress distributions is reported for both the RVE-WBC and the RVE-PBC. Finally, a descriptive statistical analysis is used to demonstrate the accuracy and computational efficiency differences between the two RVE approaches.

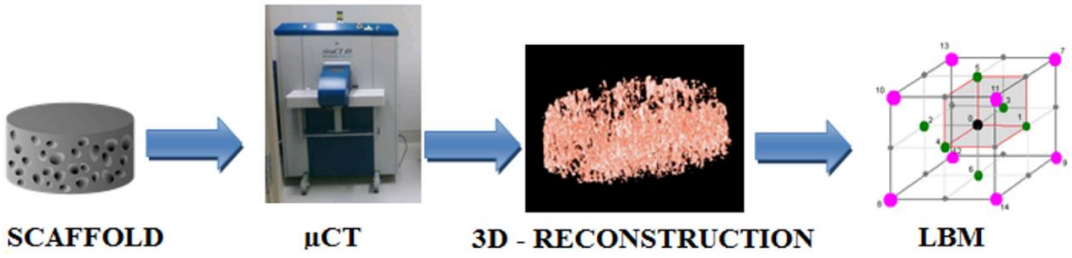

Figure 3.2 The image-based modeling methodology used in this work. The scaffolds were first manufactured, and then they were scanned using high-resolution μCT. Afterwards, their architecture was reconstructed virtually in 3D, and imported into the LBM fluid flow solver. Finally, the LBM simulation results were used to compute the shear stresses on the scaffold surfaces. *Source: [71]*

3.3 Materials and Methods

3.3.1 Scaffold Preparation and Imaging

Two types of porous scaffolds, salt-leached foam and nonwoven fiber scaffolds, were produced from poly-L-lactic acid using methods described in detail elsewhere.[73] The scaffolds were then scanned via μCT using a ScanCo VivaCT40 system (ScanCo Medical, Bassersdorf, Switzerland) to obtain 10μm resolution, 2D intensity image slices (see **Figure 3.3**) at the optimum settings of 88 μA (intensity) and 45 kV (energy). The acquired X-ray images were filtered for noise reduction and assembled into 3D-reconstructions of the scaffolds using a custom Matlab code (MathWorks Inc., Natick, MA). The scans were segmented using global thresholding. Threshold values were chosen such that the porosity of scaffolds from 3D-reconstructions were within 1% of experimentally calculated porosities. Experimental porosities were obtained by measuring the solid volume (mass of the scaffolds divided by the density of scaffold materials) and comparing with total scaffold volume (assuming a cylindrical scaffold) as reported in.[73, 74, 76]

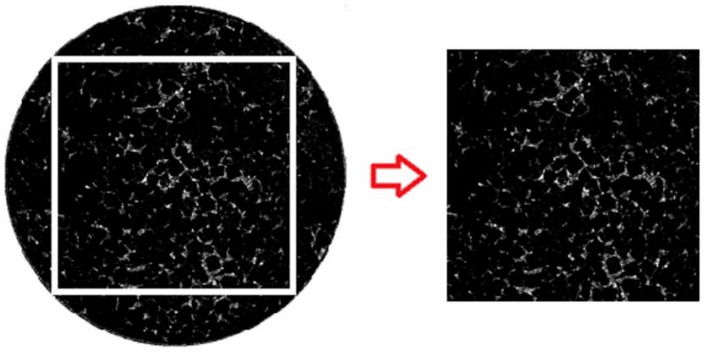

Figure 3.3 A two-dimensional analogy of how an RVE simulation domain is cut out of a whole scaffold μCT image. LEFT – A slice representative of a cross-section through a typical fiber mesh scaffold. The white box marks the largest rectangular area that could possibly be inscribed into the circular scaffold; RIGHT – the resulting RVE cutout from the rectangular region inscribed into the whole scaffold. Grayscale color is the X-ray radio-density of the scaffold material as imaged via μCT. *Source: [71]*

3.3.2 Simulation Domain and Boundary Conditions

For the non-RVE calculations, each simulation domain was composed of a *whole* scaffold placed inside of a pipe (see **Figure 3.4-A**). This is meant to mimic the cassette holder that typically fixes the scaffold in the perfusion bioreactors. The pipe's length was taken to be approximately ten times greater than the scaffold thickness, in order to avoid periodicity artifacts and ensure that a uniform parabolic profile is developed before flow reaches the scaffolds. Simulations were performed for a flow rate of 0.15 mL/min. This is considered a suitable flow rate for mechanical stimulation in many perfusion bioreactors.[97, 129]

For the RVE calculations, the simulation domain was obtained by extracting the *largest* rectangle that could possibly be inscribed into the circular whole scaffold (see **Figure 3.3-Left)**.

Generally, the size of the RVE (denoted below as 'L') is taken to satisfy the so-called 'separation of scales', $d < L$, where d is the average size of the porous media heterogeneity[130]. Specifically, the RVE domain size should be *at least 6 times the average pore size.*[119] We tried to stay well above this criterion, in order to maximize accuracy and examine the *best-case scenario* produced by the RVEs. Subsequently, the resulting domain sizes (see **Figure 3.3-Right**) were all between 8 - 14 times the scaffolds pore sizes, which is significantly greater than the suggested minimum for RVEs.[119]

For the RVE-PBC calculations, periodicity was applied in all three directions (see **Figure 3.4-B**) to approximate an infinite domain representing the full scaffold. On the other hand, for the RVE-WBC, the scaffold was surrounded by solid walls in the non-flow directions (see **Figure 3.4-C**). In addition, an entrance length equal to half of the scaffold's thickness in the flow direction was added, in order to stay consistent with the previous

analysis of this boundary condition type.[119] In both implementations, the total flow rate through the RVE was decreased proportionally to the cutout size, in order to compensate for the reduction in the cross-sectional area available to flow relative to the whole scaffold.

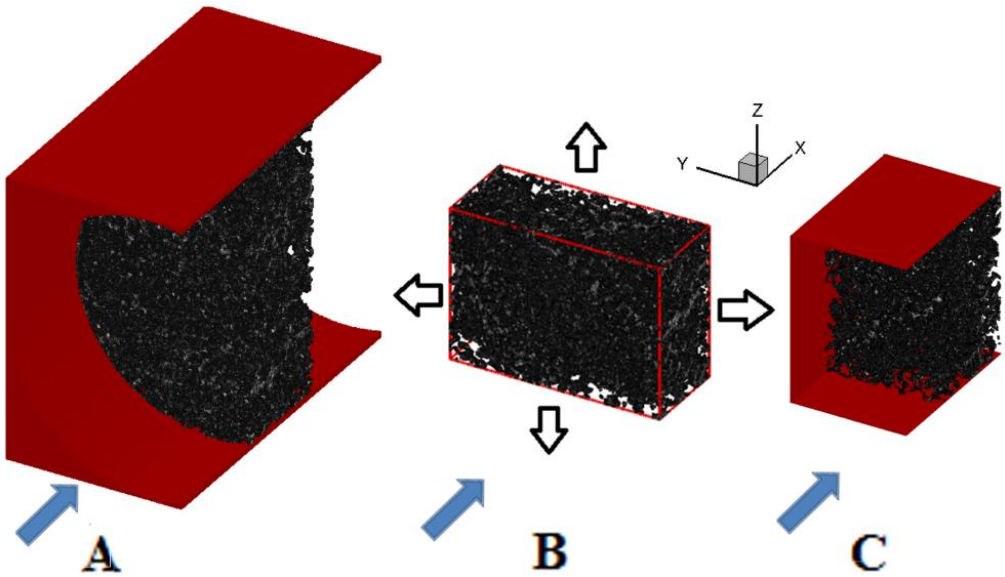

Figure 3.4 Simulation domain comparison between whole scaffold simulations and the RVEs. A – Cross-sectional view of the whole simulation domain (right half is omitted for clarity). The wall and the entrance length are shown in red. In all panes, the blue arrow is the flow direction; and the gray scale color is the X-ray radio-density of the scaffold material, as imaged via μCT. B - A representative RVE-PBC simulation domain. White arrows show the directions in which periodicity is applied. Note that periodicity is also applied in both x directions as well, but the arrows are omitted for clarity. C – A cross-sectional view of RVE-WBC simulation domain (right half is omitted for clarity). The wall and the entrance length are shown in red. *Source: [71]*

3.3.3 Fluid Flow Modeling

LBM was chosen for the present application, because it is especially appropriate for modeling pore-scale flow through porous media (such as scaffolds) due to the simplicity with which it handles complicated boundaries.[57, 72-74, 76, 94, 98, 131] This is because LBM uses structured meshes for complex geometries, unlike classical CFD approaches which will rather utilize unstructured meshes. Another advantage of LBM is that it uses a

direct method based on first principles at the mesoscopic scale rather than modeling terms of the fluid flow governing equations at the macroscopic scale. In addition, the LBM method has gained popularity within the scientific computing community because of the ease with which it can be parallelized on supercomputers.[56]

A previously developed custom-written, in-house code was used in this work.[6, 57, 73, 74, 76-78, 94, 132] The D3Q15 lattice [88] in conjunction with the single-relaxation time Bhatnagar, Gross and Krook[86] collision term approximation was used to perform simulations. The no-slip boundary condition was applied at solid faces using the "bounce-back" technique.[61] To take advantage of the inherent LBM parallelizability, domains were decomposed using message passing interface.[57, 94] Simulation convergence was defined as when average and highest velocities computed for the simulation domain vary by less than 0.01% for two consecutive time steps. The code has been validated for several flow cases for which analytical solutions are available: forced flow in a slit, flow in a pipe and flow through an infinite array of spheres.[74, 94]

3.3.4 Surface Stress Calculations and Error Analysis

Shear stress on the surface of the scaffolds was calculated following a scheme suggested in,[98] where the full shear stress tensor is calculated first, and then the maximum eigen value is evaluated using a Jacobi iteration technique. The cell culture media was assumed a Newtonian fluid, and the shear stresses at every location within the scaffolds were estimated using:

$$\underline{\underline{\sigma}} \approx \mu\left(\frac{1}{2}\right)\left(\nabla U + \nabla U^{T}\right) \tag{3.1}$$

where $\underline{\underline{\sigma}}$ is the shear stress tensor, and U is local velocity vector. The fluid dynamic viscosity was 0.01 g/(cm s), which is close to that of α-MEM supplemented with 10% FBS typically used in cell culturing experiments.[133] Velocity vectors used in calculations were derived for the specified flow rate. Computed shear stress values are the largest eigenvalues of $\underline{\underline{\sigma}}$. Stress maps generated using Tecplot 360 EX 2017 (Tecplot Inc., Bellevue, WA USA) were used to visualize localized shear stress values on the scaffolds. For the accuracy comparisons, the error at every fluid surface node was calculated as follows:

$$\varepsilon_t = 100\% * \left| \frac{True\ (Whole\ Scaffold) Stress - Approximated\ (RVE)\ Stress}{True\ (Whole\ Scaffold)\ Stress} \right| \quad (3.2)$$

where the 'True Stress' refers to the shear stress value obtained from the Whole scaffold simulations, while the 'Approximated Stress' is obtained from the RVE scaffold simulations.

3.4 Results

In order to compare the RVEs' performance relative to each other, as well as to that of the whole scaffold simulations, we performed image-based LBM modeling using a flow rate typically encountered during artificial tissue culturing conditions. **Figure 3.5** shows representative results for *whole* scaffolds of two different architectures: salt-leached foam (**Figure 3.5**-LEFT) and nonwoven fiber-mesh (**Figure 3.5**-RIGHT). These very computationally-intensive models exemplify the best stress estimates, because they are the most representative of the actual flow perfusion culturing conditions. However, they take

approximately 30,000-40,000 LBM steps to converge. Unfortunately, for high-resolution scaffold images (e.g., μCT), this can translate to weeks of waiting for results, even on a large supercomputer. The RVEs on the other hand, take only a fraction of that to converge, and therefore, have a higher computational efficiency.

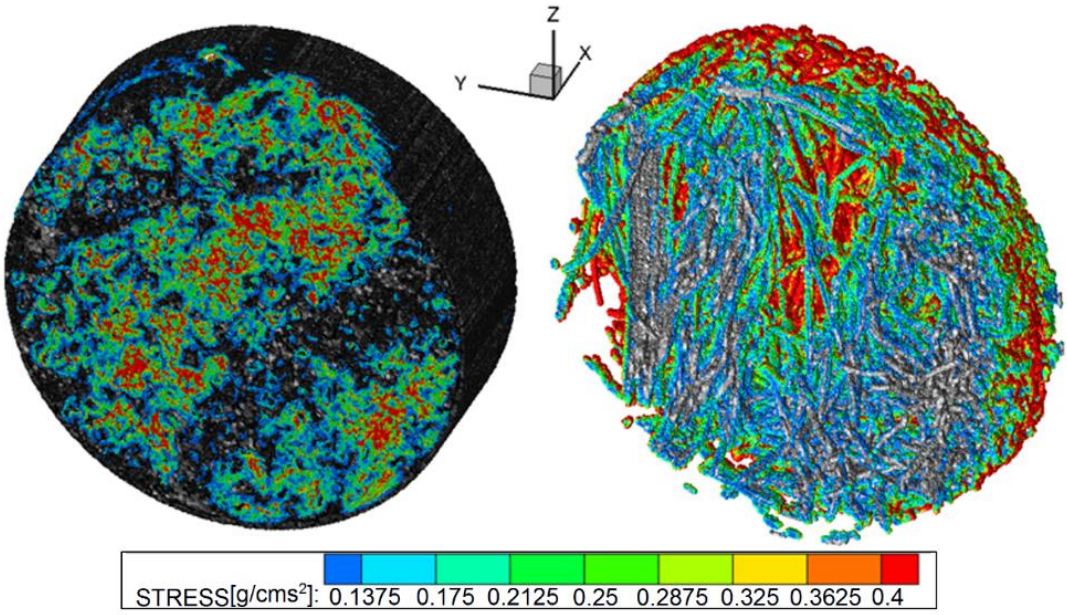

Figure 3.5 3D-reconstructions of the two scaffold types used in this study, with the surface stress maps (color) calculated from LBM overlaid on the *μCT* images (gray scale). LEFT - Porous foam scaffold. RIGHT – Fiber Mesh scaffold. The pipe surrounding the scaffold, and stress values below 0.1dynes/cm^2 are omitted for clarity. Dimensions are 1.61mm x 5.1mm x 5.1mm and 1.10mm x 5.1mm x 5.1mm for salt-leached and nonwoven fiber-mesh scaffolds, respectively. *Source: [71]*

This is shown in **Figure 3.6**, where both axes are normalized by the corresponding whole scaffold values. From this figure, it is apparent that the RVEs take roughly 3-6 times less LBM steps to converge, which translates into a significant waiting time reduction for the user. Hence, this makes the RVE approaches attractive, as long as some error can be tolerated.

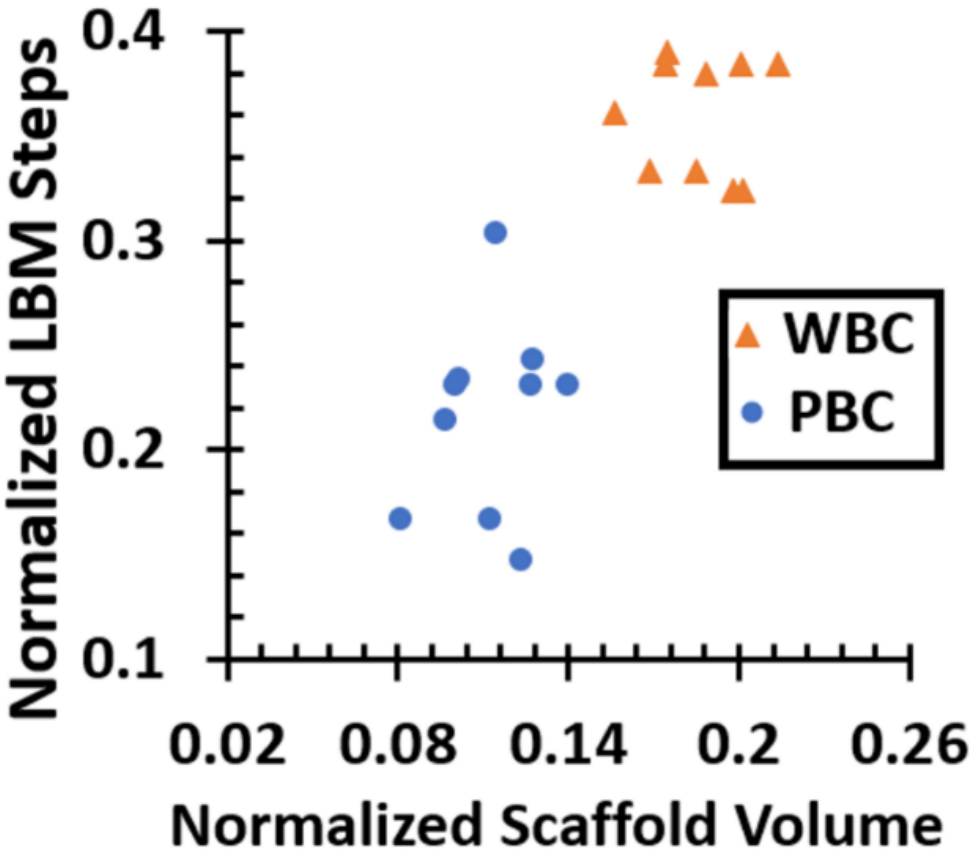

Figure 3.6 Total number of LBM steps required to reach convergence versus scaffold volume for RVE-PBC and RVE-WBC. The vertical and horizontal axes are normalized with respect to the whole scaffold values, respectively.

Next, we visualized the stresses produced by the RVEs, in order to gauge the amount of error incurred from their use. The first question we wanted to answer was whether the stress approximations provided by the RVEs follow a *spatial* pattern similar to that observed in the whole scaffold simulations. To that end, **Figure 3.7**-A & D shows stresses in RVE-equivalent domains cut out from the *whole* scaffold simulations in **Figure 3.5**. These are presented in order to provide a one-to-one comparison for the actual RVE-WBC and RVE-PBC cutouts shown in **Figure 3.7**-B & E and **Figure 3.7**-C & F, respectively. From **Figure 3.7**, it is apparent that the *spatial* stress patterns produced by

the RVEs are indeed very similar to those obtained from the whole scaffold simulations. However, the former stresses are significantly lower when compared with the latter.

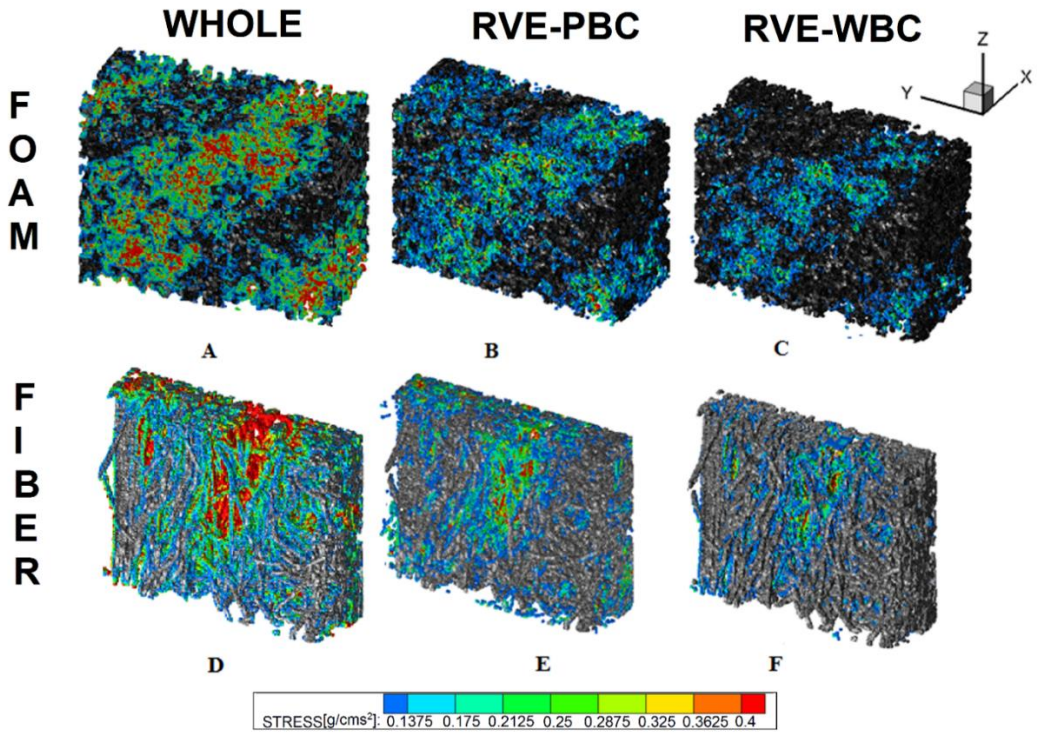

Figure 3.7 Surface *stress* maps overlays for the RVE-equivalents cutout from whole scaffold simulations and the two types of boundary conditions used for the RVEs. TOP ROW: Salt-leached Foam Scaffold. BOTTOM ROW: Nonwoven Fiber Mesh. LEFT COLUMN: RVE-equivalent volumes cutout from a *whole* scaffold models: CENTER COLUMN: RVE-PBCs. RIGHT COLUMN: RVE-WBCs. Dimensions are 1.61mm x 3.91mm x 2.81mm and 1.10mm x 3.79mm x 2.99mm for salt-leached and nonwoven fiber-mesh scaffolds, respectively. *Source: [71]*

Consequently, we used Equation (3.2) to quantify the spatial *accuracy* of the results produced by the RVE approximations. This was done by calculating the amount by which they deviate from the *true* stress values at every surface voxel of the scaffolds. For the purposes of this comparison, the whole scaffold stresses are considered to be the *true* values in the Equation (3.2) calculations, while the stresses produced by the RVE are used as the *approximated* values in the same equation. **Figure 3.8** is a 3D overlay of the resulting spatial error patterns in the two scaffold types from **Figure 3.7**. From left to right, the top

row shows the salt-leached foam RVE-PBC and WBC, respectively; while the bottom row shows the fiber-mesh RVEs, in the same order. It can be immediately observed from this figure that the bulk error is similar for both RVEs, varying roughly between 40 and 60% (for these particular samples). However, there is also a spatial trend in the error: in the case of the RVE-PBC it appears to *decrease* towards the cutout's periphery, while for the RVE-WBC the opposite is the case. This makes sense, given that the presence of the wall in the latter alters the flow field near the boundary. Therefore, there are significant differences in accuracies between the two RVEs; with the RVE-PBC yielding the more superior results.

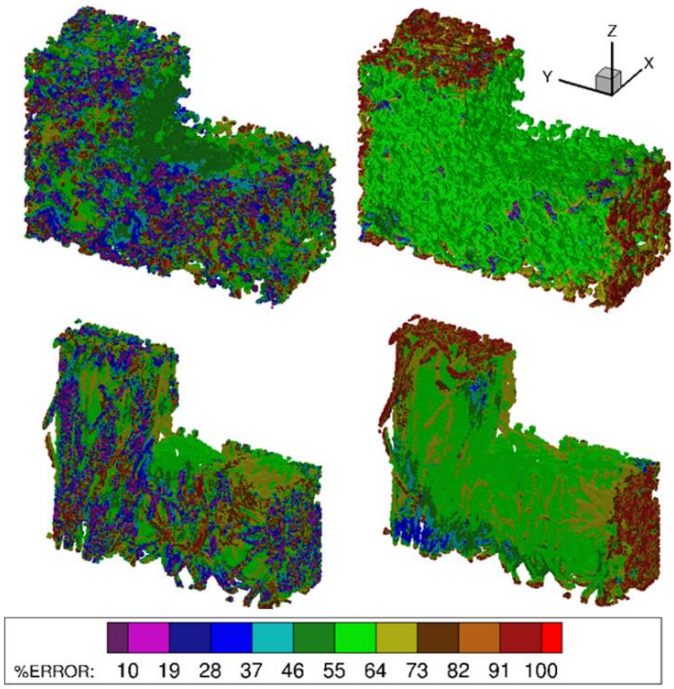

Figure 3.8 Surface *error* maps overlays for the two RVE types, relative to the whole scaffold simulation RVE equivalents. TOP ROW: Salt-leached Foam Scaffold. BOTTOM ROW: Nonwoven Fiber Mesh. LEFT COLUMN: RVE-PBC. RIGHT COLUMN: RVE-WBC. The wall is omitted from the WBC reconstructions for clarity. Top right quarter of each scaffold is removed in order to provide a view inside. Dimensions are 1.61mm x 3.91mm x 2.81mm and 1.10mm x 3.79mm x 2.99mm for salt-leached and nonwoven fiber-mesh scaffolds, respectively. *Source: [71]*

In addition to the spatial distributions of stresses, we analyzed the probability distributions of the wall shear stress magnitude. **Figure 3.9**-A & C show the histogram distributions of stresses in salt-leached foam and nonwoven fiber-mesh scaffolds respectively. Stresses are normalized using:

$(stress - mean\ stress)/(standard\ deviation\ of\ stress\ distribution)$, as is reported in our previous works.[73-75]

From the figures, it is observed that all the normalized distributions appear similar in shape but differ by frequency of occurrence of stresses. Hence, we quantified the differences, errors in probabilities for RVE-PBC and RVE-WBC are calculated as percentages of the whole scaffold simulation values using:

$$Error = |True\ Probability - Approximated\ Probability| * 100\%/(True\ Probability) \quad (3.3)$$

where *True Probability value* is probability of occurrence of each stress histogram bin in *whole* scaffold simulation histogram and *Approximated Probability value* is probability of occurrence of each stress bin in *RVE* simulation histogram. **Figure 3.9**-B & D show error histograms for salt-leached foam and nonwoven fiber-mesh scaffold. The figures show that for both scaffold architectures, the RVE-PBC produced lower errors than RVE-WBC at low stresses, while higher errors resulted at high stress values. However, since each of the histogram bins corresponds to a different probability of stress occurrence, a *weighted* average is calculated for each of the error distributions to aid better comparison between them. The *weighted* average error is calculated using:

$$W_{error} = \sum_{i=1}^{N} \left(p_i * \mathrm{err}_i \right) \quad (3.4)$$

where W_{error} is *weighted* average error, i is an index for histogram bin i, N is total number of bins in histogram, p_i is the probability of occurrence of histogram bin i and err_i is the error obtained for histogram bin i using Equation (3.3). As shown in **Figure 3.9**-B & D, the weighted average errors are lower for the RVE-PBC for both scaffold architectures; thus, confirming its superiority over the RVE-WBC.

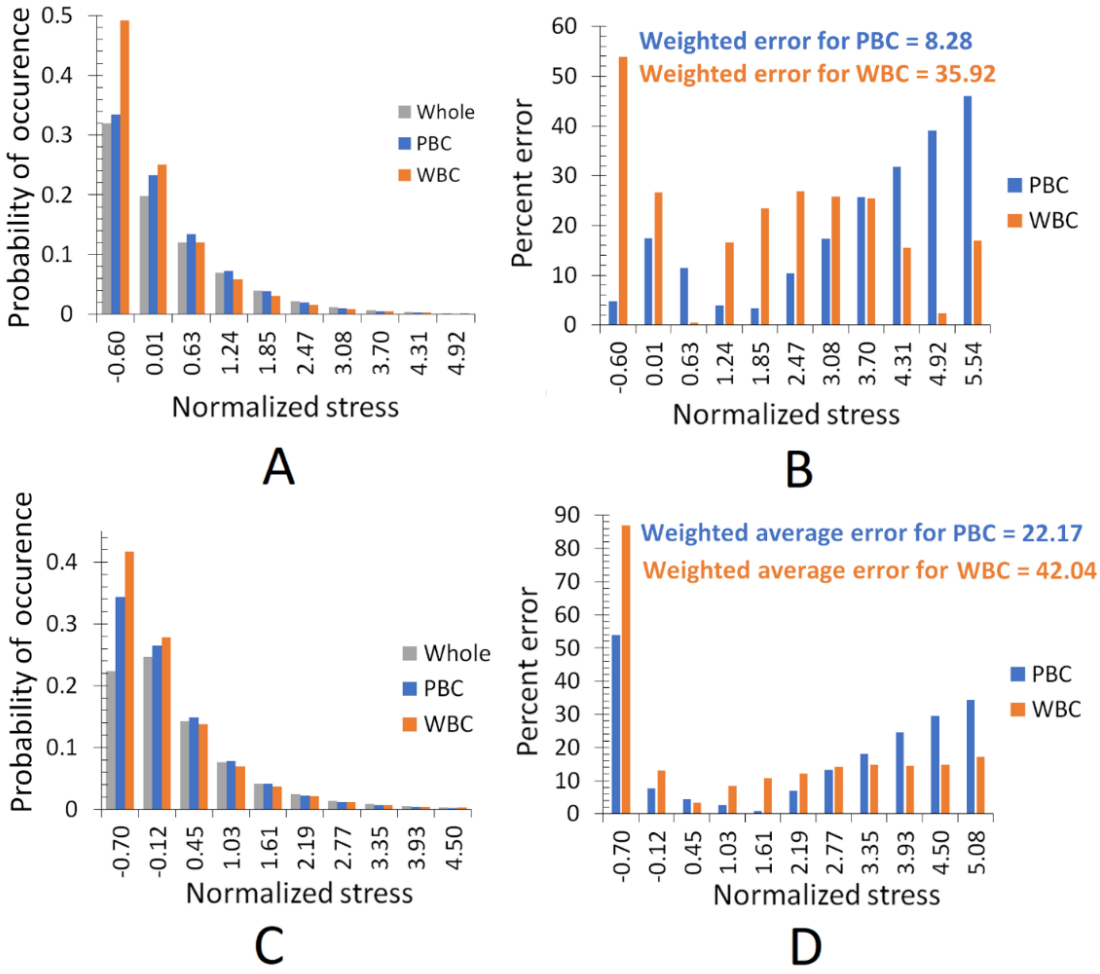

Figure 3.9 Comparison of surface stress and error histograms for Salt Leached Foam and Nonwoven Fiber Mesh scaffolds. TOP ROW: A – Histogram of normalized stresses for Salt Leached Foam Scaffold; B – Percentage error histogram for Salt Leached Foam Scaffold. BOTTOM ROW: C – Histogram of normalized stresses for Nonwoven Fiber Mesh Scaffold; D – Percentage error histogram for Nonwoven Fiber Mesh Scaffold. Grey color – Whole. Orange color – WBC. Blue Color – PBC. *Source*: [71]

Further, we wanted to check whether the type of the scaffold architecture has a significant effect on the surface stress accuracy. To that end, **Figure 3.10** plots the mean error in the RVE surface stress, relative to those from the whole scaffold simulations. We chose the abscissa to be porosity, since it also describes the scaffold morphology. From this figure, it is evident that the RVE-WBC always results in a greater error relative to that obtained from the corresponding RVE-PBC. Another observation is that the foam scaffolds always had a smaller error than the fiber scaffolds, though this is likely an effect of their lower porosity. Specifically, the error was found to increase proportionally to the latter, indicating that the porosity influences the simulation accuracy. The absolute stresses for the data in **Figure 3.10** are given in **Table 3.1**.

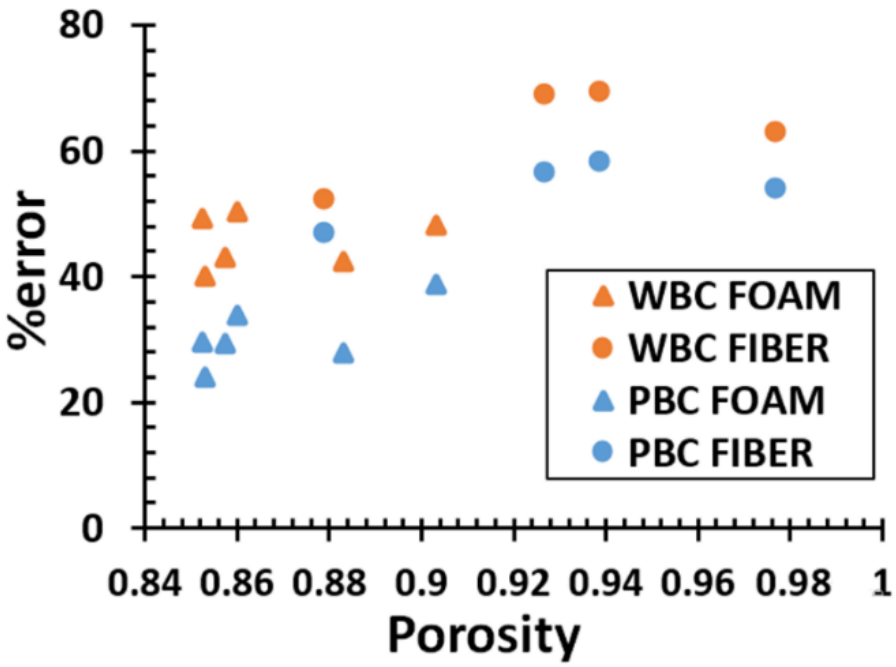

Figure 3.10 Average error in fluid-induced surface stress resulting from the RVE calculations plotted versus scaffold porosity and boundary condition type. Orange color – WBC. Blue Color – PBC. Triangles – Salt Leached Foam. Circles – Nonwoven Fiber Mesh. *Source: [71]*

Table 3.1 Summarized Stress Data and LBM Steps to Convergence for all the Scaffolds Studied

		Shear stress (dynes/cm^2)			
Scaffold type	**Porosity**	**Average**	**Maximum**	**Mean % Error**	**LBM steps**
Foam 1					
Whole scaffold	0.8830	0.078	1.695	N/A	37000
RVE-PBC		0.057	0.620	27.799	9000
RVE-WBC		0.045	0.547	42.462	12000
Foam 2					
Whole scaffold	0.9033	0.092	1.462	N/A	39000
RVE-PBC		0.056	0.608	38.860	9000
RVE-WBC		0.048	0.551	48.137	15000
Foam 3					
Whole scaffold	0.8526	0.076	2.035	N/A	38500
RVE-PBC		0.054	0.815	29.537	9000
RVE-WBC		0.038	0.649	49.389	15000
Foam 4					
Whole scaffold	0.8600	0.081	1.818	N/A	39000
RVE		0.054	0.813	33.780	9000
RVE-WBC		0.040	0.692	50.292	15000
Foam 5					
Whole scaffold	0.8573	0.074	1.958	N/A	39500
RVE		0.052	0.957	29.342	12000
RVE-WBC		0.042	0.813	43.062	15000
Foam 6					
Whole scaffold	0.853	0.068	1.263	N/A	39000
RVE		0.052	0.790	24.059	9000
RVE-WBC		0.041	0.565	40.097	15000
Fiber 1					
Whole scaffold	0.8790	0.122	3.420	N/A	36000
RVE		0.065	0.780	46.762	6000
RVE-WBC		0.058	0.920	52.340	13000
Fiber 2					
Whole scaffold	0.9268	0.134	2.318	N/A	34000
RVE		0.059	0.835	56.404	5000
RVE-WBC		0.042	0.576	68.975	10000
Fiber 3					
Whole scaffold	0.9388	0.146	3.298	N/A	36000
RVE		0.061	0.766	58.146	6000
RVE-WBC		0.045	0.641	69.195	12000
Fiber 4					
Whole scaffold	0.9770	0.127	4.345	N/A	42000
RVE-PBC		0.058	0.721	54.117	9000
RVE-WBC		0.047	0.382	62.909	14000

Lastly, the validity of LBM simulation results presented is demonstrated. We compared permeability values calculated by LBM to those obtained from the well-established Kozeny-Carman (KC) equation for porous materials (given below):

$$k = \frac{\varepsilon^3}{(1-\varepsilon)^2}\left(\frac{1}{S^2 K}\right) \tag{3.5}$$

k is the permeability of material, ε is the porosity, S is the surface area-to-volume ratio and K is the Kozeny constant. Based on experiment,[134] K is often assigned a value of 5 but recent studies have shown that its value varies with porosity.[135] The comparisons are given in **Table 3.2** and they show that permeabilities obtained by LBM are of similar order of magnitude to those from the analytical KC equation. The percentage errors between estimates obtained from the KC equation and LBM are plotted in **Figure 3.11**. It shows that values obtained by RVE-PBCs are mostly more accurate than the RVE-WBC. The discrepancy observed for scaffold with porosity of 0.977 is likely because calculations were performed using K = 5, despite its dependence on porosity.

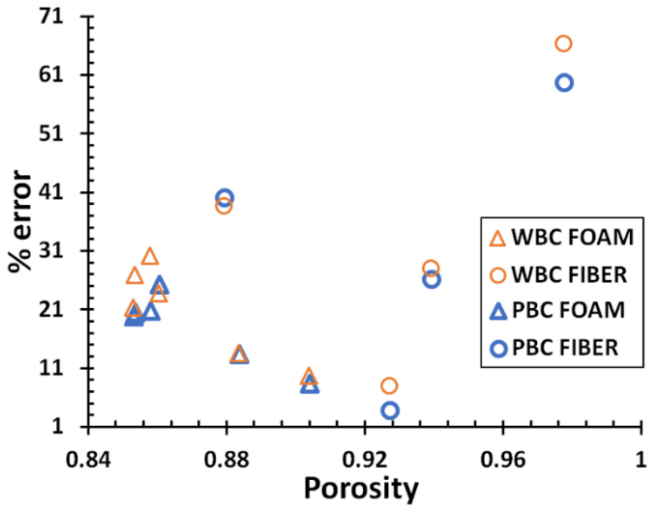

Figure 3.11 Percentage error in permeabilities calculated from LBM and analytical Kozeny-Carman equation plotted versus scaffold porosity and boundary condition type. Orange color – WBC. Blue Color – PBC. Triangles – Salt Leached Foam. Circles – Nonwoven Fiber Mesh. *Source: [71]*

Table 3.2 Permeability and Interstitial Velocity for Scaffolds

		PERMEABILITY (cm^2)	Error (%)		AVERAGE INTERSTITIAL VELOCITY (cm/s)	Error (%)
Foam 1	**KC**	1.84E-05		**Whole**	1.44E-02	
	PBC	2.10E-05	13.85	**PBC**	1.22E-02	15.30
	WBC	2.12E-05	13.85	**WBC**	1.13E-02	21.14
Foam 2	**KC**	2.50E-05		**Whole**	1.40E-02	
	PBC	2.72E-05	8.76	**PBC**	1.20E-02	14.41
	WBC	2.25E-05	10.04	**WBC**	1.11E-02	20.77
Foam 3	**KC**	1.29E-05		**Whole**	1.57E-02	
	PBC	1.55E-05	20.22	**PBC**	1.24E-02	21.39
	WBC	1.57E-05	21.56	**WBC**	9.21E-03	41.49
Foam 4	**KC**	1.43E-05		**Whole**	1.52E-02	
	PBC	1.66E-05	15.64	**PBC**	1.23E-02	19.20
	WBC	1.78E-05	24.00	**WBC**	1.03E-02	32.38
Foam 5	**KC**	1.38E-05		**Whole**	1.52E-02	
	PBC	1.67E-05	21.24	**PBC**	1.23E-02	18.87
	WBC	1.80E-05	30.43	**WBC**	1.04E-02	31.79
Foam 6	**KC**	1.40E-05		**Whole**	1.55E-02	
	PBC	1.69E-05	20.95	**PBC**	1.24E-02	20.06
	WBC	1.78E-05	27.21	**WBC**	1.03E-02	33.18
Fiber 1	**KC**	1.16E-05		**Whole**	1.48E-02	
	PBC	1.63E-05	40.39	**PBC**	9.66E-03	34.57
	WBC	1.61E-05	38.94	**WBC**	9.56E-03	35.25
Fiber 2	**KC**	1.59E-05		**Whole**	1.35E-02	
	PBC	1.66E-05	4.16	**PBC**	9.42E-03	30.17
	WBC	1.72E-05	8.20	**WBC**	9.27E-03	31.29
Fiber 3	**KC**	2.41E-05		**Whole**	1.34E-02	
	PBC	1.77E-05	26.54	**PBC**	8.95E-03	33.05
	WBC	1.73E-05	28.32	**WBC**	8.69E-03	35.06
Fiber 4	**KC**	1.11E-04		**Whole**	1.31E-02	
	PBC	4.43E-05	60.08	**PBC**	8.85E-03	32.59
	WBC	3.71E-05	66.58	**WBC**	8.79E-03	33.07

Additionally, we have validated the simulation results against a three-parameter gamma distribution, $\Gamma(\alpha,\gamma,\beta)$ which was shown to be representative of normalized wall stresses in flows through highly porous random porous media.[75]:

$$\Gamma(\alpha,\gamma,\beta)=\frac{(\tau^{*}-\gamma)^{\alpha-1}}{\beta^{\alpha}\Gamma(\alpha)}\exp\left[-(\tau^{*}-\gamma)/\beta\right] \tag{3.6}$$

where τ^{*} is the normalized stress, $\Gamma(\alpha)$ is a complete gamma function, $\alpha = 2.91$, $\beta = 0.45$ and $\gamma = -1.43$. The comparison is given in **Figure 3.12.** It is observed that RVE-PBC, RVE-WBC and whole simulation results all show good agreement with $\Gamma(\alpha,\gamma,\beta)$, however the PBC is closer to it than the WBC.

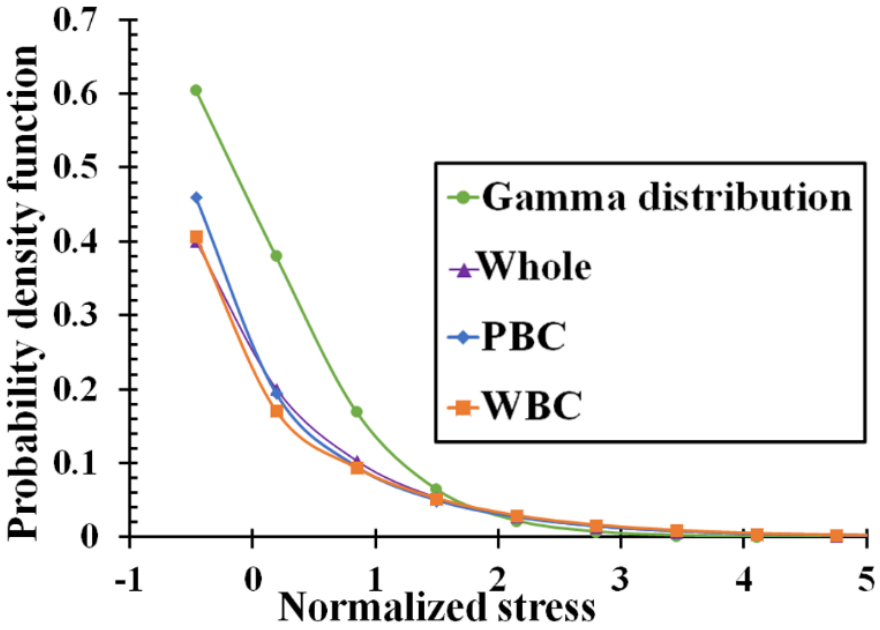

Figure 3.12 Comparison of probability density function obtained from LBM simulation results with the generalized three-parameter gamma distribution function for representative scaffold. Ordinate is probability density function and abscissa is normalized surface stress. Green color – three parameter gamma distribution. Purple color – Whole. Orange color – WBC. Blue Color – PBC. *Source: [71]*

3.5 Discussion

The ability to predict the shear stresses experienced by osteoblasts during culturing is crucial for optimizing *in vitro* bone tissue engineering experiments and scaffold designs.

For example, such models could help reveal scaffold features that are key to inducing bone forming responses: increased nitric oxide, prostaglandin and osteopontin production.[103, 136, 137] However, there is a danger that the simpleton RVE models, commonly implemented by researchers to save on computation time, could potentially yield unrealistic results. Yet, the only guideline on accuracy that currently exists in literature [119] applies to the RVE-WBC only, while the RVE-PBC remains uncharacterized. Moreover, the guideline is based on *average* stress values, which is not truly representative of what the cells experience during an actual experiment, given that they are not uniformly distributed in the scaffolds. Hence, we explored the *spatial* variations in the fluid-induced shear stresses obtained via *both* the RVE-PBC and the RVE-WBC scaffold approximations. These were compared by benchmarking against the computationally-intensive *whole* scaffold LBM simulations, which are considered to yield the *true* stress values. Moreover, we made sure that our cutout sizes were well beyond the "6 times the average pore size" guideline suggested by,[119] in order to examine the *best-case scenario* produced by the RVEs.

Consequently, the RVE simulations were found to have a significantly lower computational overhead (see **Figure 3.6**), which ultimately translates to shorter waiting times for obtaining results. Furthermore, between the two boundary condition types commonly employed in the RVE simulations, the PBC was found to converge faster than the WBC. This is largely attributed to: 1) the smaller simulation domain size of the former, since the latter models typically include an entrance length that is added in order to avoid entrance effects; and 2) the flow field being considerably simpler, since there is no wall contributing to its complexity.

Moreover, the RVE-PBC was also found to be more accurate when compared to the RVE-WBC (see **Figure 3.8** and **Figure 3.9**). Specifically, the RVE-PBC produced less error towards the cut-outs' edges, while the RVE-WBC caused more. This makes sense, given that the RVE-PBC is not affected by its boundaries due the periodicity applied, while the RVE-WBC is essentially a flow bounded by a duct. The latter is also less representative of an equivalent cut-out from the whole scaffold. Furthermore, we found that for both RVE types, the error goes up with the scaffold porosity (see **Figure 3.10**). The likely reason for this observation is that when the scaffold pores are tight, they have a dominating effect on shaping the flow field and the boundary condition effects are negligible. Conversely, when the pores become less restrictive, the effect of the boundary condition becomes more evident and contributes to the error.

However, even for the best-case scenario (i.e., when the cut-out is >> six times larger than the average pore size), the deviation from the true stress values was still between 20 and 80%, for the ten scaffolds that we tested. This is significant and can lead to misleading conclusions about the efficacy of the scaffold. Therefore, caution must be taken when using the RVE approximations. Overall, however, the fact that most of the spatial *stress* patterns were preserved, despite the use of the unrealistic boundary conditions, adds legitimacy to their use. Additionally, information about the variation of *error*, such as what is provided in this manuscript, could in theory help undo some of the inaccuracies associated with the RVEs. Until that becomes possible, however, the RVE-PBC was found to be the clear winner over the RVE-WBC, on both the accuracy and computational efficiency fronts. Therefore, it is the recommended boundary condition for large-scale

simulations, especially when the porosity of the scaffold is high (which is typical for tissue engineering).

A limitation of this study is that it was performed on *empty* scaffolds, without any cells or tissues in them. As mentioned earlier, the cells are likely to build tissues in preferred locations within the scaffolds. Therefore, the effects of the RVEs should be quantified in greater detail in the locations favored by the cells. Finally, in addition to calculating the stimulatory stresses, the flow field produced by the RVEs is often also used to model the influences of metabolite transport on the tissue growth.[75, 76] Therefore, although they are beyond the scope of this manuscript, the effects of the RVE cutouts and their boundary conditions on the mass transport within the scaffolds will be addressed in our future investigations.

Overall, the results of this study are expected to be useful to CFD applications beyond tissue engineering and LBM. For example, the RVEs are commonly used in porous media modeling,[130, 138, 139] and with non-LBM methods.[117, 118, 140] The biggest difference for the latter is that the non-LBM CFD methods may implement a non-structured mesh instead of a structured one. In the case of PBC, "pointers" are used at each boundary mesh-node in order to re-address the flow to a location appropriate for achieving periodicity.[141] Hence, the conclusions of this work apply to RVE-PBCs implemented with CFD approaches other than LBM as well.

3.6 Conclusion

In this work, we investigated the numerical differences between two types of boundary conditions, the PBC and the WBC, which are commonly employed for enabling RVE

approximations in bone tissue engineering scaffold simulations. We found that, in general, both of the RVE types followed the same *spatial* surface stress patterns as the whole scaffold simulations. However, they under-predicted the absolute stress values by a considerable amount: 20 - 80%. Moreover, it was found that the error grew with higher porosity of the scaffold but did not depend significantly on its manufacturing method. Lastly, we found that the PBC always resulted in a better prediction (i.e., lower error) than the WBC. It was also more computationally efficient, due to a smaller simulation domain size requirement. Therefore, the PBC is recommended as the boundary condition of choice for the RVE approximations. Overall, these findings fill an important knowledge gap in literature regarding the accuracy of the widely used RVE approximations. It is our expectation that they will be used to help researchers decide whether the use of the RVE approximations is justified for their application.

CHAPTER 4

APPLICATION II: TIME-DEPENDENT SHEAR STRESS DISTRIBUTIONS DURING EXTENDED FLOW PERFUSION CULTURE OF BONE TISSUE ENGINEERED CONSTRUCTS

4.1 Abstract

Flow perfusion bioreactors have been extensively investigated as a promising culture method for bone tissue engineering, due to improved nutrient delivery and shear force-mediated osteoblastic differentiation. However, a major drawback impeding the transition to clinically-relevant tissue regeneration is the inability to non-destructively monitor constructs during culture. To alleviate this shortcoming, we investigated the distribution of fluid shear forces in scaffolds cultured in flow perfusion bioreactors using computational fluid dynamic techniques, analyzed the effects of scaffold architecture on the shear forces and monitored tissue mineralization throughout the culture period using micro-computed tomography. For this study, we dynamically seeded one million adult rat mesenchymal stem cells (MSCs) on 85% porous poly (L-lactic acid) (PLLA) polymeric spunbonded scaffolds. After taking intermittent samples over 16 days, the constructs were imaged and reconstructed using microcomputed tomography. Fluid dynamic simulations were performed using a custom in-house lattice Boltzmann program. By taking samples at different time points during culture, we are able to monitor the mineralization and resulting

---

Some of the material presented in this section have been published in *Williams, C., Kadri, O.E., Voronov, R.S. and Sikavitsas, V.I. "Time-Dependent Shear Stress Distributions during Extended Flow Perfusion Culture of Bone Tissue Engineered Constructs". Fluids, 2018.* ***3****(2): p. 25.* Listed are individual author contributions: O.E.K. performed image processing, 3-D reconstruction, CFD simulation and data analysis; C.W. performed cell culture, bioreactor experiments, image analysis and data analysis.

changes in flow-induced shear distributions in the porous scaffolds as the constructs mature into bone tissue engineered constructs, which has not been investigated previously in the literature. From the work conducted in this study, we proved that the average shear stress per construct consistently increases as a function of culture time, resulting in an increase at Day 16 of 113%.

4.2 Introduction

Every year in the United States, there are more than 500,000 bone graft surgeries.[142] In most cases, bone will regenerate after fracture with minimal complications; however, when there is a critically-sized defect or fracture healing is impaired, bone grafts must be used in order to regain proper bone function. Furthermore, bone diseases such as osteoporosis, infection, skeletal defects and bone cancer may also cause a need for bone grafts. Bone tissue engineering is a possible solution to the problems plaguing the current bone graft therapies. Because tissue engineered bone would be made using the patient's own cells, immune rejection would be eliminated. For this to work, four components are needed for tissue growth: cells that can be differentiated into bone cells, osteoconductive scaffolds acting as a matrix while the tissue grows, growth factors and other chemical stimulation and mechanical stimulation to encourage osteogenic differentiation. Mechanical stimulation, in particular, is implemented through the use of bioreactors.

Previous studies have given the indication that the shear stresses bone cells experience inside the body are between 8 and 30 dynes/cm^2.[74] *In vitro* culture studies combined with computational fluid dynamics (CFD) simulation results have shown that shear stresses below 15 dynes/cm^2 are conducive to increased matrix production and

osteoblastic differentiation. However, if the shear rates are too high, detachment or cell death can occur.[143] In addition, whenever inhomogeneous cell seeding distributions occur, especially in the case of cell aggregates, even modest shear rates that are otherwise beneficial may result in cell detachment.[112, 144-146] Due to this, it is important to properly model and evaluate the flow profile inside cell-seeded scaffolds.[120, 121, 147, 148] Ideally, the localized shear rates should be anticipated in order to give proper fluid control. However, the largest barrier to this goal is the continual deposition of mineralized tissue during the culture period. After the stem cells differentiate into mature osteoblasts, both soft and hard extracellular matrices grow into the pores of the construct. This effectively alters the flow field, due to the decreasing porosity of scaffold, and renders simulations performed on empty scaffolds invalid after the start of culture.

To combat this issue, we aimed to evaluate the localized fluid shear distributions throughout the culture period, giving an indication of the effects of tissue growth on the flow-induced stress fields, which has been extensively investigated in the literature.[104, 113, 114, 149, 150] Using spunbonded poly (L-lactic acid) scaffolds and a custom flow perfusion bioreactor, rat mesenchymal stem cells were cultured for 16 days under shear-induced differentiation flow ranges. The resulting constructs were imaged utilizing microcomputed tomography (μCT), segmented and reconstructed following previously published techniques.[74, 75, 98] This allows for subsequent CFD simulations on the cultured constructs.

In this manuscript, it is hypothesized that the levels of fluid shear present at the walls of a scaffold, where the cells are located, will increase as a function of culture time. Previous studies have assumed that (1) the shear field predicted using a non-cultured

scaffold is representative of cultured constructs and (2) that the average wall shear experienced by the cells is constant throughout a culture period.[98, 151] The intention of this study is to use CFD simulations in conjunction with microcomputed tomography of mature constructs and biochemical assays to bring to light the relationship between the localized shear field and culture time, which would give researchers the ability to predict the time-dependent shear distribution in conjunction with the growing extracellular matrix within three dimensional scaffolds exposed to flow perfusion.

4.3 Materials and Methods

4.3.1 Scaffold Manufacturing

Poly (L-lactic acid) (PLLA; Grade 6251D; 1.4% D enantiomer; 108,500 MW; 1.87 PDI; NatureWorks LLC) non-woven fiber mesh scaffolds were produced via spun-bonding, as previously demonstrated.[72, 73] Scaffolds were cut from an 8 mm-thick PLLA mat, resulting in a porosity of 88% and a radius of 3.5 mm. A Nikon HFX-II microscope (Nikon Corporation, Tokyo, Japan) was used to evaluate fiber diameter, found to be 24.5 μm, and was confirmed by scanning electron microscopy, shown in **Figure 4.1**.

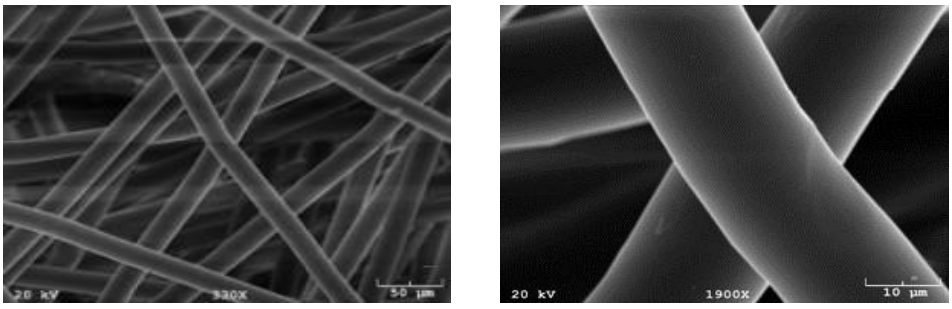

Figure 4.1 Scanning electron microscopy (SEM) images of scaffolds manufactured using spun-bounding. *Source: [72]*

4.3.2 Cell Expansion, Seeding and Culture

Adult MSCs were extracted from the tibias and femurs of male Wistar rats (Harlan Laboratories, Inc., Indianapolis, IN, USA) using protocols described in previous studies.[112, 142, 152] Cells were cultured at 37 ˚C and 5% CO_2 in standard minimum essential medium eagle alpha modification (α-MEM) (Invitrogen, Thermo Fisher Scientific corporation, Waltham, MA, USA) supplemented with 10% fetal bovine serum (Atlanta Biologicals, Flowery Branch, GA, USA) and 1% antibiotic-antimycotic (Invitrogen). Passage 2 cells were used for this study at a density of two million cells/mL for scaffold seeding. Scaffolds were prepped for cell seeding using an established pre-wetting technique.[144] Vacuum air removal of scaffolds was conducted in 75% ethanol. Pre-wet scaffolds were placed in cassettes within a flow perfusion bioreactor for one hour in α-MEM to remove any remaining ethanol.[153, 154] Following ethanol removal, two million MSCs/150 µL of osteogenic α-MEM were pipetted into each scaffold chamber. The seeding mixture was dynamically perfused at 0.15 mL/min, forwards and backwards, in five-minute intervals for two hours. Osteogenic media comprises standard α-MEM supplemented with dexamethasone, beta-glycerophosphate and ascorbic acid, which have been shown to induce osteogenic differentiation.[155] After dynamic seeding, the bioreactor was allowed to rest for two hours, without flow, to facilitate cell attachment. Finally, osteogenic α-MEM was continuously perfused at a rate of 0.5 mL/min for the remainder of the culture period. Scaffolds were collected for analysis at Days 1, 4, 8, 11 and 16.

4.3.3 Construct Cellularity

The number of cells present in each construct was evaluated using the fluorescent PicoGreen® dsDNA assay (Invitrogen). At each sacrificial time point, construct was removed from cassette and rinsed in PBS to remove any cells not adhered to the scaffold. Subsequently, the scaffolds were cut into eight pieces, placed in 1 mL of deionized (DI) H_2O and stored at -20 ˚C. Each construct underwent three freeze/thaw cycles to lyse the cells. Fluorescent analysis was conducted on a Synergy HT Multi-Mode Microplate Reader (BioTek Instruments, Inc., Winooski, VT, USA) at an excitation wavelength of 480 nm and an emission wavelength of 520 nm. All samples and standards were run in triplicate. Resulting values were then divided by the previously-determined dsDNA content per cell.

4.3.4 Construct Calcium Deposition

Calcium deposition was measured within scaffolds following the freeze/thaw cycles of the described above. The solution was measured with a calcium colorimetric assay (Sigma-Aldrich Corporation, St. Louis, MO, USA, Cat. # MAK022). Samples were read on a Synergy HT Multi-Mode Microplate Reader (Bio-Tek) at an absorbance of 575 nm. All samples and standards were run in triplicates.

4.3.5 Imaging and Reconstruction

Micro-computed tomography was used to non-destructively scan the scaffolds at a resolution of 20 μm and 45 kV energy (Quantum FX, Perkin Elmer, Waltham, MA, USA; L10101, Hamamatsu Photonics, Hamamatsu, Japan; PaxScan 1313, Varian Medical Systems, Palo Alto, CA, USA). The resulting 2D μCT image slices were filtered and

thresholded using a custom-written MATLAB code (MathWorks Inc., Natick, MA). Using a methodology described in Voronov et al.,[152] three different materials (polymer scaffold, soft tissue and mineralized tissue) were identified. This was done by using a segmentation method which allowed us to distinguish between the aforementioned materials, based on their attenuation to X-rays and structural differences. After segmentation, the images were assembled into a 3D-reconstruction. Segmentation parameters were chosen to ensure that porosity of the 3D-reconstruction matched experimentally determined values of porosity. In this study, a total of six time points were investigated (three constructs per time point).

4.3.6 CFD Simulations

Simulations were performed via the LBM implemented using a previously validated custom in-house LBM, which has been extensively utilized for computing surface shear stresses on μCT reconstructions.[74, 75, 78]

A custom-written, in-house code was developed for this work, and a detailed description may be found in previous publications.[74-76] The three-dimensional, 15 lattice (D3Q15) for LBM,[88] in conjunction with the single-relaxation time approximation of the collision term given by Bhatnagar, Gross and Krook[86], was used to perform simulations. LBM results have been validated for several flow cases for which analytical solutions are available: forced flow in a slit, flow in a pipe and flow through an infinite array of spheres.[74]

Due to the computationally-intensive nature of fluid flow simulations in scaffolds, representative portions cut from whole scaffolds are used. In this work, a single cuboid

portion was extracted from the center of the 3D scaffold reconstruction to avoid end effects in flow simulations. The resulting simulation domain size was 153 μm × 277 μm × 221 μm, with the center of the domain located at the center of the scaffold. Periodic boundary conditions were applied in all three directions, in order to approximate the whole scaffold. In addition, it was assumed that the whole extracellular matrix (ECM) was a rigid, non-permeable domain. A no-slip boundary condition was applied at wall faces using the "bounce-back" technique.[61] To take advantage of the inherent LBM parallelizability, the domain was decomposed using MPI.[94] Simulation convergence was defined as when the minimum, average and highest velocities computed for the simulation domain vary by at least 0.001% for two consecutive time steps.

In order to estimate the mechanical stimulation of the cells by the flow of the culture media, the fluid-induced shear stresses on the surface of the scaffold were calculated following a scheme suggested by Porter et al[98] given in equation (3.1). The fluid dynamic viscosity was 0.01g/cm s, which is close to that of α-MEM supplemented with 10% FBS typically used in cell culturing experiments.[133] Velocity vectors used in calculations were derived from a flow rate of 0.5 mL/min. Computed shear stress values are the largest eigenvalues of $\underline{\sigma}$. Stress maps generated using Tecplot 360 EX 2016 (Tecplot Inc., Bellevue, WA, USA) were used to visualize computed shear stresses. Additionally, we modeled the ECM as an impermeable wall without elasticity (static mesh) and did not distinguish between hard and soft ECM during the computations.

4.4 Results

4.4.1 Construct Cellularity

In order to validate the presence of cells in the constructs, a destructive dsDNA quantification assay is performed. As shown in **Figure 4.2**, there was a slight decrease in scaffold cellularity between Days 1 and 4, and a statistically steady cellularity through the end of culture. The vertical dotted line between Days 1 and 4 indicate the transition in flow rate from 0.15 mL/min–0.5 mL/min. Hence, the decrease between these two days represents a loss of cells either due to cell detachment or death.[156, 157] This loss is a common occurrence, as MSCs display weak adherence to poly (L-lactic acid) (PLLA). The horizontal dashed line represents the number of cells initially seeded on the constructs. The ratio between this line and Day 1 is known as the seeding efficiency, which in this case is 40%.

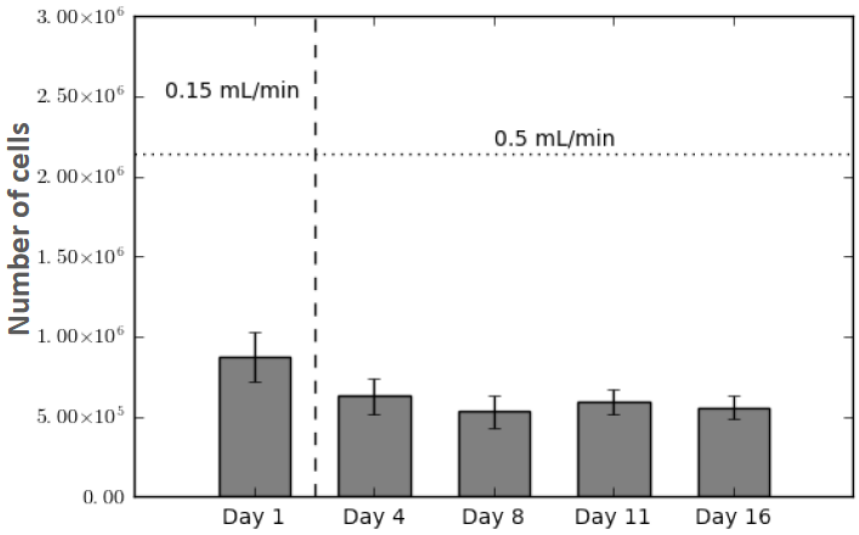

Figure 4.2 Construct cellularity for each construct over the culture period. The horizontal dashed line indicates the number of cells seeded initially; vertical dotted line indicates the switch in flow rates, from 0.15 mL/min during seeding to 0.5 mL/min for culture. Values are given as mean ± standard error of values with respect to the mean (n = 4). *Source: [72]*

4.4.2 Calcium Deposition

Calcium deposition was measured using a calcium assay at each sacrificial time point, with results shown in **Figure 4.3**. As seen in the graph, there is a sharp increase in calcium deposition around Day 8.

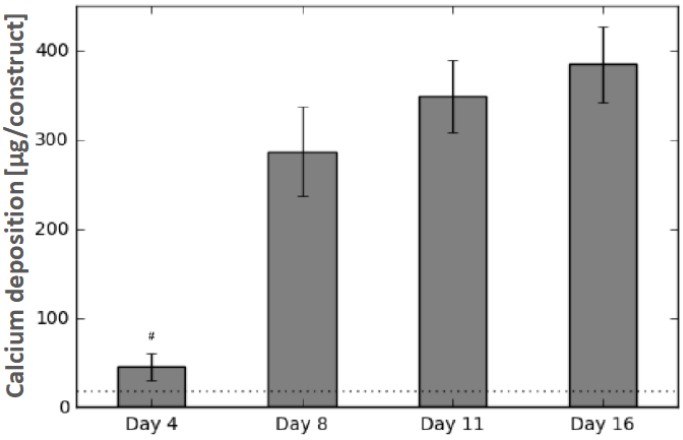

Figure 4.3 Calcium levels present within each construct over the culture period. The horizontal dotted line represents the background signal for an empty construct. Values are given as the mean ± the standard error of the mean (n = 4). The # signifies the significantly lowest value ($p < 0.01$). *Source: [72]*

In conjunction with the calcium assay, a 2D representation of the constructs is shown in (**Figures 4.4 and 4.5**). Extensive mineralized tissue can be seen in samples sacrificed after Day 8, while prior samples displayed limited amounts of mineralized tissue. It can be noted that the largest standard deviation in mineralization was observed in samples sacrificed on Day 8, a time point that matches the onset of extensive mineralization (**Figure 4.4**). A similar jump in amounts of mineralized tissue can be observed around Day 11.

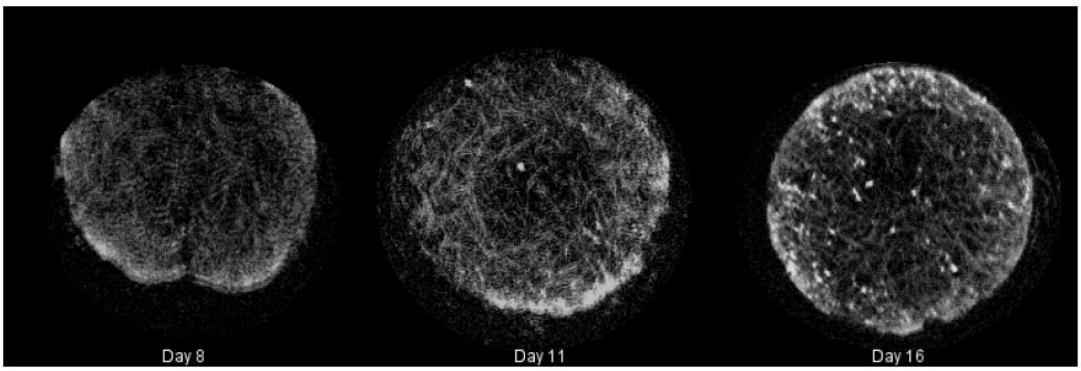

Figure 4.4 Summary of mineralized tissue (hard extracellular matrix (ECM)) deposited in cultured constructs rendered during microcomputed tomography (μCT) with Simple Viewer for samples taken on Days 8, 11 and 16, respectively. *Source: [72]*

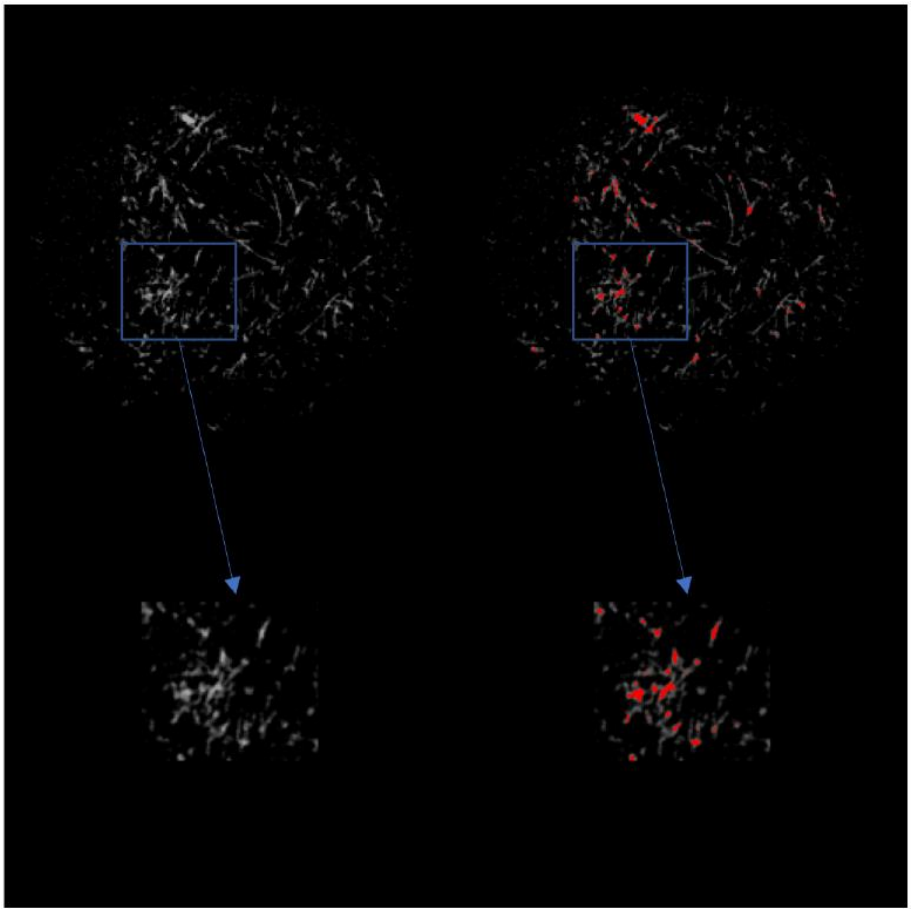

Figure 4.5 (Left) 2D grayscale view of the scaffold after μCT imaging. The top row is a view of the entire scaffold, while the bottom row is a magnified view of the indicated area of interest. (Right) 2D view of the scaffold after μCT imaging with ECM indicated in red. *Source: [72]*

4.4.3 Shear Stress Distributions over Time

The localized fluid shear stress distributions for the reconstructions at each intermittent time point are shown in **Figure 4.6**, where light blue is Day 1, green is Day 4, red is Day 8 and dark blue is Day 11. The data presented show pronounced increases in shear stress levels with increasing culture time, this is evidenced by the rightwards shift in histogram distributions shown on the graph.

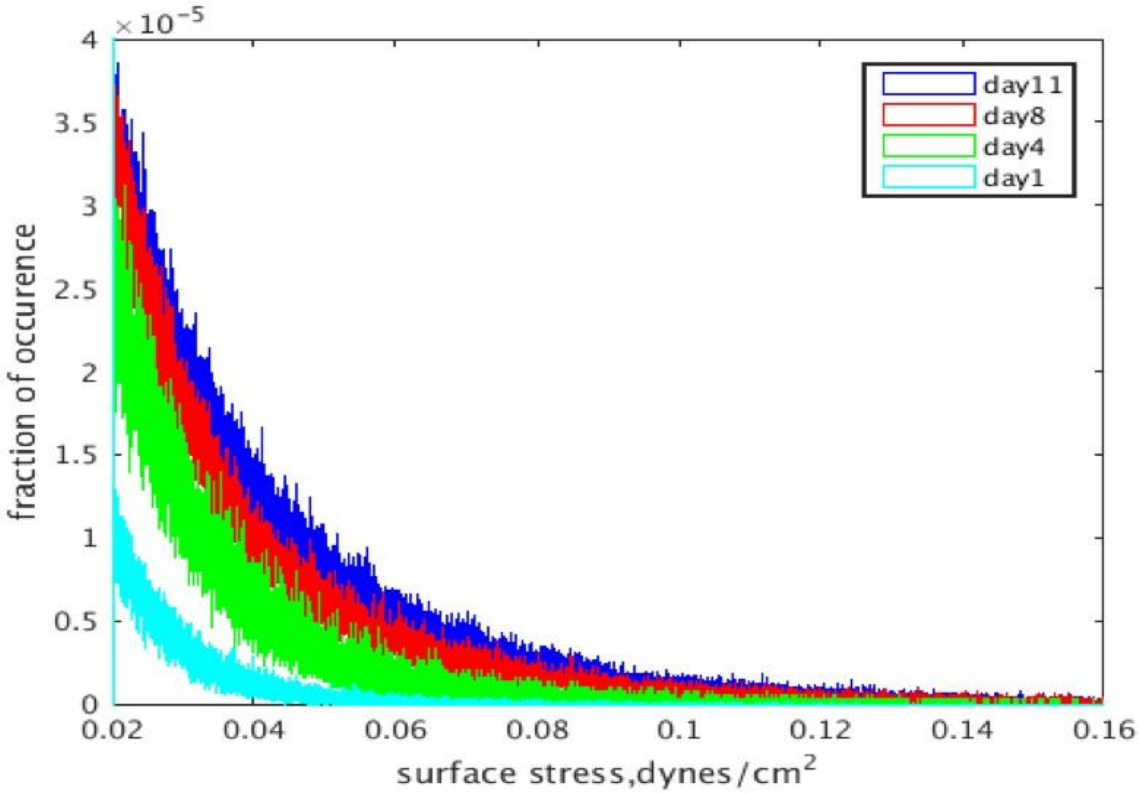

Figure 4.6 Wall shear stress histogram distributions based on the day constructs were removed from culture and imaged. *Source: [72]*

4.4.4 Effects of Calcium Deposition on Localized Shear Distributions

Figure 4.7 shows sections of reconstructed scaffold cut-outs, with wall shear stress maps overlaid on them. It is evident that there are higher shear stresses during the later time

points, which is supported by the distributions shown in **Figure 4.6**. As pore size decreases, obstructions to flow occur resulting in increased fluid velocity and, subsequently, increased shear stress (yellow and red colors in the figure). Furthermore, these increased levels of shear stress are more widely distributed as culture time increases.

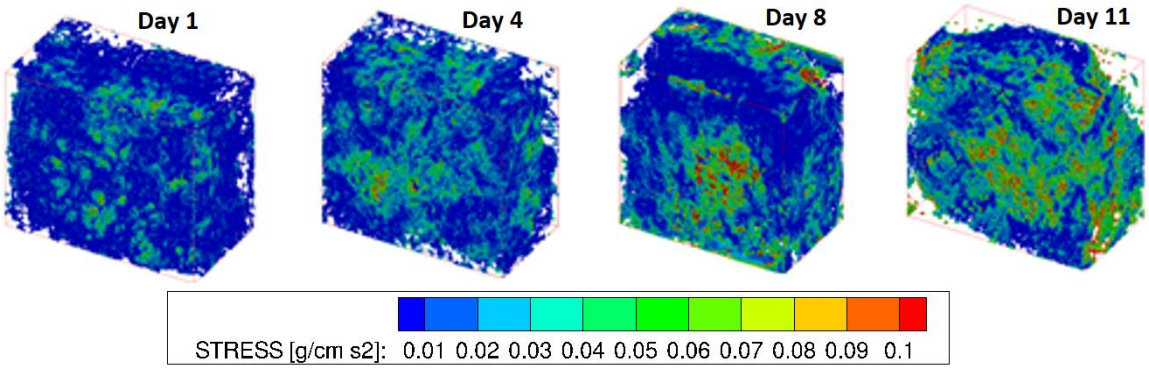

Figure 4.7 Summary of wall shear stress maps for constructs cultured under osteo-inductive conditions. Shear stress maps for Day 1 (far left) to Day 11 (far right) obtained using LBM. *Source: [72]*

4.4.5 Average Wall Shear Stress

Figure 4.8 displays the average wall shear stress calculated from LBM simulations following construct culture, resection, imaging and reconstruction. Indeed, the results reveal a continuous increase in shear as culture time increases, which is consistent with results presented in **Figures 4.6** and **4.7**. The most important revelation from this graph is the big jump in average wall shear stresses between Day 4 and Day 8. This is probably due to increased clogging of pores by matrix and is consistent with calcium deposition results given in **Figure 4.3**.

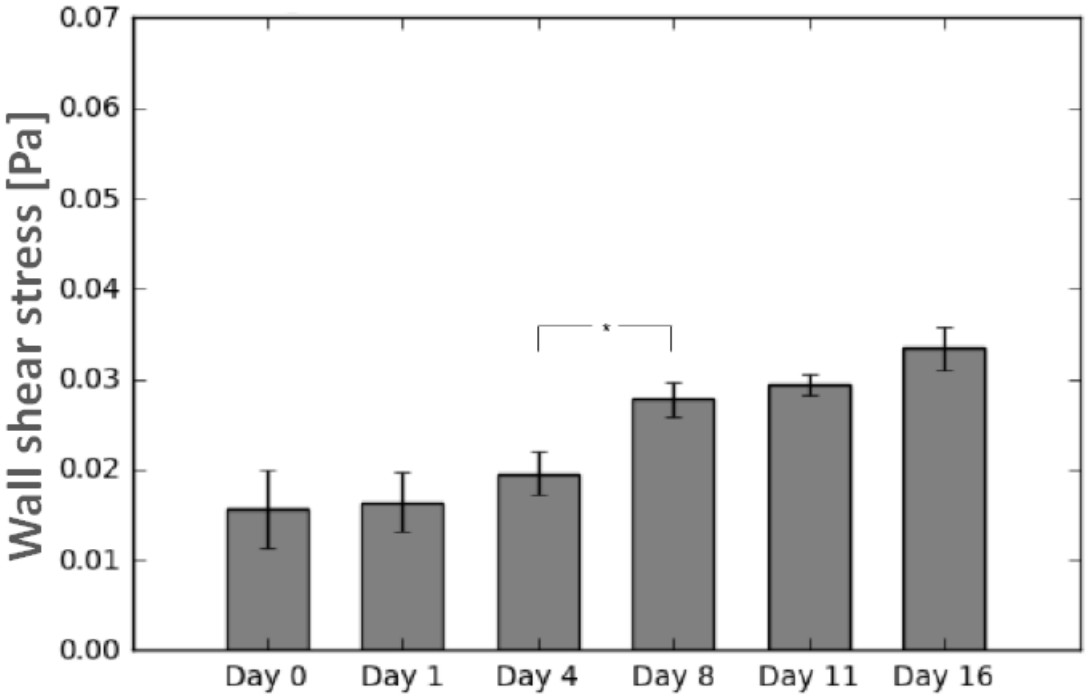

Figure 4.8 Summary of average shear stress per layer for a 0.5 mL/min flow rate. Values are given as the mean ± the standard error of the mean. *Source: [72]*

4.5 Discussion

After destructive analysis of the constructs, the average wall shear stress per construct as a function of culture time was investigated. As observed in **Figure 4.8**, the average shear stress remains statistically the same throughout the first four days of culture; however, after Day 8, there is a continuous increase in its value till the end of the culture period (113% by Day 16). This finding is consistent with other estimates of shear forces in scaffolds having similar levels of tissue formation reported in literature.[104] Furthermore, it confirms our hypothesis about bone tissue engineered cultures; that the shear stress experienced by the cells will increase significantly during culture, if the circulation fluid flow remains unchanged. This can be attributed to extracellular matrix deposition resulting in a clogging of the construct pores. By holding the circulation fluid flow constant and

simultaneously decreasing the pore sizes, fluid velocity within the construct interior is being increased and, concurrently, the wall shear stress. With respect to the influence of shear rate on osteoblastic differentiation, it is evident that a continuously increasing shear rate exposure will potentially accelerate the differentiation towards an osteoblastic lineage. Obviously, if the initial shear rates are near the range of flow-induced detachment, the observed increase could lead to undesirable detachment, necessitating the need for further investigations of the shear levels at which detachment occurs.

After evaluating the construct reconstructions, it was observed that there is a clear correlation between the amount of mineralized tissue and an overall increase in magnitude of wall shear experienced within pores of the construct. Indeed, this correlation is obvious in both **Figure 4.6**, showing the frequency distributions, and **Figure 4.7**, which shows the wall shear stress maps. Regarding the former, distributions show an increased frequency of elevated shear stress as culture time increases, supporting the aforementioned increase in average wall shear stress. This finding is consistent when evaluating the stress maps. As culture time increases, there is a higher density of elevated shear seen within the constructs. This increase is most pronounced after Days 8–11, which, according to 3D reconstructions, are when large amounts of mineralized tissue starts depositing.

Additionally, the scaffold cellularity and the levels of mineralized tissue deposited were evaluated. As seen in **Figure 4.2**, a seeding efficiency of 40% was achieved, higher than most perfusion-based seeding methods, and can be directly attributed to the oscillatory seeding protocol demonstrated in previous studies. Following complete seeding, the seeding efficiency drops further to 28% at Day 4 with the addition of a higher unidirectional fluid flow established at the end of Day 1. It is believed that the decrease in

cellularity seen between Day 1 and Day 4 is due to the change from basic maintenance flow employed immediately after seeding until Day 1 (0.15 mL/min) to culture flow beyond Day 1 (0.5 mL/min), and potentially causing a portion of cells to detach from the scaffold, especially those that form aggregates that are loosely bound to the surface. However, it must be noted that this drop could also be due to cell death or apoptosis, as observed in previous studies.[112, 144]

In **Figure 4.3**, a steep increase in calcium production is observed between Days 4 and 8. The point at which this occurs is a critical point in bone tissue engineering research and better understanding of the factors influencing it could result in more efficient scheduling of culturing bone tissue engineering constructs *in vitro*. Recent studies identifying the initiation of extensive osteoblastic differentiation using nondestructive metabolic monitoring can potentially allow future studies to better predict the exact timing of mineralization and thus allow for accurate prediction of the end of the culture period.[144]

Figures 4.4 and 4.5 demonstrate qualitatively that mineralized tissue begins developing from the outer layer of the top surface of the scaffold directly exposed to culture media flow. This result contradicts the common assumption of homogeneous cell distribution made for many tissue engineering models and cannot be justified by localized fluid shear forces produced. This observation could be an artifact that is due to the scaffold radius being slightly larger than the bioreactor cassette; thus, causing both a snug fit and decreased porosity at scaffold edges in contact with the wall. Hence, this presents an environment where cells can attach in greater numbers due to the larger surface area available for attachment. This phenomenon is not expected to occur in rigid three-

dimensional scaffolds, but will persist whenever deformable meshes are utilized, as is the case in the current study.

Finally, **Figure 4.4** shows an increase in mineralized tissue produced by visualizing μCT images between Days 8 and 11. It is believed that this lag time is due to cells starting to deposit calcium that is not dense enough to be picked up during image segmentation around Day 8. Together with this observation, **Figure 4.5** presents the 2D images obtained from μCT showing growing tissue highlighted in red. These images illustrate the state of the construct at the end of culture and provide an insight into the density of mineralization that would occur if culturing were to continue. Therefore, it is to be expected that the soft tissue visualized in the images will eventually transition into fully-mineralized tissue.

4.6 Conclusion

In the presented manuscript, it was hypothesized that the distribution of fluid shear present at the walls of a construct cultured under osteoconductive conditions will exhibit higher magnitudes as culturing time increases. In order to accomplish this, rat mesenchymal stem cells were dynamically seeded on 85% porosity spunbonded poly (L-lactic acid) scaffold and cultured with osteogenic media for up to 16 days in a flow perfusion bioreactor. Following culture, the constructs were either destructively evaluated with assays for cellularity and calcium deposition or imaged using μCT and reconstructed to allow for CFD simulations to be performed. Average shear stress values and shear stress frequency distributions obtained from simulations were compared with the assays and confirmed the initial hypothesis. In terms of the calcium quantification assay, a steep increase is observed around Day 8. This finding is supported by the reconstructions, where imaging identified

an increase in mineralized tissue between Days 8 and 11. Additionally, the stress maps revealed elevated magnitudes of shear stress during the same time period. Finally, it was shown that both the shear stress distributions and average shear stress with each construct consistently increased as a function of culture time. This is due to mineralization occurring within the pores of the scaffold, decreasing pore diameter and effectively increasing velocity within the pores. In future studies, a correlation or algorithm can be developed that will give researchers the ability to predict, for the culture period, fluid shear distributions in bone tissue engineered cultures using μCT images of empty scaffolds, CFD simulations on the 3D reconstructions and non-destructive metabolic monitoring that allows for the identification of the point of sharp increase of mineralized deposition.

CHAPTER 5

APPLICATION III: THROMBUS BIOMECHANICS

5.1 Abstract

Ischemia leading to heart attacks and strokes is the major cause of mortality and morbidity in the United States. Whether an occlusion occurs or not, depends on the ability of a growing thrombus to resist the blood flow forces exerted on its structure. This manuscript provides the first known *in-vivo* measurement of the stresses that clots can withstand before yielding to the surrounding blood flow. A hybrid semi-empirical approach was implemented to overcome the limitations of conventional techniques: namely, Lattice-Boltzmann Method fluid dynamics simulations were performed based on 3D clot geometries. The latter were estimated from intravital microscopy images of laser-induced injuries in cremaster microvasculature of live mice. In addition to reporting the blood clot yield stresses, we also show that the thrombus "core" (a region nearest the injury site, composed of highly activated platelets) does not experience significant deformation in contrast to the thrombus "shell" (an assembly of quiescent platelets covering the core). This finding indicates that the shell is the more dangerous part of the blood clot, as it is prone to embolization. Hence, drugs should be designed to target it selectively, while leaving the core intact to minimize excessive bleeding. Finally, we laid down a foundation for a nondimensionalization procedure which could ultimately lead to a unified theory of thrombo-genesis, capable of explaining all clotting events. It is expected that the findings herein will be beneficial to public health, including to the understanding and treatment of heart attacks, strokes and hemophilia.

5.2 Introduction

Achieving hemostasis following penetrating injuries is essential for the survival of organisms that possess a closed high-pressure circulatory system. However, pathological manifestation of thrombosis and embolism can potentially lead to life-threatening complications when occurring in the heart (i.e., a heart attack), brain (i.e., a stroke), or lungs (i.e., Deep Vein Thrombosis (DVT)/ Pulmonary Embolism (PE)). Among these, thrombo-embolic infarction is the leading cause of mortality and morbidity in the United States, while stroke is the 5th.[158] Conversely, deficiencies in the clotting mechanisms (hemophilia or due to drug interactions) can result in bleeding risks that confront surgeons on a regular basis. Yet, despite tremendous efforts by the medical research community (e.g., ~$3 billion of annual expenditure on heart attack and brain stroke research alone[159]), the problem that essentially amounts to a clogged "pipe" remains largely unsolved to this day. Moreover, what makes one thrombus benign, while another one dangerous, is also not well understood. Therefore, gaining insight into the thrombi's tendency to occlude blood vessels would be beneficial for public health, since it could pave the way towards a better understanding of the risk factors involved; and subsequently to better disease treatments and thromboectomy devices.[160]

Whether an occlusion occurs or not, depends on the ability of the growing thrombus to resist the blood flow forces exerted on its structure. With development of advanced intravital microscopy experiments, the thrombi structure has been shown to be heterogeneous, consisting of a densely packed "core" nearest the injury site, and a loose "shell" overlaying the core (see **Figure 5.1**).[161, 162]It is also reported that the core is composed of highly "activated" platelets (as is measured by P-selectin expression), while

the shell consists of loosely-packed P-selectin -negative cells. The biological purpose, as well as the cause of this heterogeneity, are unknown. One thing that is apparent, however, is that the core and the shell contribute differently to key parts of the thrombus formation and hemostasis: The shell is observed to shed the most mass (leading to the conclusion that embolism is mostly caused by this part of the clot); while the core can be seen to anchor the thrombus to the injury, and stop the escape of blood to the extravascular space by "sealing" the damage. This leads to an important conclusion that there are significant material and functional differences between these two regions of blood clots.

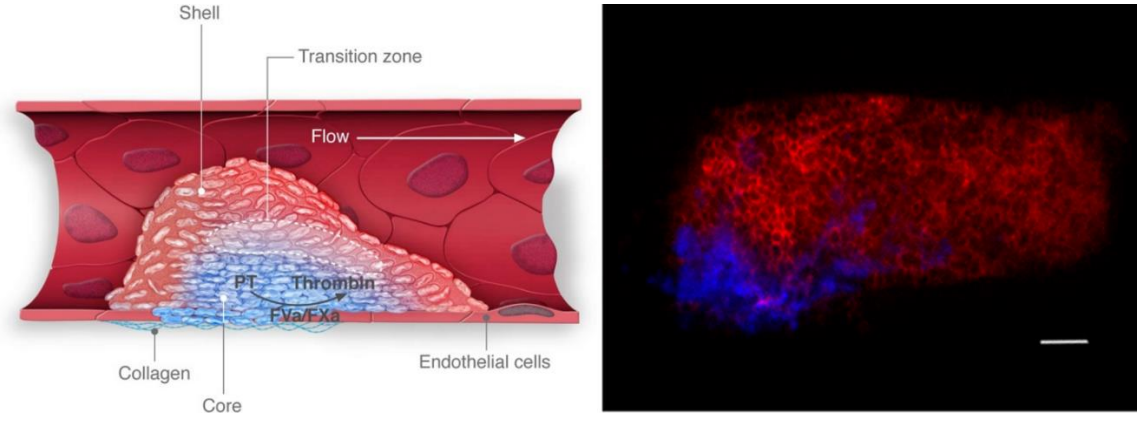

Figure 5.1 LEFT - "Core-and-Shell" model schematic showing that the clot is comprised of two regions differing in degree of platelet activation and packing density; Image reprinted with permission, from Ref. *Source: [163]* RIGHT – Confocal microscopy image of a clot (Blue = P-selectin exposure marking the activated core; Red = anti-CD41 marking the quiescent shell). Scale bar is 10µm.

At the same time, the viscoelastic behavior exhibited by the thrombi resembles that of a Bingham plastic - a material, like toothpaste, that behaves as a rigid body at low stresses, but flows as a viscous fluid when its critical yield stress σ_c is exceeded (see Equations 5.1 and 5.2). Thus, like a Bingham plastic, the clot consists of discrete particles (in this case platelets) trapped in a liquid gel. The platelets interact with each other creating a weak solid structure known as a "false body". A certain amount of stress corresponding

to σ_c is required to break this structure and allow the platelets to rearrange within the gel under viscous forces. After the stress is reduced however, the platelets associate again, solidifying the structure. **Figure 5.2** illustrates the Bingham plastic-like behavior of a blood clot as observed from intravital microscopy.

$$\dot{\gamma} = 0 \qquad \sigma < \sigma_c, \qquad \text{no flow} \qquad (5.1)$$

$$\sigma = \sigma_c + \mu\dot{\gamma}, \qquad \sigma \geq \sigma_c, \qquad \text{flow with a constant viscosity} \qquad (5.2)$$

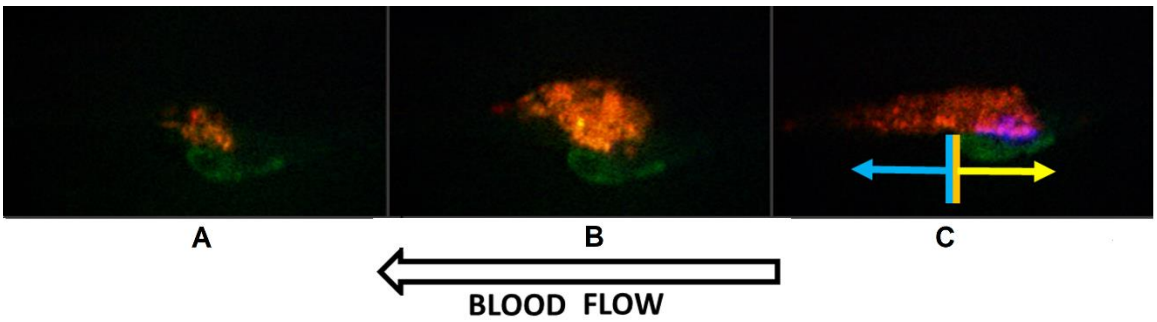

Figure 5.2 Red – Platelets (Anti-CD41 platelet marker); Blue – Core (anti-P-selectin thrombus "core" marker); Green – Injury (Uncaged Fluorescent Albumin). White Arrow – indicates the direction of flow; Yellow Arrow – Upstream portion of the clot; Cyan Arrow – Downstream portion of the clot. A – Initial attachment at injury; B – Uniform growth prior to transition; C – Final stable steady-state core-and-shell thrombus structure, after the thrombus' yielding to the blood flow.

This figure shows three major progression stages of a typical thrombus formation: 1) initial platelet attachment to the injury site (see **Figure 5.2**-A); 2) clot growth radially outward from the injury site (see **Figure 5.2**-B); and 3) steady state stability (see **Figure 5.2**-C). The transition from the second to the third stage (**Figure 5.2**, panels B→C) is the Bingham-like yielding of the thrombus. During this critical event, platelet mass from the upstream portion of the thrombus is forced to its downstream side. As a result, the thrombus changes shape from a "ball"-like structure, to the characteristic "comet-tail" shape typically seen in blood clots. This transition occurs because the obstructing thrombus

experiences stronger forces from the surrounding fluid, which is trying to squeeze through the little remaining openings left in the lumen. If there is no full occlusion of the blood vessel, the thrombus' structure eventually *yields* to the flow forces, and rearranges its shape to minimize the fluid drag imposed on its surface.

Interestingly, despite the underlying complexity of the thrombo-genesis mechanism, the discrete regimes shown in **Figure 5.2** appear to be common to all thrombi. Therefore, it is hypothesized here that the critical yield stress σ_c is a parameter that is key to understanding the extent to which the clot's structure can resist deformation and breakage. In other words, it is an important measure of stiffness that can provide information on when the thrombus is likely to become pathogenic. Yet, σ_c remains unmeasured to this day. This is because insight into thrombosis is made difficult by the fact that it is a fast, small scale process that involves a combination of coupled biochemical reaction cascades, intra- and inter- cell signaling, cell and tissue biomechanics, and non-Newtonian fluid flow.[164, 165]

Among the experimental techniques, compression testing,[166, 167] tensile testing,[168-170] shear rheometry,[171, 172] nano-indentation[173] and ultrasound elastography[174-176] are commonly used to estimate mechanical properties of the thrombi (e.g., elastic modulus, shear modulus and stiffness).[166-169, 171, 173-175] However, most of these works use *in vitro* flow loops to generate thrombi, which may not be representative of the real physiological conditions *in vivo.* For example, there are some discrepancies between the *ex vivo* and the *in vivo* measurements. One such discrepancy is the platelet attachment, which happens so fast *in vivo*, that even the high speed cameras have trouble resolving it.[6] In contrast, the time scales of platelet activation observed *ex-*

vivo are on the order of minutes, which is several orders of magnitude longer than that of *in-vivo*.[177-180]

Alternatively, a preformed thrombus could be explanted from the body for an *ex vivo* measurement. However, this type of experiment corresponds to just a single time point, and only at a late stage of the thrombus formation. Hence, it would not capture the full thrombosis dynamics; knowledge of which is necessary to measure the critical yield stress of the clot. Unfortunately, only a few studies among the above works measure thrombi biomechanical properties directly *in vivo*. A typical example is Mfoumou et al.,[176] who used shear wave ultrasound imaging to measure thrombus stiffness in rabbits' veins. However, a) the temporal resolution of the measurements in such studies is on the order of $\Delta t = 10$ mins, which is again too slow to capture thrombus growth dynamics (lasts on the order of seconds), and b) the measurement occurs through tissue, which could reduce its accuracy. Therefore, better approaches are needed to deduce the ability of blood clots to resist deformation *in vivo*.

Computational models offer an attractive alternative, because they can resolve the time scale limitation by recreating thrombosis *in silico*.[181-188] However, the clot structures generated by the simulations are not guaranteed to have realistic geometries, or to follow a realistic deformation trajectory over time. The reasons behind these limitations are the numerous unknowns in biology: for example, simulated clot structures are typically represented using either continuum models,[181, 183, 186, 188-191] discrete particle-based[182, 192, 193] or hybrid continuum/discrete particle-based[184, 185, 187, 194-196] dynamics. All these approaches rely on defining the clot biomechanics via parameters such as platelet-platelet, platelet-vessel wall/injury, platelet-proteins and fibrin-fibrin bond

strengths (typically modeled using a simple spring constant). However, since most of these parameters are obtained from in vitro experimental measurements, it is difficult to verify whether they are truly representative of the in vivo values. Moreover, some of the biological processes are simply too complex, and consequently require numerous simplifications / assumptions for achieving bottom-up modeling. For example, platelet activation – a process central to clotting, is typically modeled using top-down neural networks pre-trained on an individual's unique platelet phenotypes;[196] while bottom-up approaches to modeling the same phenomenon require unknown-parameter estimation.[197] Therefore, the purely computational methods, ultimately do not guarantee a realistic trajectory of thrombus evolution over time.

Thus, this seemingly "simple" phenomenon that is responsible for a wide range of life-threatening pathologies is not easily accessible to either experimental or computational inquiries alone. Consequently, semi-empirical approaches offer a reasonable compromise for overcoming these limitations: they bypass the need for generating the clot structure mathematically, by obtaining it from experimental imaging instead. This ensures that a realistic geometry is used for solving the physics involved in the process. For example, in refs. [180, 186, 198, 199] such models were used to calculate the time-dependent effects of surface shear stresses on thrombi developed *in vitro*. However, as mentioned previously, in vitro experiments may not depict realistic physiological conditions observed *in vivo*. Hence, in ref.[200] intravital imaging was used as the basis for calculating shear stresses in the near-thrombus region *in vivo*. Unfortunately, these simulations were 2D, which may not provide quantitatively accurate descriptions of the 3D thrombus behavior.

The reason why the latter study was done in 2D is because the thrombus structure changes faster than a 3D confocal microscopy scan can be completed.[186] Moreover, considerable fluorophore bleaching is experienced during 3D image acquisition, even if the scanned thrombus is static. To overcome this problem, here we instead estimate the 3D geometry of the clots from the high-speed imaging of their cross-sections. In this manner, our image-driven simulation approach avoids the pitfalls of using either just experiments or just computation alone. To the best of our knowledge, this combination of advanced time lapse imaging and high-fidelity computation provides the first estimate of the thrombi's yield stress *in vivo*.

5.3 Methods

The overall semi-empirical approach used in this work is summarized in **Figure 5.3**. Namely, the evolution of the clot structures over time is obtained from 2D intravital microscopy of laser-induced injuries in microvasculature of live mice. Then, the 3D shape of the thrombi is estimated by casting assumptions about the relationship between the 2D and the 3D structures (based on our previous observations).[6, 186] Finally, Lattice-Boltzmann Method (LBM) is used to calculate the fluid forces causing the thrombi to deform (i.e., the critical yield stress σ_c).

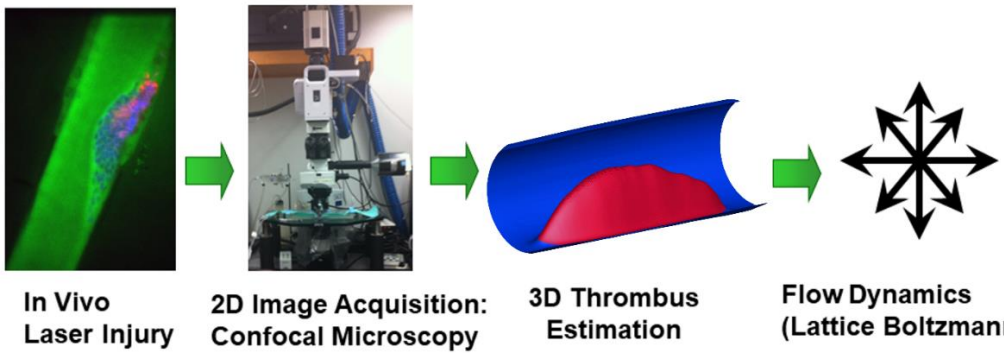

Figure 5.3 Process flow diagram for the image-based modeling methodology used in this work. Injury was first induced in the artery of mice to initiate thrombus formation (Blue color indicates activated thrombus core; red indicates thrombus shell; green represents lumen and interstitial space within the thrombus). Then high-resolution confocal microscopy was used for 2D visualization of the process. Afterwards, a reconstructed 3D thrombus geometry (red) was estimated from the 2D images (blue is pipe representing blood vessel) and imported into the LBM fluid flow solver. Finally, LBM simulation results were used to compute the shear stresses on thrombus surface.

5.3.1 *In vivo* Laser Injury and Intravital Microscopy

All of the experiments in this manuscript were performed by the Skip Brass laboratory at the University of Pennsylvania as described in refs.[6, 201] Briefly, thrombus formation was visualized in the microcirculation of live mice, following procedures previously developed in Ref.[162] In order to image the thrombus structure, intravital microscopy experiments were performed in male C57Bl/6J mice 8-12 weeks of age (Jackson Laboratories, Bar Harbor, ME). Thrombus formation in the mice was induced via laser injury of their cremaster muscle, according to procedures originally developed by Falati et al.[162] Alexa-Fluor® monoclonal antibody labeling kits from Invitrogen (Carlsbad, CA) were used to label antibodies. Anti-CD41 $F(ab)_2$ fragments (clone MWReg30, BD Biosciences, San Diego, CA) were used to visualize platelet surfaces, anti-P-selectin (clone RB40.34, BD Bioscience) was used to visualize degranulated platelets, and caged fluorescein conjugated to albumin[201] was used for lumen and laser injury site

visualization. The 2D structure of the thrombus formed due to the laser injury was imaged using confocal microscopy.

The center line maximum velocity through the mouse blood vessels was measured using optical Doppler velocimetry and divided by a factor of 1.6. The latter was done to account for a known artifact of the measuring technique: velocity profiles to appear slightly blunted and non-parabolic due to out-of-focus cells modulating the light intensity signals.[202-204] This procedure yielded an average blood vessel velocity of 4.78 mm/s. The velocimetry measurement was taken in a region away from the thrombus, to ensure that the velocity field was unaffected by the thrombi' presence. More details of the experimental procedures can be found in prior publications.[161, 201] All procedures and protocols were approved by the Institutional Animal Care and Use Committee (IACUC) of the University of Pennsylvania.

5.3.2 Image Acquisition, Post-processing and Estimation of Three-Dimensional Thrombus Shape

Since 3D imaging is too slow to capture clot shape changes, 2D images from the confocal microscope were acquired using SlideBook 5 software (Intelligent Imaging Innovations) with a time interval of 0.619 seconds and a spatial resolution of 0.22 μm/pixel. A total of 300 time images were collected for every experiment. The obtained images were deblurred using a technique reported in Ref.[6] Next, Fiji[205] plug-ins were used to compensate for vibrations due to muscle contractions in the mouse, and air currents surrounding the sample. Specifically, to achieve video stabilization, all intensity channels were superimposed together, and stabilized collectively using either StackReg[206] or Image Stabilizer ImageJ plug-ins;[207] where the choice of plug-in is based on which gave better

results for that capture. Finally, a custom Matlab code (MathWorks Inc., Natick, MA) was used to further enhance the signal-to-noise ratio of the 2D images and subsequently segment 2D thrombus shapes using standard image processing techniques.

Once the 2D images were post-processed, an in-house Matlab code (MathWorks Inc., Natick, MA) was used to generate *estimated* 3D clot geometries based on the 2D confocal images, at each time point. Specifically, the code assumed that each time-point image represented longitudinal (i.e., *parallel* to the blood flow axis) 2D cross-sections through the center of the *actual* 3D thrombi, at that same instant. This is a good assumption, since the microscope's operator particularly chose an imaging plane such that the thrombi' cross-sections were maximized. A representative grayscale thrombus cross-section from microscopy is shown in **Figure 5.4-Left.**

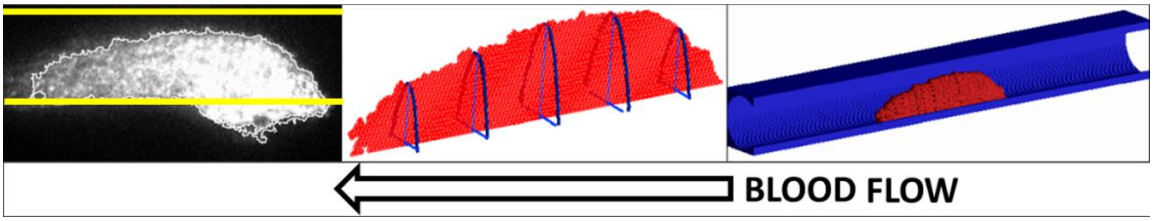

Figure 5.4 LEFT – a 2D grayscale image of a thrombus crossection obtained via confocal fluorescent microscopy (yellow line boundary outlines the segmented clot shape); MIDDLE - illustration of how parabola are fit on the edges to generate 3D geometry (red is the 2D cross-section, blue are the parabolas fitted to its "spine"); RIGHT - resulting 3D reconstruction (blue is a pipe fitted around thrombus depicting the blood vessel. Red is the actual reconstructed 3D thrombus). Pipe diameter and lengths are 0.03685mm and 0.2275mm for this experiment, respectively. White arrow indicates the direction of blood flow.

Subsequently, cross-wise (i.e., *perpendicular* to the blood flow axis) parabolic cross-sections were stacked along the "spine" of each clot artificially, to estimate the thrombus' 3D shapes (see **Figure 5.4-Middle)**. The distance between the consecutive parabolic slices corresponded to the microscopy image resolution of 0.22 μm (or one lattice

spacing in LBM units). The resulting parabolic shape, chosen to represent the outer thrombus perimeter, was selected based on experimentally-observed 3D reconstructions of a static clot.[6] Specifically, the height of each parabola was dictated by the height of thrombus' "spine" at every position along the *longitudinal* direction; while the widths of the parabolas were assumed to be in a constant 2:3 ratio with the parabola heights throughout the thrombus. This ratio was again consistent with experimental observations from static 3D *in vivo* imaging shown in Ref.[6].

Finally, the blood vessel walls were manually segmented from the 2D images to measure the lumen diameter. Subsequently, a 3D pipe of the same size was created around the estimated 3D blood clot (see **Figure 5.3-Right)**. The length of the pipe was chosen to be three times the maximum clot length, to avoid entrance effects in fluid flow simulations.

5.3.3 Fluid Flow Modeling: Lattice-Boltzmann Method

Convection within the blood vessels and around the 3D thrombi was modeled via LBM. It was chosen for this work because of the ease with which it handles complex boundary conditions, and due to its efficient parallelizability on supercomputers. A previously developed custom-written, parallelized, in-house code was used in this work.[6, 71, 74, 75, 94].

The LBM simulations were performed for a total of ten different laser-injury experiments (see **Table 5.1**). For each one, a *pseudo-steady state* approach was taken, to update the clot shape based on the successive microscopy images. Namely, flows through geometries representing each individual time step were solved *separately* from each other, as *steady state* simulations. Ultimately, the individual time step results were then

concatenated to form a continuous time-series. The pseudo-steady state approach is a good assumption, given than the fluid velocity field changes much faster than do the clot geometries.

While the viscosity of blood is known to be shear-dependent,[208, 209] here it is assumed to exhibit Newtonian behavior with a viscosity of $\mu \approx 0.03$ gr/cm-s.[210, 211] This is considered to be a good assumption due to the low hematocrit typically observed in microvasculature.[212] Given that the reality is likely to be something in-between, two different boundary conditions commonly encountered in literature were modeled: constant pressure drop[181, 199, 213] and constant flow rate.[199, 214] In both cases, the *initial* average lumen blood velocity in LBM was matched to the *in vivo* value of 4.78mm/s, obtained by optical Doppler velocimetry for a comparable diameter blood vessel (as discussed in section 5.2). The simulations were considered converged when smallest, average, and highest flow velocities in the whole simulation domain varied by less than 0.01% per LBM 1000 steps. Approximately 60,000 steps were needed for full conversion of each experimental time step. The image-based LBM simulation results were validated against an idealized homogeneous porous media model of a thrombus using a commercial CFD package COMSOL® (Discussed further in Sections 5.4 and 5.5).

5.3.4 Stress Calculations

Since the thrombi deformation was obtained from imaging, their geometry in the model was assumed to be solid. The fluid-induced shear stresses acting on thrombi surfaces were estimated following a scheme suggested by Porter et al.[98] given in Equation (2.10).

5.4 Results

The material properties of thrombi provide a measure of when the clots can potentially become pathological. The goal of this paper is to *estimate* the mechanical strength of the thrombi formed in the microcirculation of live mice. This is done by calculating the stresses induced on the clot by the surrounding blood flow, from LBM simulations based on intravital microscopy images. The hybrid semi-empirical approach helps to overcome limitations of conventional experimental and simulation tools: such as, the inability to do fast 3D fluorescent imaging in case of the former, and the uncertainty in generating the thrombi structures mathematically, in case of the latter.

5.4.1 Nondimensionalization via Data Normalization

Firstly, it was found that although each clot has unique properties (size, formation kinetics, etc.), the thrombosis dynamics look similar for different clots when compared on a non-dimensional scale. Therefore, to normalize all clots to the same scale, we nondimensionalized the experiment time by dividing it by a "characteristic" one, as shown in Equation (5.3)

$$t^* = t/t_{char} \tag{5.3}$$

where t* is the dimensionless time, 't' is the experiment time, t_{char} is some characteristic time.

To define the latter, we used the time at which the blood clot's size is maximal, because obtaining this value does not require any complicated analysis or performing simulations. The thrombus size was quantified via the *area* of the anti-CD41 platelet

marker fluorescence in the microscopy images (obtained as shown in **Figure A.1**). The ordinate values are also normalized by their respective maxima, as follows:

$$A^* = A / A_{max} \quad (5.4)$$

where, A^* is the dimensionless clot area, A is the clot area as measured from the anti-CD41 marker's fluorescence, and A_{max} is the peak value of A (obtained as shown in **Figure A.1**).

5.4.2 Distinct Regimes of Thrombogenesis

In order to identify different stages of thrombogenesis, we plotted the mean dimensionless thrombus area as a function of the normalized time (see *red* curve in **Figure 5.5**). Additionally, we plotted the mean aspect ratio (AR) for the same clots (see *blue* curve in **Figure 5.5**), in order to characterize changes in their morphology. The AR is defined as the clot height divided by the clot length and is measured based on the shape of the anti-CD41 fluorescence. However, since it is already dimensionless, the AR is plotted against the dimensionless time without normalization.

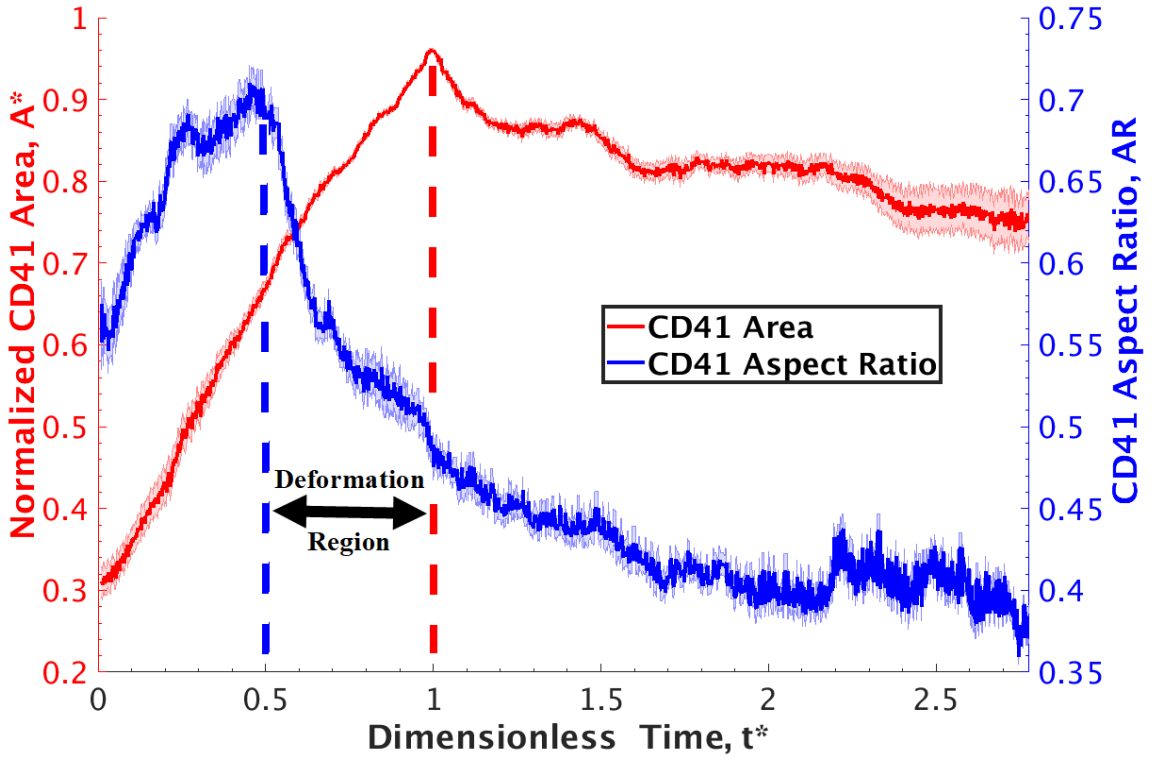

Figure 5.5 Data nondimensionalization strategy: Red graph shows the clot's cross-sectional size, quantified based on the anti-CD41 marker area in the microscopy images. Blue graph shows the clot's aspect ratio = height / length. Abscissa is the dimensionless time, whose unity corresponds to the peak CD41 area in the red curve. Both curves are moving averages with a window of 0.5, and the error bars represent the moving variance for the 10 experiments in **Table 5.1**.

Several observations regarding the mechanism of thrombogenesis can be made from **Figure 5.5**. Here, we separate them into three distinct stages, each of which describes unique characteristics of clot's evolution:

Stage I – Uniform Growth Regime: $0 < t^* <= 0.5$

During this period, both the height and the length of the clot increase simultaneously (see the *red* curve in **Figure 5.5**). However, it is evident from the upward trend in AR (see the *blue* curve in **Figure 5.5**) that the clot's growth in the vertical direction outpaces that of its horizontal elongation. The reason for the mismatch is due to differences in the mechanisms by which the clot dimensions change. Specifically, the length grows

due to the platelets attaching to the injured portion of the blood vessel wall. However, the availability of unoccupied sites in this region is limited, since the cells cannot attach to the undamaged parts of the blood vessel. This restricts the horizontal growth to the span of the injury. At the same time, the vertical growth remains unhindered, because the activated platelets can attach on top of each other as the clot builds. Consequently, platelets pile up faster vertically than they do horizontally during this stage of thrombogenesis. The described behavior continues up until approximately $t^* = 0.5$, which is considered to be the upper bound of the Stage I regime.

Stage II – Hindered Growth / Structure Yielding Regime: $0.5 < t^* <= 1$.

The boundary between this regime and the previous one is marked by the peak in the AR at $t^* = 0.5$ (see the *blue* curve in **Figure 5.5**). We define this point as the beginning of Stage II, because this is the time at which the growth in the vertical direction begins to slow down. The lag happens because the thrombus begins to occlude the lumen; and as a result, the platelets have to overcome increasingly stronger fluid flow forces in order to attach to the top portion of the clot. In contrast, the growth in the horizontal direction remains unaffected, and continues at the same rate as it did during Stage I. This happens because the platelet mass is gradually transferred from the upstream side of the clot to its downstream side, resulting in the formation of a "tail" that extends beyond the injury site. In other words, the thrombus experiences the yielding of its "false body". This is signified by a decrease in the AR – a measure of the clot's deformation. In fact, 82.65% of the AR's decrease occurs during Stage II, as is evident from the negative values of $d(AR)/dt^*$ between $t^* = 0.5$ and 1 (see **Figure A.2**). Ultimately, the end of this regime is marked by the thrombus reaching the peak size (see the *red* curve in **Figure 5.5**), which it can sustain

while opposing the blood flow forces. Consequently, the clot structure finishes the yielding, as t^* approaches the value of unity. For this reason, we choose the time $t^* = 1$ as the critical point used to mark the upper bound of Stage II.

Stage III – Structural Stabilization / Mass Shedding Regime: $t^* > 1$

The beginning of Stage III is marked by two distinct events, both of which occur for the first time since the initiation of the thrombogenesis process: 1) the clot size begins to decrease (see the decline of the *red* curve in **Figure 5.5** after $t^* = 1$); and 2) the clot length and height start to change in the opposite directions (see **Figure A.3**). Specifically, the clot height starts to decrease, while the length continues to grow. These phenomena are primarily caused by the fact that the thrombus structure has yielded and rearranged into the elongated "comet-tail" shape, which is characteristic of stable clots. Furthermore, given the streamlined shape, there is more surface area available for the drag forces to pull on and extend the clot even further. Finally, the mass shedding continues to facilitate the decrease in the clot height, as the platelet cells are removed by the blood flow from the top of the thrombus.

This interplay between the flow forces and the clot structure continues in the pseudo-equilibrium fashion, as the clot slowly thins out and stretches out. Ultimately, it retracts towards the injury site, in order to seal the damage and prevent the escape of blood into the extra-vascular. Overall, the time points $t^* = 0.5$ and $t^* = 1$ appear to be physiologically characteristic of the transitions between the distinct stages of the thrombogenesis process.

5.4.3 Clots Experience Heterogeneous Deformation During Thrombogenesis

Interestingly, the thrombus' inner region (i.e., the "core") does not show a similar trend of deformation. **Figure 5.6** shows an analysis of the cores' morphology analogous to **Figure 5.5**. Namely, this figure plots the core's P-selectin area and aspect ratio on the same dimensionless time scale, t*. The core area is also normalized according to Equation 8, where the peak value A_{max} is obtained as shown in Appendix **Figure A.4**.

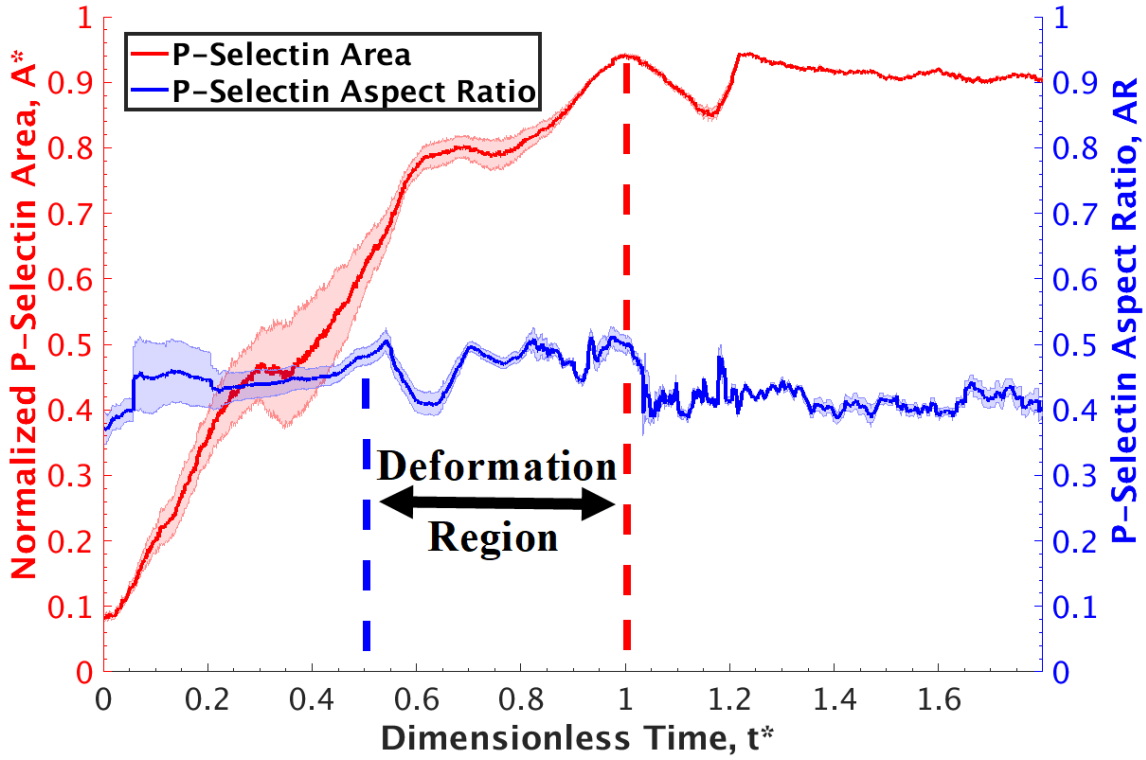

Figure 5.6 Changes in nondimensionalized thrombus' core size and morphology, plotted as function of normalized time. Red graph shows the core's cross-sectional size, quantified based on the anti-P-selectin marker area in the microscopy images. Blue graph shows the core's aspect ratio = height / length. Abscissa is the dimensionless time, whose unity corresponds to the peak CD41 area in the red curve in **Figure A.1**. Both curves are moving averages with a window of 0.5 and the error bars represent the moving variance for the 10 experiments.

Similar to the overall thrombus growth shown in **Figure 5.5**, the core increases in size up until t* = 1, after which it stays about the same size. Physiologically, the core's

growth corresponds to the activation of the platelet mass nearest the injury, similarly to what was shown in **Figure 5.2**. However, unlike the overall thrombus shape, the core's aspect ratio remains unchanged throughout the whole formation of the clot. From this, it can be concluded that for most, the clots' deformation occurs in the only thrombus' outer region (i.e., the "shell"), where loosely bound platelets are re-arranged in response to fluid flow stresses.

5.4.4 Image-based Modeling of Fluid Induced Stresses Imposed on Clots

Since the thrombus partially obstructs blood flow within the vasculature, the thrombus structure experiences forces exerted onto it by the passing fluid. These forces can drive thrombus break-up and embolism. Additionally, platelet adhesion and aggregation [215] and activation [216, 217] are influenced by local shear rate. Hence, we wanted to correlate how the fluid-induced stresses that the thrombi experience due to the flow in the blood vessels correlate to their deformation. To do this, we reconstructed the 3D thrombus shapes, estimated from the intravital microscopy images, in a virtual blood vessel (procedure in **Section 5.2)**. Once the clot geometry was obtained, an in-house LBM code was used to calculate the blood velocity field established around the thrombi versus dimensionless time (see **Figure 5.7**).

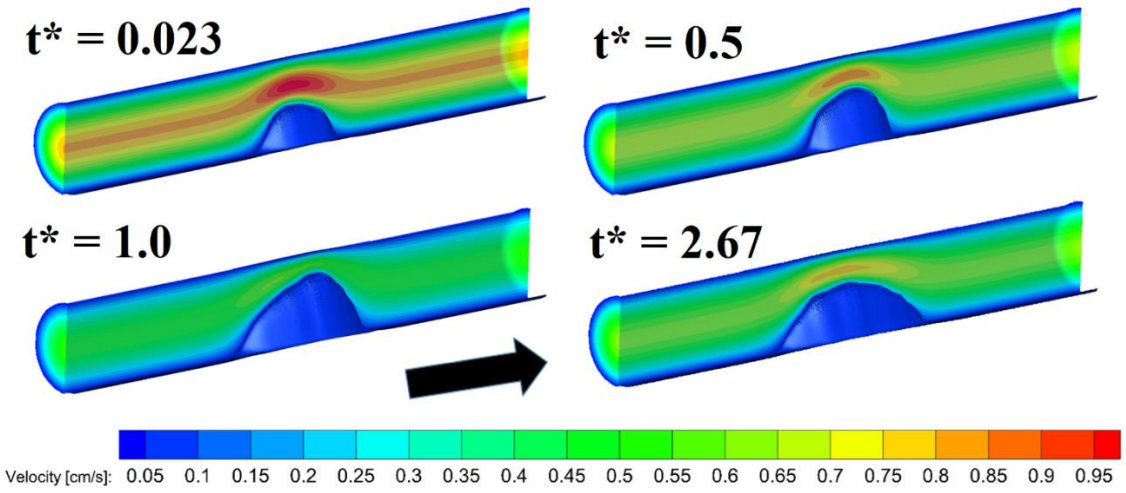

Figure 5.7 "Heatmap" of the LBM velocity field established in the lumen, calculated using the constant pressure boundary condition. The results are shown at different key time points: t* = 0.023 is an earlier time in the thrombus formation process; t* = 0.5 is the time marking the beginning of deformation/yielding; t* = 1 is the time marking the end of deformation/yielding; t* = 2.67 is a later time, after the thrombus yielding, during which it has assumed its final shape. Black arrow indicates direction of flow.

This figure shows how the velocity changes for a typical thrombus, under the *constant pressure drop* boundary conditions. In this case, the blood flow around the clot *decreases*, as the growing thrombus creates a larger and larger resistance to the flow. Conversely, in the case of the *constant flow rate* boundary condition (not shown), the velocity would *increase* to push the same amount of fluid through a narrower opening in the lumen. As discussed previously in Section 5.2.3, we performed both types of the simulations, to obtain the upper and lower bounds of the stress experienced by the thrombi. This is because the physiological reality is likely to be something in between the two boundary conditions: namely, a) an injured blood vessel tends to relax in order to avoid occlusion (similar to the *constant pressure drop* case), b) blood may get re-routed through other pathways in the vasculature (similar to the *constant pressure drop* case), and c) the heart may compensate in order to clear the obstruction by pushing the blood harder (similar to the *constant flowrate* case). Ultimately, the LBM velocity fields for both boundary

condition types were used to calculate the fluid-induced stresses experienced in the lumen, using the procedure described in Section 5.2.4.

A representative result for the *constant pressure drop* boundary condition is shown in **Figure 5.8**.

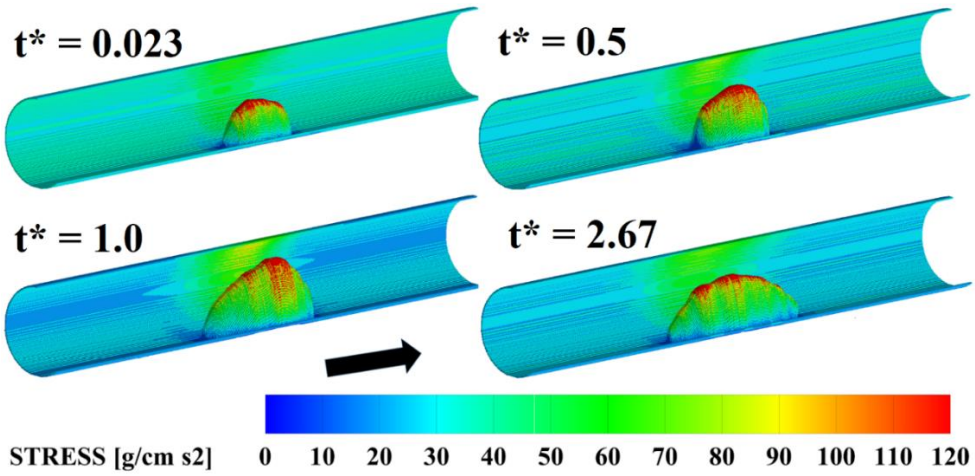

Figure 5.8 "Heatmap" of the LBM fluid-induced surface shear stress, caculated using the constant pressure drop boundary condition. The results are shown at different time points. t* = 0.023 is an earlier time in the thrombus formation process; t* = 0.5 is the time marking the beginning of deformation/yielding; t* = 1 is the time marking the end of deformation/yielding; t* = 2.67 is a later time after thrombus yielding during which thrombus has assumed its final shape. Black arrow indicates direction of flow.

Spatial surface shear stress distributions obtained from the velocity fields are shown in **Figure 5.8**. As expected, the stress distributions change with time, due to the effects that the evolving thrombus structure has on the surrounding blood flow in the lumen. As validation, the thrombus base (nearest the blood vessel wall) experienced stresses comparable to the value of ~31 dynes/cm^2 expected for an empty blood vessel of a similar diameter (calculated using Hagen–Poiseuille equation[218]). Moreover, these values are also comparable to the experimentally measured values of ~47 dynes/cm^2 for similar size arterioles of cat mesentery.[219] Finally, the top part of the thrombus protrudes into the

center of the blood vessel and experiences stresses that are several folds higher than the base. Hence, the highest flow forces are acting on the shell of the thrombus, rather than on the core. This is consistent with the shell being the part of the thrombus that experiences the most deformation.

Next, the stresses were plotted as a function of the dimensionless time t*, and normalized as follows:

$$\sigma^* = \sigma / \sigma_{max} \qquad (5.5)$$

where, σ^* is the dimensionless fluid-induced shear stress, σ is dimensional fluid-induced shear stress, and σ_{max} is the peak value of σ (obtained as shown in **Figure A.5**).

Furthermore, since the simulations are computationally expensive, only every 10^{th} time step out of the total 300 was modeled for each experiment. However, we did solve one of the experiments fully, confirm that the obtained trends would be similar. This confirmation is shown in **Figure 5.9**.

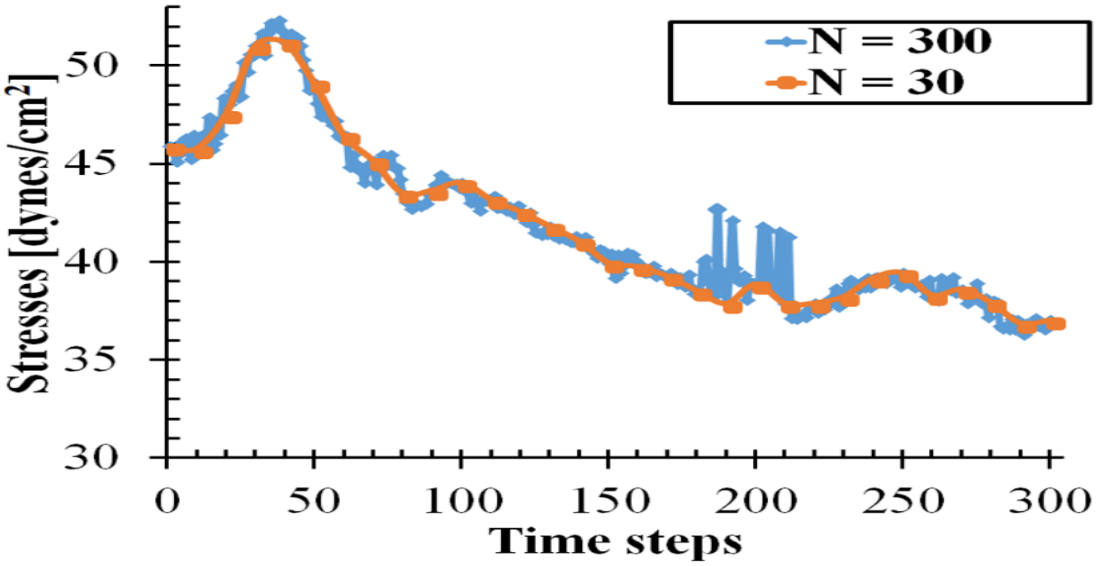

Figure 5.9 Comparison of LBM stress results for a representative laser-injury induced thrombus, solved for every time step (N=300), versus only every 10^{th} one (N = 30). The results agree with each other.

From **Figure 5.9**, it is apparent that solving every 10th time step is sufficient to capture the stress trends displayed by the thrombi. Hence, the time-coarsed stress results are shown in **Figure 5.10**.

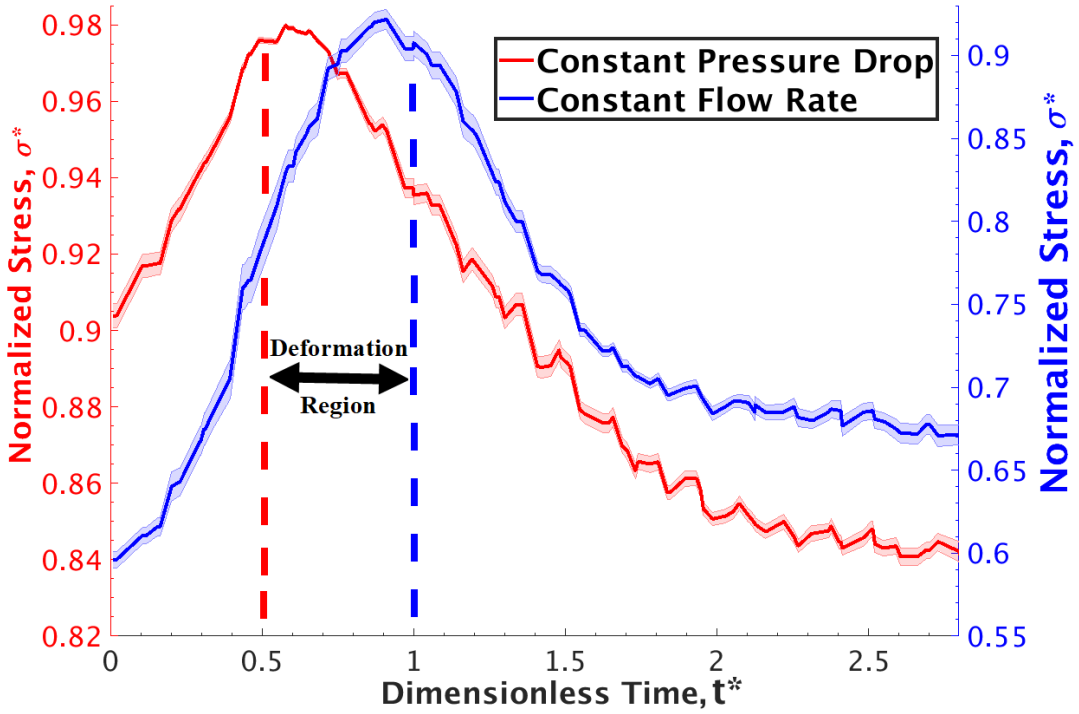

Figure 5.10 Normalized stress data plotted as a function of normalized time. Blue curve represents *constant flow rate* simulation results. Red curve represents *constant pressure drop* simulation. Abscissa is the dimensionless time; whose unity corresponds to the peak CD41 area in the red color curve in **Figure 5.5**. Both curves are moving averages with a window of 0.5 and the error bars represent the moving variance for the 10 experiments in **Table 5.1**.

In **Figure 5.10**, the normalized stresses are averaged over the thrombi surfaces, and plotted the versus normalized time, for both the *constant pressure drop* and *constant flow rate* scenarios. In both cases, as the thrombi grow in the blood vessel, the shear stresses imposed on their surfaces initially increase with time. However, the locations of the peaks do not coincide. Instead, they are located at the beginning (t* = 0.5) and the end (t* = 1) of the clot's "deformation region", for the *constant pressure drop* and *constant flow rate*

cases, respectively. This again, supports the notion that the two boundary conditions represent the extreme cases, while the reality is something in-between.

Finally, **Table 5.1** tabulates the σ_{max} values for the 10 thrombi modeled in this study, in order to enable the recovery of the actual stresses from the dimensionless curves in **Figure 5.10**. Additionally, the σ_{max} results can be extrapolated to other blood vessel sizes. For example, we have observed a strong dependence of the yield stresses on the blood vessel diameter (see **Figure 5.11)**.

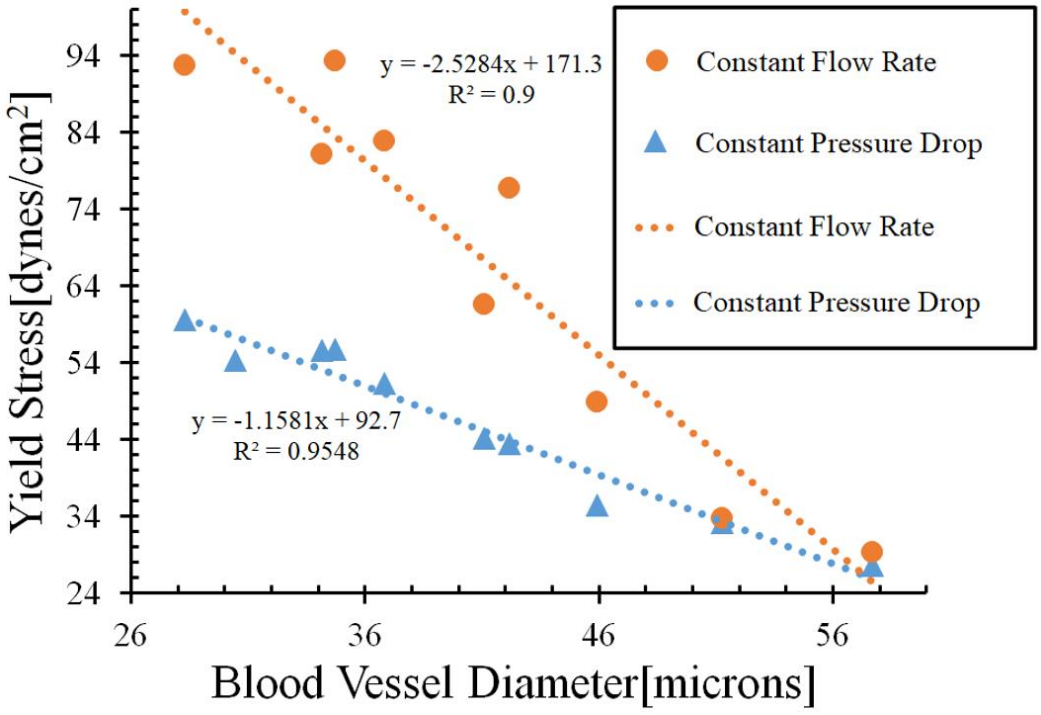

Figure 5.11 Yield Stress as a function of Blood Vessel Diameter: solid markers indicate LBM calculations, while dashed lines are linear least squares fits through the data.

Although, this may seem surprising at first, it appears that geometric attributes of the blood vessel dictate the peak size of the thrombi. Specifically, the maximum clot volume was found to vary with the blood vessel diameter and injury length (see **Figure**

5.12). Consequently, it makes sense that the clots found in different blood vessels can withstand varying amounts of stresses, depending on how big or small their structures are.

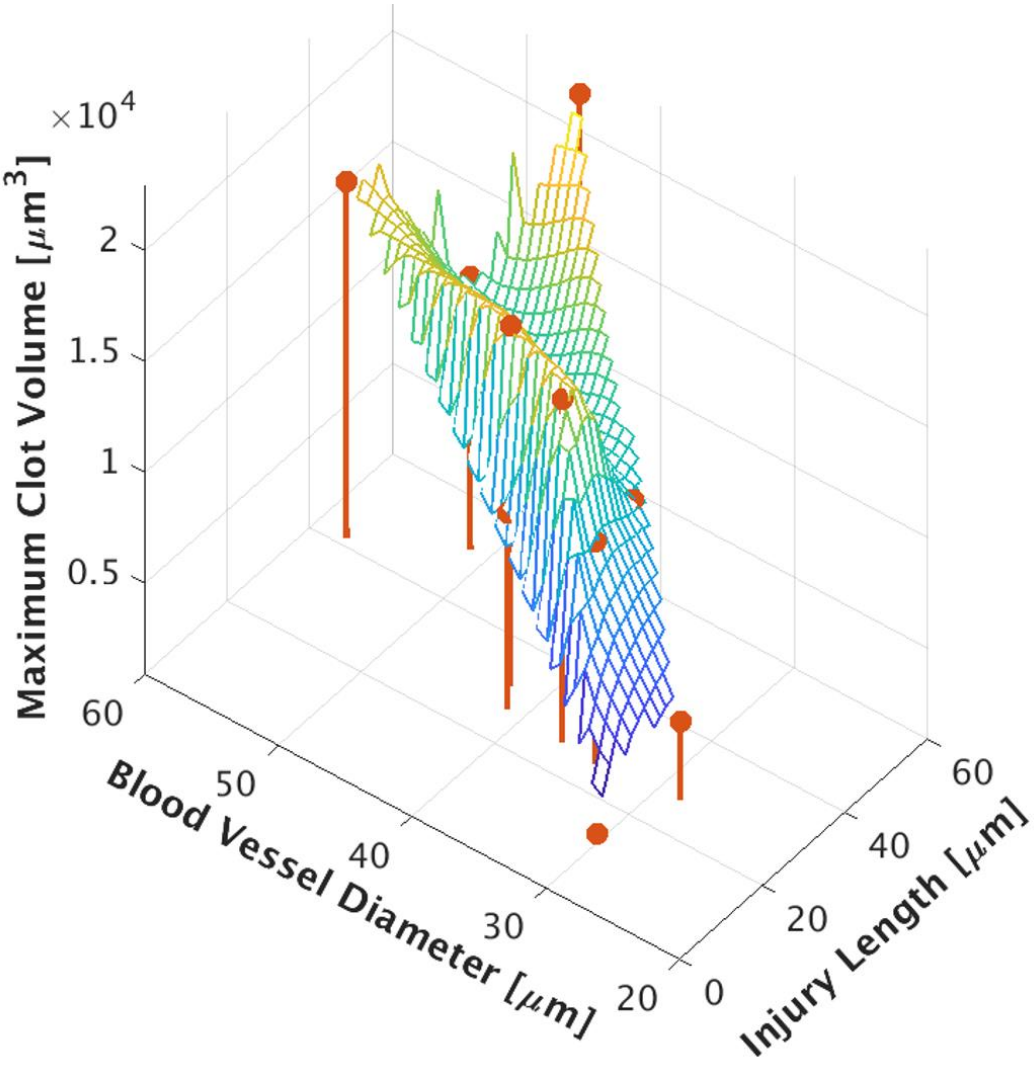

Figure 5.12 Dependence of clot size on blood vessel diameter and injury length. Red "stems" represent the 10 experimental measurements from this study, while the colored mesh is a fit through these points (meant to serve as a guide for the eye).

Table 5.1 Summary of Data for the Ten Modeled Thrombi

	Maximum stress (dynes/cm^2)		Maximum					
Blood Vessel Diameter [μm]	**Constant Pressure Drop**	**Constant Flow Rate**	**CD41 Area[μm^2]**	**P-Selectin Area[μm^2]**	**CD41 Height [μm]**	**CD41 Volume[μm^3]**	**Injury length[μm]**	**Specific Surface Area [μm^2/μm^3]**
28.30	57.12	92.68	749.89	82.98	25.90	4447.79	27.23	55838.42
34.18	55.57	81.23	1580.69	137.87	32.84	10922.70	25.63	39835.00
30.44	54.27	56.16	447.91	107.58	13.62	906.50	13.88	58685.18
34.71	55.83	93.32	1333.18	180.93	32.04	10881.41	36.31	50712.37
36.85	51.40	82.88	1759.63	170.45	36.58	16455.41	26.17	39182.72
41.12	44.23	61.67	1313.43	183.64	34.44	9818.34	26.97	53490.24
42.19	43.43	76.78	1755.28	174.02	37.91	17243.75	30.97	54409.11
51.26	33.28	33.80	2037.72	201.61	35.51	13299.55	50.46	37391.42
57.67	27.58	30.80	2297.07	173.66	36.58	17016.10	41.39	46383.00
45.92	35.43	48.89	2742.20	180.72	44.32	21660.17	59.81	43235.64

5.5 Discussion

The yield stress is a critical property representing mechanical strength of the thrombi' material; and as such, it provides a measure of when a blood clot can potentially become pathological. Therefore, quantitative characterization of this parameter is important to public health. However, it is difficult to measure τ by using either purely experimental or purely computational tools alone. Hence, we applied a semi-empirical framework that combined intravital imaging and flow dynamics simulations, to overcome the technological challenges of the conventional approaches. To the best of our knowledge, this is the first measurement of the thrombi' critical yield stress made *in vivo*.

Moreover, we have reported that the thrombo-genesis mechanism appears to consist of several discrete regimes common to all clots, despite the underlying uniqueness and complexity of their formation. Consequently, we identified the time of the clot

yielding as a characteristic nondimensionalization parameter, which can be used to collapse data from multiple injuries onto a single master curve. This consistency across the multiple blood vessel injuries gives hope that a uniform theory of thrombo-genesis can be developed, which would be able to describe all clotting events using a single analytical expression.

Finally, we showed that the thrombus core does not change shape appreciably. In contrast, the shell experiences significantly higher fluid-induced stresses, which result in its deformation. This raises the likelihood that the shell is an inherently compromised part of the clot; and that as such, it is responsible for most of the embolism. Hence, it can be concluded that the core is structurally stronger, and that it tethers the overall body of the thrombus to the injury. Consequently, the biological differences between these thrombi regions could mean that it is possible to dissolve just the dangerous part of the blood clot (i.e., the embolizing shell), while leaving the useful one (i.e., the core which seals the injury) intact. In this manner, a new generation of drugs could be developed that would selectively target just the shell; thereby avoiding the dangerous bleeding complications of the medications currently available on the market.

Although our study provides important information regarding the thrombus biomechanics, it is necessary to keep in mind that it is only an *estimate*; and that several assumptions and simplifications had to be made to obtain it. Specifically, the *limitations* of this study are as follows: 1) The clots' 3D shapes were extrapolated from their 2D longitudinal cross-sections, by assuming that thrombi crosswise profiles are parabolic in shape and have a constant width-to-height ratio (see **Figure 5.4-Middle)**. Although this was measured experimentally,[6] a late-stage *static* thrombus was used. Therefore, this

assumption may not work well for the very early stages (i.e., $t^* < 0.5$) of the thrombus formation (when the clot has a less elongated shape). However, this only concerns the 3D LBM simulations, while the 2D experimental results would not be affected; 2) The pseudo-steady state approach to the simulation necessitated the assumption that the velocity field of the blood flow establishes faster than the clots change their shape; 3) The thrombi are assumed to be impermeable to the fluid flow, since the true nature of their porous structure could not be approximated using our minimalistic approach. However, COMSOL® validations showed that making the clot permeable has a negligible effect on the stress results **(**see **Figure A.6)**; Furthermore, we confirmed that the idealized model gives stress trends similar to those obtained via image-based LBM (compare **Figure A.7** to **Figure 5.10**); 4) We did not model blood escape from the injury site, which could cause the simulated flow field to deviate from the real one; 5) The shape of the blood vessel was assumed to be a straight solid pipe, while in reality it may bend and deform, (especially near the injury site); 6) Finally, the blood was assumed to be a Newtonian fluid for simplicity. However, this is commonly done in similar thrombo-genesis modeling studies.[6, 180, 198, 220]

The future directions for this work include performing similar measurements of the blood flow forces experienced by occlusive and embolizing thrombi (both of which are harder to induce and capture experimentally). Furthermore, we plan to continue working towards developing a universal model of the thrombo-genesis. This will be done by correlating other physiological phenomena, such as the dynamics of the blood's escape to the extravascular space, to the dimensionless time scale, t^*. Finally, superior imaging

methods will be used to capture the real-time 3D thrombi shape changes, instead of relying on extrapolations based on the 2D cross-sections from conventional confocal microscopy.

5.6 Conclusions

In this study, we have performed an in-depth analysis of intravital microscopy images, showing thrombi development in response to laser-induced injuries in live mouse microvasculature. Based on these results, we were able to conclude that the thrombus core does not change shape appreciably during thrombo-genesis, but its shell does. This implies that there are inherent differences in the material properties of these two regions of the clots. Furthermore, we performed image-based LBM modeling, which allowed us to calculate the fluid-induced shear stresses imposed on the thrombi's surfaces by the blood flow. From these results, we observed that it is the thrombus shell that experiences the highest fluid-induced shear stresses on its surface. A combination of the two results, namely that the shell is both weaker and experiences more deformation, leads to the conclusion that it is the most prone to embolism. The implications of this finding are that a new class of anti-embolic drugs could be developed, which would target the dissolution of the shell selectively, while preventing the risk of severe bleeding (typically associated with the existing antithrombotic medications) by leaving the core of the clots intact. Finally, we have laid down a foundation for a nondimensionalization approach to interpreting thrombo-genesis data, with the hopes that a uniform theory could be developed through an extension of this procedure. Overall, the findings herein are expected to be beneficial to understanding the process of thrombo-genesis, which is central to heart attacks and strokes that are plaguing the public health today.

CHAPTER 6

ENDOTHELIAL CELLS COULD BE RESPONSIBLE FOR THE OBSERVED CORE-AND-SHELL THROMBUS ARCHITECTURE

6.1 Abstract

Ischemia leading to heart attacks and strokes is a major cause of deaths in the world. This study explores the possibility that intracellular material from ruptured endothelial cells is partially responsible for the heterogeneous core-and-shell blood clot architecture, typically observed using intravital microscopy. As evidence, we present a fluid dynamic argument that platelet agonists emanating from the injury cannot activate platelets in the thrombus core, given that they would have to travel *against* flow of blood escaping into the extravascular. Furthermore, we demonstrate visual evidence that the core material appears to be continuous and originates from the damaged endothelium. Finally, we present a mechanism, illustrating the steps of platelet recruitment into the thrombus and sealing of the injury. If correct, the model presented herein will be beneficial to the understanding and treating of heart attacks, strokes and hemophilia.

6.2 Introduction

Thrombo-embolic infarction is the leading cause of mortality and morbidity in the United States, while stroke is the 5th.[158] Yet, despite tremendous efforts by the medical research community,[159] the problem remains largely unsolved to this day. Recent developments[162, 221] in intravital microscopy have shown[161] that the clots consist of: 1) a densely packed "core" that is responsible for the cessation of blood loss; and 2) a loosely-packed "shell" whose embolism is potentially life-threatening. Hence, these differences could be utilized for circumventing excessive bleeding that is associated with the existing antithrombotic treatments. Also, insight into the thrombogenesis mechanism would be beneficial for public health.

Currently it is thought that the core is composed of highly "activated" platelets, while the shell consists of less activated ones. Explanations have been put forward that primary platelet agonists (e.g., thrombin) from the injury do not reach the shell,[6, 222, 223] resulting in a degree of secondary platelet activation that is insufficient to elicit granule release in that region (see Fig.7 in Ref [161]) .

Additionally, it has been shown that in Sema4D$^{-/-}$ mice[224] the dense packing of the core region not only precedes *full* platelet activation, but is at least partially independent of it.[201] This could be indicative of presence of a non-platelet material in the thrombus core. In fact, the validity of the core-and-shell model rests upon the *interpretation* that the P-selectin expression is a signature of platelet activation only.[161, 225-227]

However, endothelial cells (ECs) also contain P-selectin in their Weibel-Palade bodies.[228-230] So, it is possible that the early P-selectin signal originates from the "guts" of the damaged ECs, leaving room for an alternative mechanism of the core-and-shell

formation. This study explores the fidelity of this alternative mechanism. To achieve this, we analyze the same time lapse intravital microscopy images used for the image-based modeling work performed in chapter 5.

6.3 Methods and Materials

All experiments were performed by the Skip Brass laboratory at the University of Pennsylvania. Briefly, in order to image the thrombus structure, intravital microscopy experiments were performed in male C57Bl/6J mice 8-12 weeks of age (Jackson Laboratories, Bar Harbor, ME). Thrombus formation was induced via laser injury of their cremaster muscles.[162] Alexa-Fluor® monoclonal antibody labeling kits from Invitrogen (Carlsbad, CA) were used to label antibodies: Anti-CD41 $F(ab)_2$ fragments (clone MWReg30, BD Biosciences, San Diego, CA) were used to visualize platelet surfaces, anti-P-selectin (clone RB40.34, BD Bioscience) was used to visualize degranulated platelets, and caged fluorescein conjugated to albumin (cAlb) was used to measure clot porosity and visualize blood escape into the extra vascular.[201] Additional details on the methods can be found in [161, 201]. All procedures and protocols were approved by the Institutional Animal Care and Use Committee (IACUC) of the University of Pennsylvania.

6.4 Results and Discussion

6.4.1 Different Blood Flow Patterns Do Not Affect the Core-and-Shell Formation

There are typically two extremes of the laser injury types commonly achieved under *in vivo* conditions: **Figure 6.1-A** shows an injury that is *non-penetrating* (i.e., no blood escapes to

the extravascular) while **Figure 6.1-B** shows a *fully penetrating* injury (i.e., blood does escape to the extravascular).

Also, videos (https://vimeo.com/user92157740/review/302888553/b6ad320fa9) and (https://vimeo.com/user92157740/review/302888560/d2834a5c98) show movies for non-penetrating and penetrating injuries respectively.

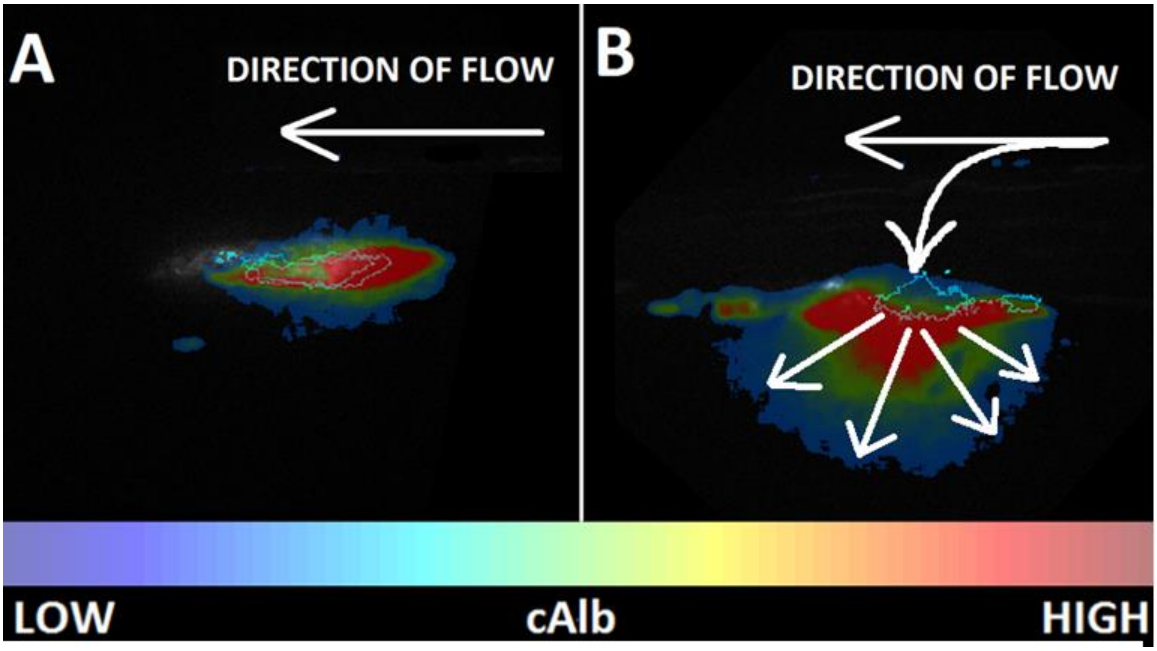

Figure 6.1 Injury types visualized via fluorescently labeled cAlb: (A) Non-penetrating – cAlb is trapped in a punctured muscle cell, encircling the blood vessel; and (B) Fully Penetrating – cAlb escapes into extravascular. The images correspond to the initial time of the injury, before the thrombus has formed. The cyan outline shows the steady state outline of the thrombi's cores.

Despite the drastic differences between both injury types, no differences in either timing or spatial patterns of the core's activation are observed between the two blood flow regimes. This is in contradiction to the conventional model of the core-and-shell formation, which depends on the platelet agonists fluxing from the injury *upward*.

In fact, **Figure 6.2** shows that the P-selectin expression increases steadily throughout the time course of thrombus growth (which takes place between $t^* = 0$ to 1, where a value of unity represents peak clot size). Yet, the decrease in the blood's escape due to sealing of the injury does not appear to affect the expression of the P-selectin in the core. Hence, it is unlikely that primary platelet agonists would be able to emanate from the injury and diffuse *against* the convective flows of blood (especially considering that they are large molecules, with small diffusivities).

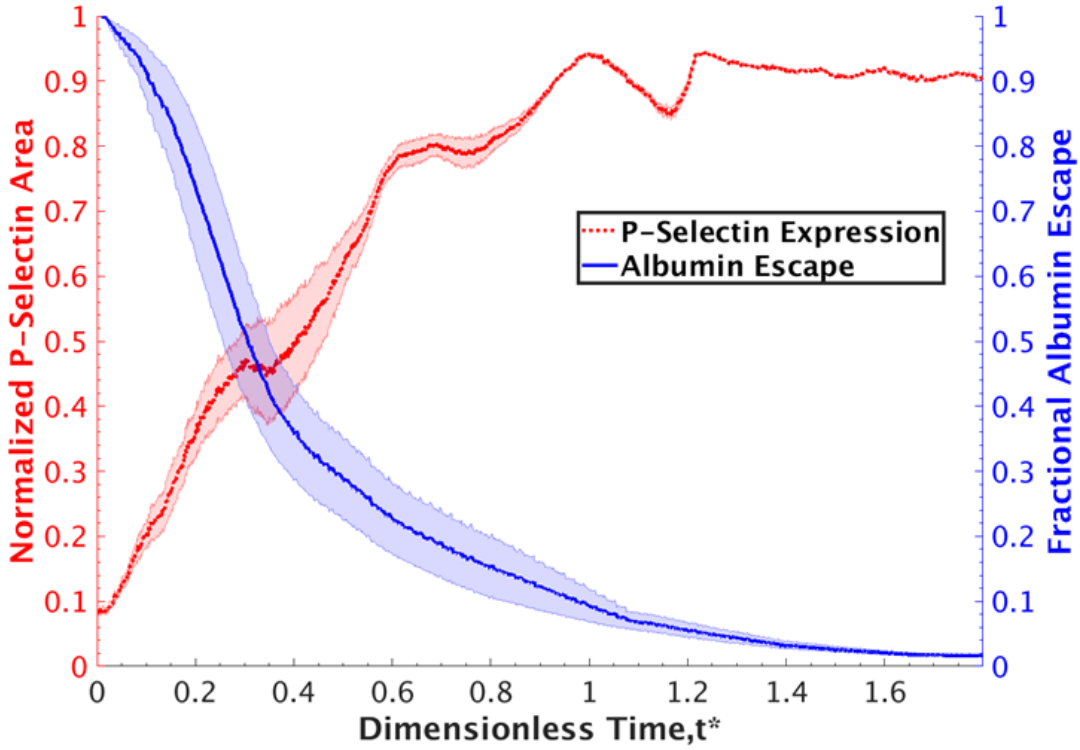

Figure 6.2 Time course of blood escape to the extravascular space (blue) versus P-selectin expression in the core (red). The former is based on the area of the fluorescently labeled cAlb in the extravascular space while the latter is quantified by measuring the area of CD62P in the intravital microscopy videos. Dimensionless time scale is achieved via normalization by the characteristic time at which the clot size is maximum. Both curves are moving averages with a window of 0.5; and the error bars represent the moving variance for 10 different laser injury experiments on wild type mice.

6.4.2 The Role of Hypothesized Endothelium Participation in Thrombogenesis

Figure 6.3 illustrates the hypothesized mechanism of thrombogenesis. As with conventional models, the injury is initiated at $t^* = 0$ by rupturing an EC. However, in our model the EC's interior is immediately exposed to the blood flow contents in the lumen (see **Figure 6.3-Left**). Next, a gelatinous substance emanating from the damaged EC captures the platelets from the blood flow and recruits them into the thrombus. It is this substance that displays the majority of the early P-selectin signal and is perceived as the thrombus' core in the intravital microscopy videos.

As the thrombus grows further, it begins to occlude the passage of other blood contents. Ultimately, at some critical stage, the thrombus achieves its peak size (see **Figure 6.3-Center**) and is consequently deformed by the fluid shear. At this point, the platelets from its front are transferred to the downstream side. When this happens, the upstream portion of the thrombus wraps around, creating the classical "comet" tail pattern (see **Figure 6.3-Right**). Finally, the gel retracts back into the damaged vessel wall, ultimately resulting in consolidation of the platelets at the site of the injury (see Fig. 6.1-A & B and supplemental Vid. 1 in Ref. [231]) and sealing the wound.

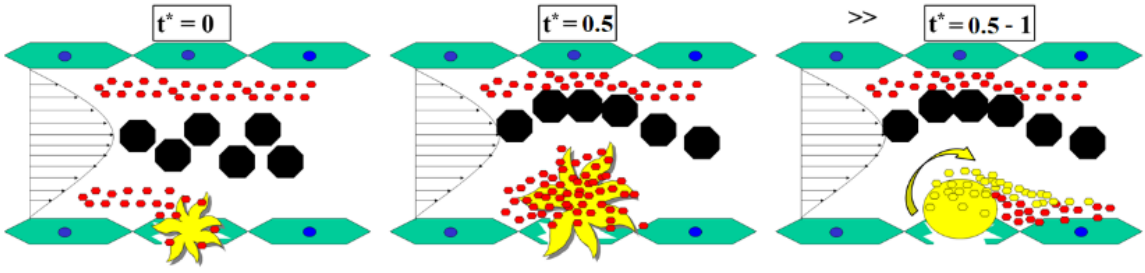

Figure 6.3 Hypothesized thrombogenesis mechanism, as a function of dimensionless time, t^*. Green = intact ECs; Red = Platelets; Black = Red & White Blood Cells; Yellow = damaged EC's "guts". LEFT – EC guts are exposed to the blood contents as a result of thrombogenesis initialization via injury. CENTER – platelets are captured by the exposed

EC guts in the lumen. RIGHT – transfer of upstream mass to the downstream side, resulting in thrombus' comet shape.

Furthermore, individual platelet tracking results (see **Figure 6.4**) indicate that the thrombus cells are being drawn inward towards the injury (often against the direction of blood flow). Hence, the process is likely driven by the aforementioned gel retracting back into the damaged EC.

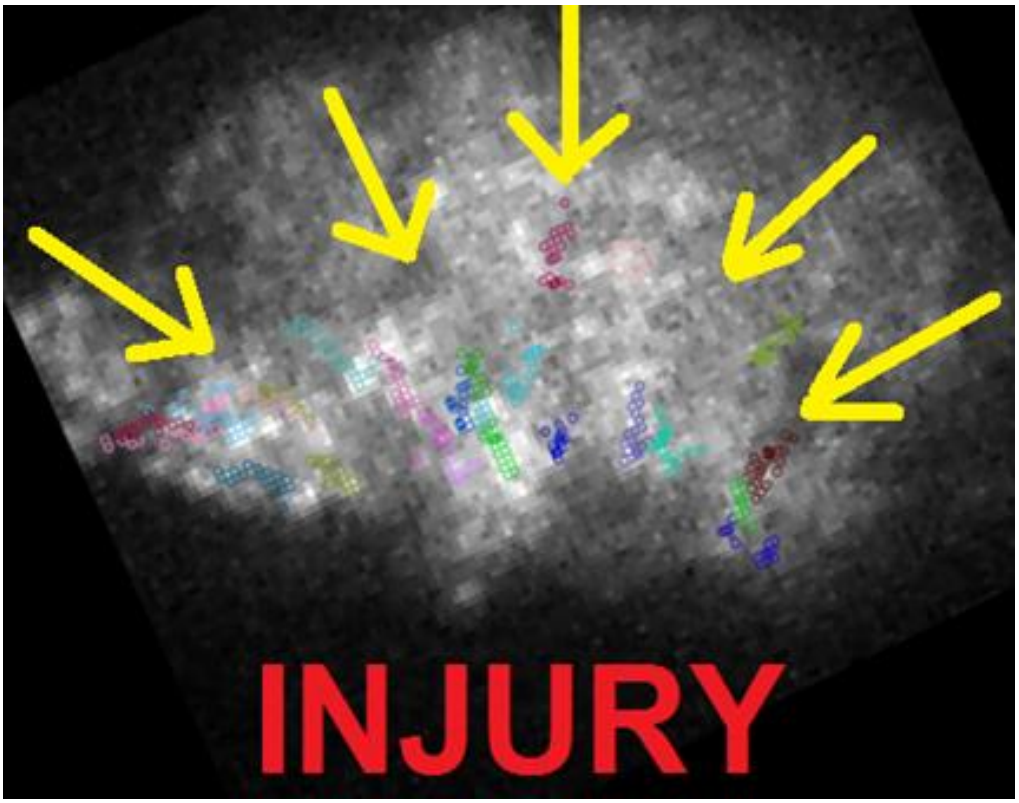

Figure 6.4 Single platelet tracking within the thrombus. Gray = platelets imaged via anti-CD41 fluorescence; Color = platelet tracks; Yellow arrows highlight the direction of the platelet tracks.

In addition, **Figure 6.5** show that the P-selectin core (green) stretches out from the injury like protrusions (outlined in yellow), and strongly resembles a continuous substance, rather than discrete platelets visible in the shell.

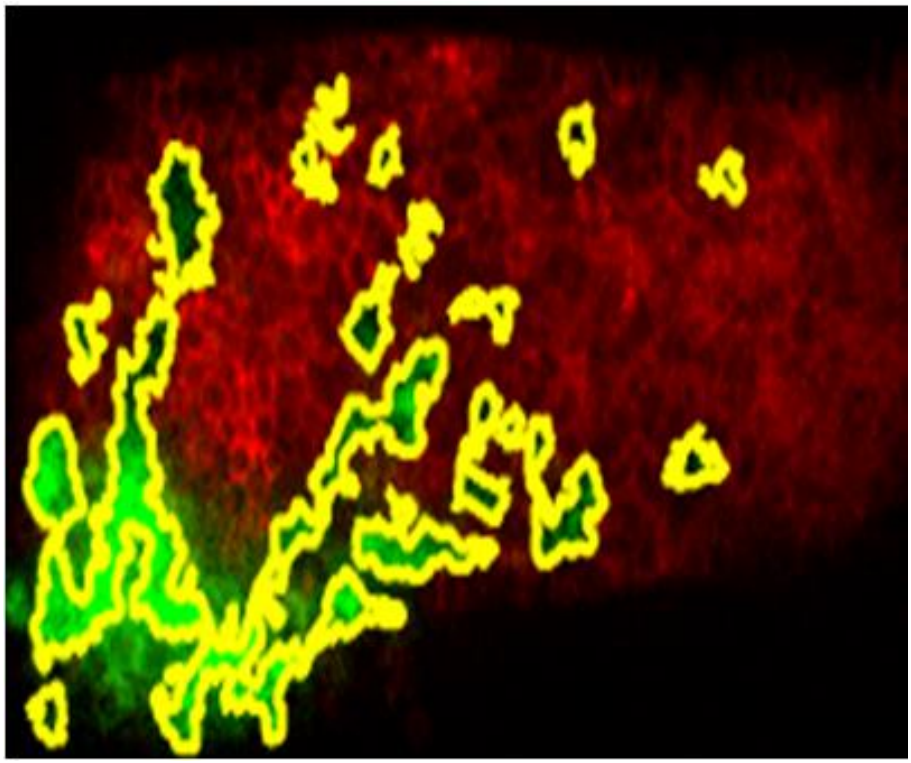

Figure 6.5 A fluorescent image of the core and shell. Core perimeter, outlined in yellow, resembles continuous protrusions rather than discrete cells (red=platelets imaged via anti-CD41, green=P-selectin imaged via anti-CD62P)

Again, video (https://vimeo.com/user92157740/review/302888572/43e0264dfc) shows a movie for the observation described in **Figure 6.5**.

Moreover, **Figure 6.6** shows heatmaps of cAlb retention half-lives[201] in a late stage clot structure. Such calculations consistently show patterns of what looks like a different material in the core and around the top of the thrombus (similar to **Figure 6.3** -

Right). This is consistent with our hypothesis about a gel emanating from the injury site and wrapping about the thrombus, as a result of the structural deformation after $t^{*}=1$. It would also explain how the shell is held together without platelet activation (i.e., the absence of P-selectin signal in the shell). The P-selectin expression in the shell may be diminished by the thinning of the gel strands and/or due to washing out by the blood flow.

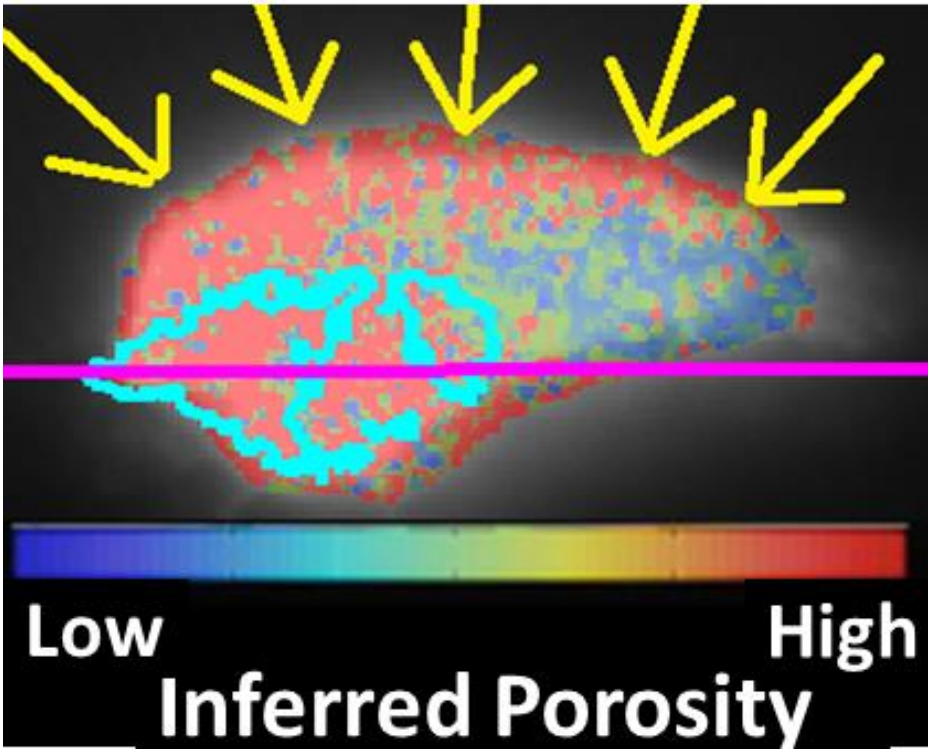

Figure 6.6 Color is a heatmap cAlb retention half-life (see Ref. *[201]* for more detail). Cyan outlines the core's perimeter (anti-CD62P fluorescence); Purple – marks the blood vessel wall, obtained visually; Yellow arrows point to regions of low porosity along the periphery of the shell.

Thus, our hypothesis is that there is an additional contribution of the EC material participating in the body of the clot. We suspect that it is this material that is responsible for the majority of the *early* P-selectin signal visible in the core.

6.5 Conclusions

In summary, we have hypothesized a thrombogenesis model that involves the participation of intra-EC material in the clot's core. This modification to the conventional model helps to explain why thrombi formation is not affected by extravascular flows of blood, which should entrain the platelet agonists responsible for activating the core. It also helps explain how the thrombus shell is held together, despite no apparent platelet activation being detected in this region of the clot. If correct, the presence of the EC material in the core could open up the possibilities for new drug targets, capable of selectively dissolving the dangerous shell, while leaving intact the useful core. This would serve a great benefit to the public health, given that pathogenic thrombosis is the leading cause of death worldwide. In the future, the hypothesized mechanism will be tested by labeling endothelial cells within the thrombus core with endothelial surface markers. This will help shed more light on previously reported observations. Also, the hypothesis will be further explored by developing a multiphase computational model which will incorporate platelet and gelatinous EC material, as well as the surrounding blood flow. Viscoelastic properties of clot used in the multiphase model will be calculated using yield stress estimates obtained in Chapter 5 and other constitutive equations. The ability of the model to reproduce observations from microscopy will serve to further validate the proposed mechanism.

CHAPTER 7

7 FUTURE WORK/CONCLUSIONS

7.1 Conclusions

In this work, the underlying goal was to resolve some of the unknown questions in two different biophysical application areas – Tissue Engineering and Thrombogenesis using image-based modeling. In the first application, numerical differences between two types of boundary conditions, the PBC and the WBC, which are commonly employed for performing RVE approximations in tissue engineering scaffold simulations was investigated. LBM fluid dynamics simulations were used to model the surface shear stresses in 3D scaffold reconstructions, obtained from high resolution microcomputed tomography images. It was found that, both of the RVE types followed the same *spatial* surface stress patterns as the whole scaffold simulations. However, they under-predicted the absolute stress values by an approximate factor of two. Moreover, it was found that the error grew with higher porosity of the scaffold. Thus showing dependence of RVE error on scaffold architecture. Additionally, it was found that the PBC always resulted in a better prediction (i.e., lower error) than the WBC. Therefore, the PBC is recommended as the boundary condition of choice for the RVE approximations.

In another tissue engineering study, the dependence of culture time on the distribution and magnitude of fluid shear in tissue scaffolds cultured under flow perfusion was investigated. In this study, following culture, constructs were either destructively evaluated with assays for cellularity and calcium deposition, imaged using μCT and reconstructed to allow for CFD simulations to be performed. It was found that both the

shear stress distributions and average shear stress within consistently increased with culture time. The observed increase in shear levels correlated with increasing levels of mineralized tissues within the scaffold constructs as seen in calcium deposition data and μCT reconstructions.

In the thrombogenesis application, detailed analysis of intravital microscopy images, showing thrombi development in response to laser-induced injuries in live mouse microvasculature was performed. Based on the results, it was found that the thrombus core does not change shape appreciably during thrombogenesis, but its shell does. Also, image-based LBM modeling was performed to calculate the fluid-induced shear stresses imposed on the thrombi's surfaces by the blood flow. From these results, it was shown that the thrombus shell experiences the highest fluid-induced shear stresses on its surface. Using results of the image-based modeling, estimates of the yield stress of thrombi formed in different blood vessels was obtained. It was found that thrombus yield strength and maximum size is correlated to blood vessel size.

Overall, the findings from this work reveal that image-based modeling is a versatile approach which can be applied to different biomedical application areas while overcoming the difficulties associated with conventional modeling.

7.2 Future Work

A limitation of the tissue engineering study presented in Chapter 3 is that it was performed on *empty* scaffolds, without any cells or tissues in them. In reality, the cells are likely to build tissues in preferred locations within the scaffolds. Thus, the observed flow fields will be different and effects of the RVEs should be quantified in greater detail in the locations

favored by the cells. Hence, studies should be performed on scaffolds with mineralized tissue/cell growth to see how much error is produced with RVE approximations. Also, in addition to stimulatory stresses, the flow field produced by the RVEs is often also used to model the influences of metabolite transport on the tissue growth. Therefore, the effects of the RVE cutouts and their boundary conditions on the mass transport within the scaffolds should be considered in future investigations.

In the second tissue engineering application presented in Chapter 4, an algorithm which can correlate tissue growth with stress distribution can be developed. This will potentially give researchers the ability to predict, for the culture period, fluid shear distributions in tissue engineered cultures using μCT images of empty scaffolds and CFD simulations on the 3D scaffold reconstructions.

Future directions for the study presented in Chapter 5 will include accounting for: (a) porous structure of thrombus, (b) blood escape from injury site, (c) deformations of blood vessel and (d) non-Newtonian nature of blood behavior in subsequent image-based thrombogenesis models. In addition, measurements of the blood flow forces experienced by occlusive and embolizing thrombi (both of which are harder to induce and capture experimentally) should be addressed in future investigations.

Overall, since image-based models utilize data from biomedical images. Their predictive capabilities can be improved by using higher resolution images. The imaging techniques used in studies reported in this work are limited by either or both imaging depth and resolution. Hence, the use of improved resolution light-based clinical imaging methods such as optical coherence tomography/OCT and enhancement of existing ones with newly developed contrast agents will enhance their capabilities. Also, super-resolution

microscopy methods which surpass diffraction limits imposed by conventional light microscopy techniques and are capable of even higher resolution should be used to obtain better images. Thus, amplifying the ability to create better image-based models. In addition to the aforementioned, with non-invasive imaging methods becoming more popular, image-based modeling is poised to become a mainstream tool for studying biological processes *in vivo*.

APPENDIX

SUPPLEMENTARY FIGURES FOR THROMBUS BIOMECHANICS

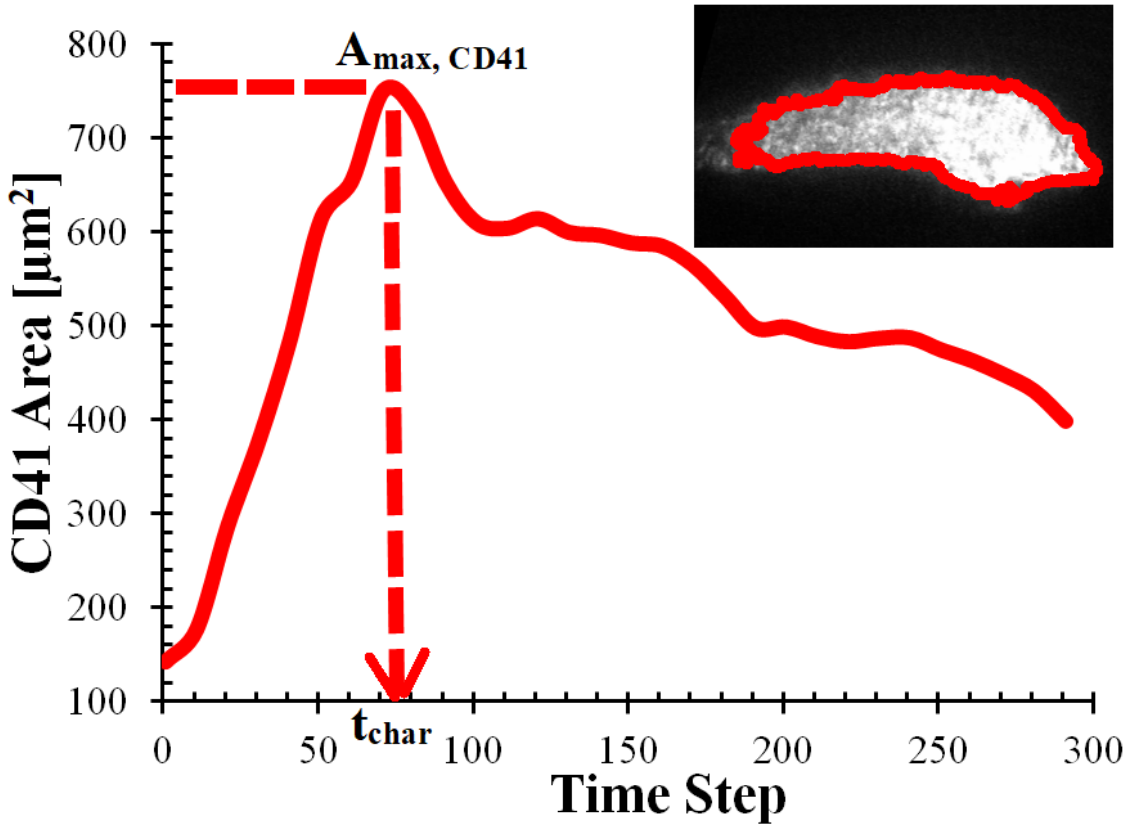

Figure A.1 Procedure for obtaining the maximum thrombus area and the characteristic time t_{char} at which it occurs. Inset in the upper right corner outlines the intravital microscopy image area used for the measurement for a typical experiment.

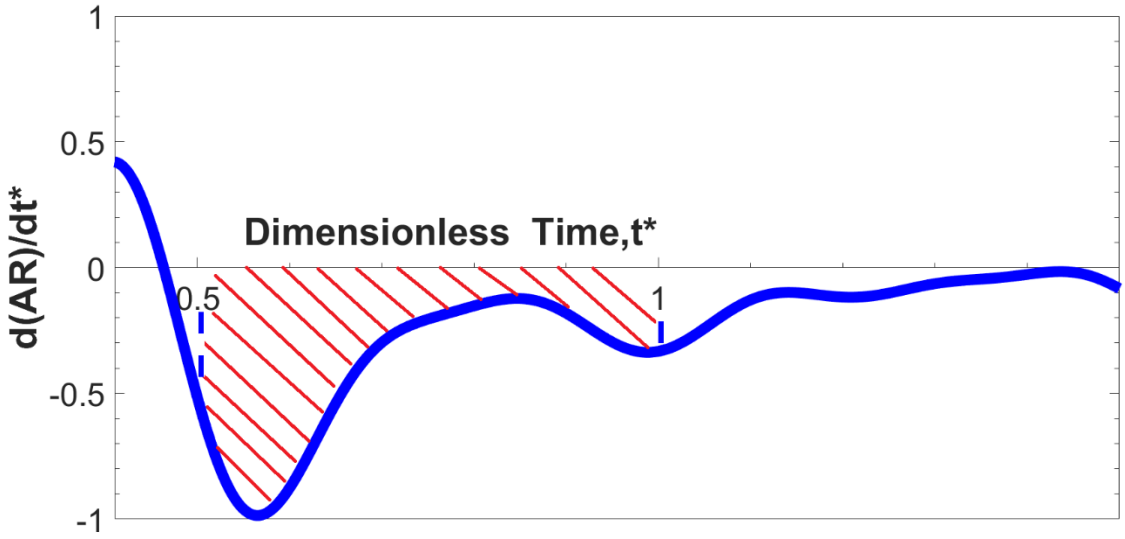

Figure A.2 Derivative of AR with respect to dimensionless time, showing that most of the negative AR slope (i.e., clot elongation) occurs between 0.5 < t* <= 1. The derivative is obtained by fitting a polynomial to the moving average AR data.

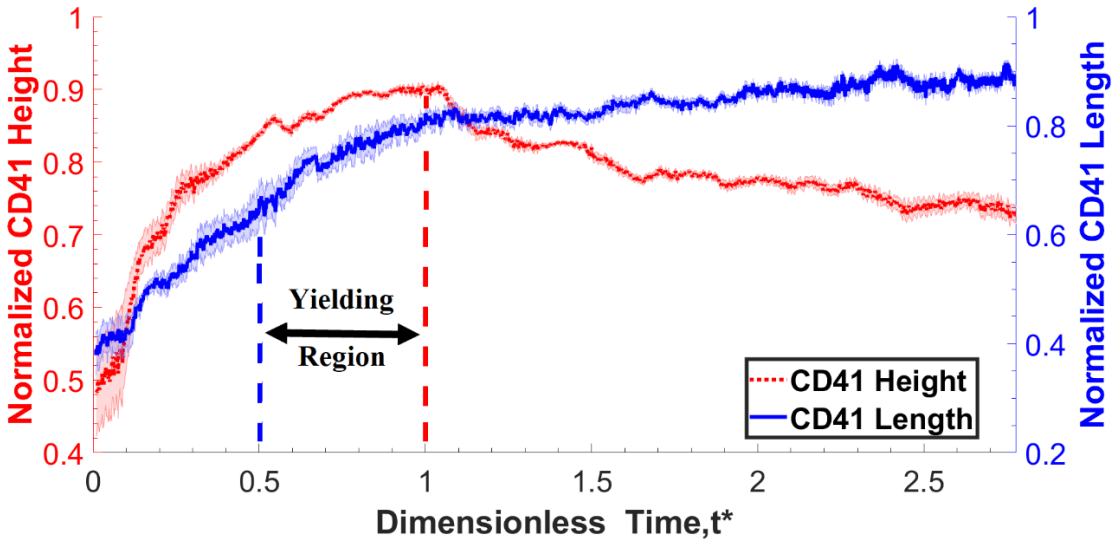

Figure A.3 Changes in the normalized thrombus height and length, as a function of the dimensionless time. Both curves are moving averages with a window of 0.5, and the error bars represent the moving variance for the 10 experiments in **Table 5.1**.

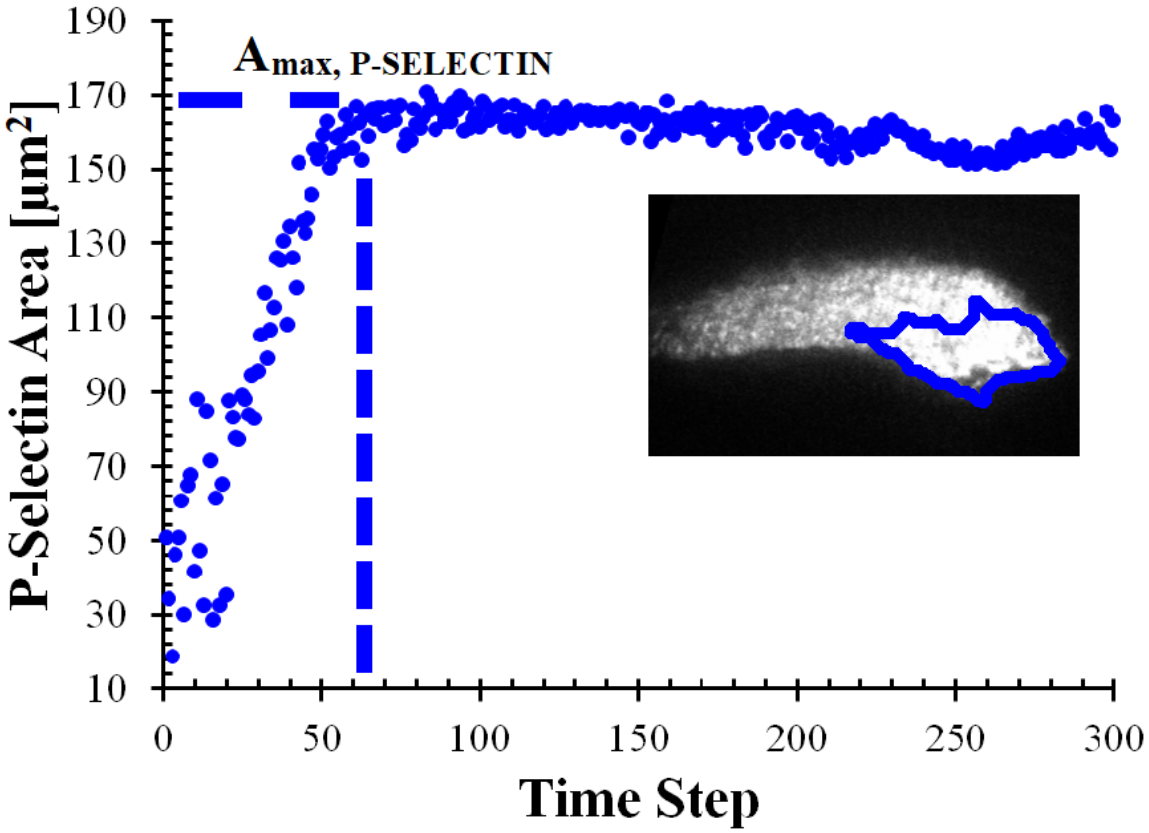

Figure A.4 Procedure for obtaining the maximum core area and the characteristic time t_{char} at which it occurs. Inset in the upper right corner outlines the intravital microscopy image area used for the measurement for a typical experiment.

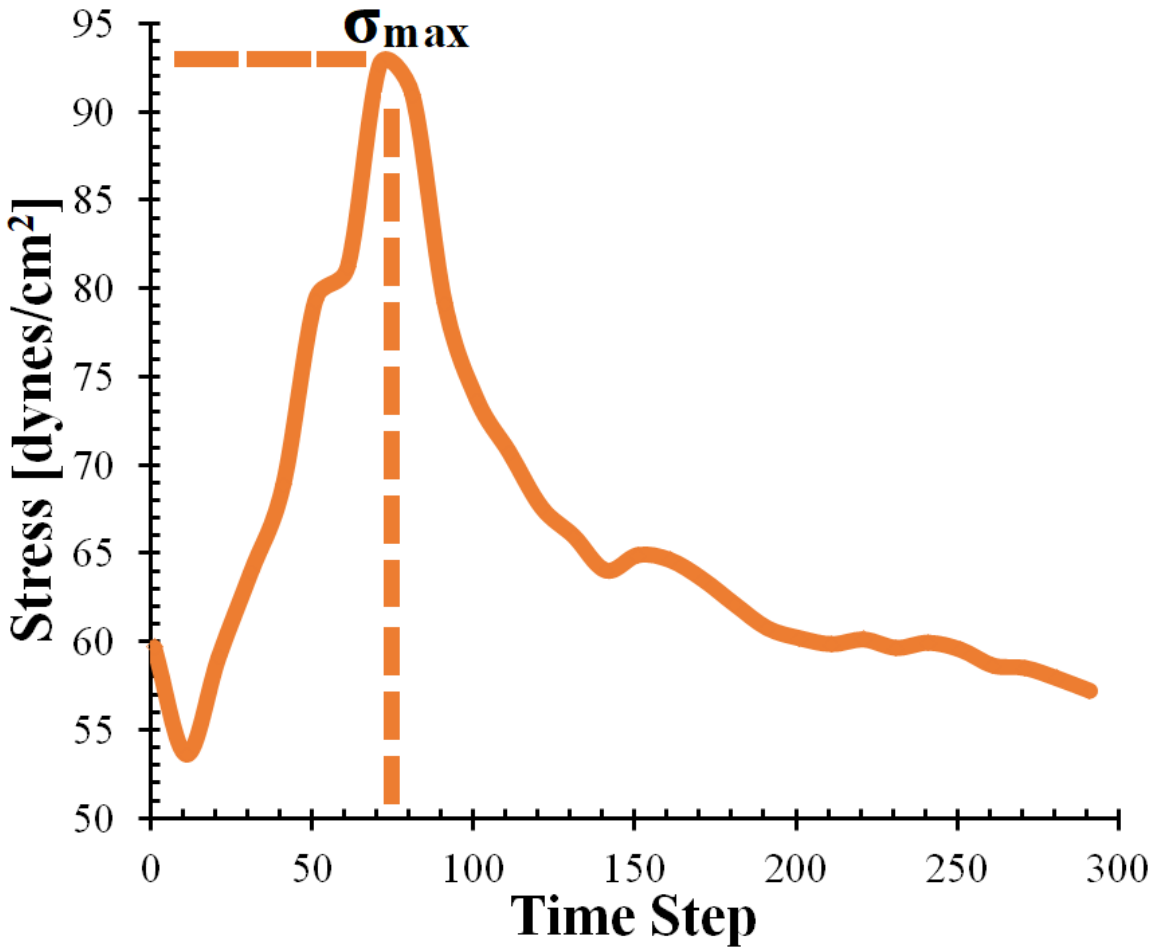

Figure A.5 Procedure for obtaining the maximum fluid induced stress experienced by clot. Data is shown for a typical LBM simulation.

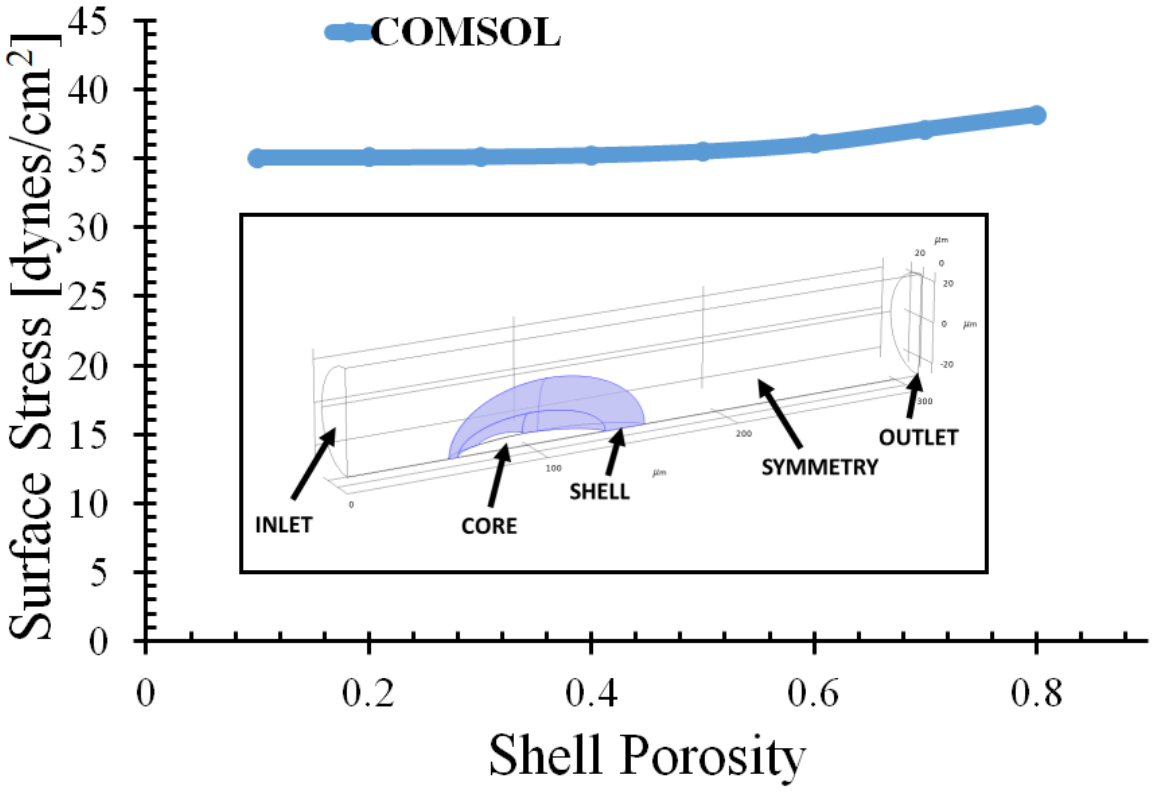

Figure A.6 COMSOL validation, demonstrating that varying the shell porosity does not significantly affect the fluid-induced stress imposed the clot's surface. Inset shows the COMSOL model setup, where the shell is filled with blue color.

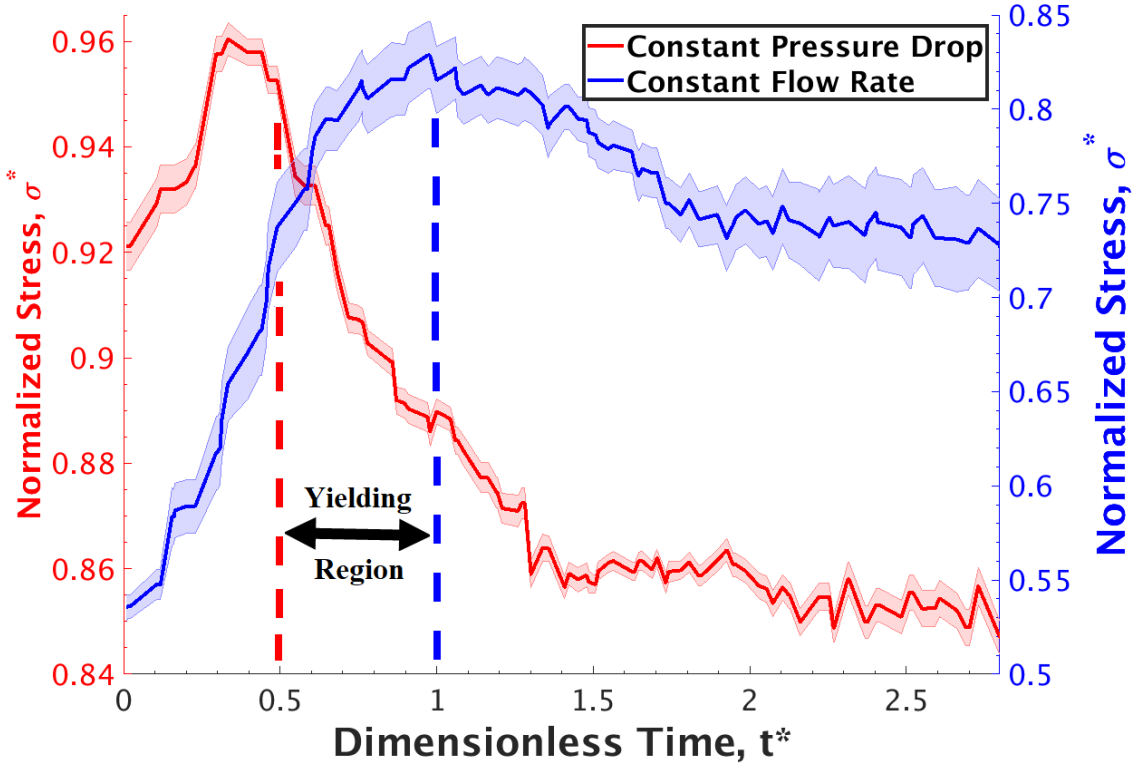

Figure A.7 Validation of **Figure 5.10** using an idealized thrombus model in COMSOL®: Normalized stress data, averaged over the thrombus surface, and plotted as a function of normalized time. Blue curve represents constant flow rate simulation results. Red curve represents constant pressure drop simulation. Abscissa is the dimensionless time; whose unity corresponds to the peak CD41 area in the red curve in **Figure 5.5**. Both curves are moving averages, with a window of 0.5; and the error bars represent the moving variance for the 10 experiments in **Table 5.1**. Thrombi core and shell are built using a combination of ellipsoids, whose dimensions are given by the clot's morphological properties measured from the intravital microscopy images.

REFERENCES

1. Costs of Chronic Diseases and Prevention. *Center for Disease Control and Prevention (CDC) Report*, 2017.

2. What is the impact of Chronic Diseases on America? *The Partnership To Fight Chronic Disease (TPTFCD) Report*, 2018.

3. *Heart Disease Facts (2015).* https://www.sciencedaily.com/releases/2016/03/160301114116.htm. Accessed 06/13/2017

4. Apostolidis, A.J. and A.N. Beris, Modeling of the blood rheology in steady-state shear flows. *Journal of Rheology*, 2014. **58**(3): p. 607-633.

5. Mittal, R., et al., Computational modeling of cardiac hemodynamics: Current status and future outlook. *Journal of Computational Physics*, 2016. **305**: p. 1065-1082.

6. Voronov, R.S., et al., Simulation of intrathrombus fluid and solute transport using in vivo clot structures with single platelet resolution. *Annals of Biomedical Engineering*, 2013. **41**(6): p. 1297-1307.

7. Fedosov, D.A., et al., Blood flow and cell-free layer in microvessels. *Microcirculation*, 2010. **17**(8): p. 615-28.

8. Kim, H.J., et al., Patient-Specific Modeling of Blood Flow and Pressure in Human Coronary Arteries. *Annals of Biomedical Engineering*, 2010. **38**(10): p. 3195-3209.

9. Kulp, S., et al. *Patient-specific modeling and visualization of blood flow through the heart*. in *2011 IEEE International Symposium on Biomedical Imaging: From Nano to Macro*. 2011.

10. Duanmu, Z., et al., A patient-specific lumped-parameter model of coronary circulation. *Scientific Reports*, 2018. **8**(1): p. 874.

11. Dobroserdova, T., et al., Patient-specific blood flow modelling for medical applications. *MATEC Web Conference*, 2016. **76**: p. 05001.

12. Jiwoong, C., et al., MDCT-Based 3D-1D Coupled Airflow Simulation In The Entire Conducting Airway Of Breathing Human Lung, in *A66. Modeling, Mechanics and Gas Exchange*. 2012, American Thoracic Society. p. A2078-A2078.

13. Lambert, A.R., et al., Regional deposition of particles in an image-based airway model: large-eddy simulation and left-right lung ventilation asymmetry. *Aerosol science and technology: The Journal of the American Association for Aerosol Research*, 2011. **45**(1): p. 11-25.

14. Tawhai, M.H., et al., CT-based geometry analysis and finite element models of the human and ovine bronchial tree. *Journal of Applied Physiology (1985)*, 2004. **97**(6): p. 2310-21.

15. Yin, Y., et al., A multiscale MDCT image-based breathing lung model with time-varying regional ventilation. *Journal of Computional Physics*, 2013. **244**: p. 168-192.

16. Patel, T.R., et al., Modeling congenital nasal pyriform aperture stenosis using computational fluid dynamics. *International Journal of Pediatric Otorhinolaryngology*, 2018. **109**: p. 180-184.

17. Linninger, A.A., et al., A mathematical model of blood, cerebrospinal fluid and brain dynamics. *Journal of Mathematical Biology*, 2009. **59**(6): p. 729-759.

18. Sweetman, B., et al., Three-dimensional computational prediction of cerebrospinal fluid flow in the human brain. *Computers in Biology and Medicine*, 2011. **41**(2): p. 67-75.

19. Perdikaris, P., L. Grinberg, and G.E. Karniadakis, Multiscale modeling and simulation of brain blood flow. *Physics of Fluids*, 2016. **28**(2): p. 021304.

20. BCA-Research, *Human Intelligence And Economic Growth From 50,000 B.C. To The Singularity*, in *The BCA Blog*, B. Peter, Editor. 2013, BCA Research: www.bcaresearch.com.

21. Jung, K.-H. and K.-H. Lee, Molecular Imaging in the Era of Personalized Medicine. *Journal of Pathology and Translational Medicine*, 2015. **49**(1): p. 5-12.

22. Kherlopian, A.R., et al., A review of imaging techniques for systems biology. *BMC Systems Biology*, 2008. **2**(1): p. 74.

23. Hong, G., et al., Multifunctional in vivo vascular imaging using near-infrared II fluorescence. *Nature Medicine*, 2012. **18**: p. 1841.

24. Kriegeskorte, N. and P. Bandettini, Analyzing for information, not activation, to exploit high-resolution fMRI. *NeuroImage*, 2007. **38**(4): p. 649-662.

25. Lamata, P., et al., Images as drivers of progress in cardiac computational modelling. *Progress in Biophysics and Molecular Biology*, 2014. **115**(2–3): p. 198-212.

26. Fred, H.L., Drawbacks and Limitations of Computed Tomography: Views from a Medical Educator. *Texas Heart Institute Journal*, 2004. **31**(4): p. 345-348.

27. Hallouard, F., et al., Iodinated blood pool contrast media for preclinical X-ray imaging applications – A review. *Biomaterials*, 2010. **31**(24): p. 6249-6268.

28. Schambach, S.J., et al., Application of micro-CT in small animal imaging. *Methods*, 2010. **50**(1): p. 2-13.

29. Laskey, M.A., Dual-energy X-ray absorptiometry and body composition. *Nutrition*, 1996. **12**(1): p. 45-51.

30. Pirayesh Islamian, J., et al., Comparison between the MDCT and the DXA scanners in the evaluation of BMD in the lumbar spine densitometry. *The Egyptian Journal of Radiology and Nuclear Medicine*.

31. Lusic, H. and M.W. Grinstaff, X-ray-Computed Tomography Contrast Agents. *Chemical Reviews*, 2013. **113**(3): p. 1641-1666.

32. Silvast, T.S., et al., Contrast agent-enhanced computed tomography of articular cartilage: Association with tissue composition and properties. *Acta Radiologica*, 2009. **50**(1): p. 78-85.

33. Adams, J.E., Quantitative computed tomography. *European Journal of Radiology*, 2009. **71**(3): p. 415-424.

34. Kazerooni, E.A., High-Resolution CT of the Lungs. *American Journal of Roentgenology*, 2001. **177**(3): p. 501-519.

35. Burghardt, A.J., T.M. Link, and S. Majumdar, High-resolution Computed Tomography for Clinical Imaging of Bone Microarchitecture. *Clinical Orthopaedics and Related Research*, 2011. **469**(8): p. 2179-2193.

36. Condeelis, J. and R. Weissleder, In vivo imaging in cancer. *Cold Spring Harbor perspectives in Biology*, 2010. **2**(12): p. a003848-a003848.

37. Xiang, L., et al., 4-D Photoacoustic Tomography. *Scientific Reports*, 2013. **3**: p. 1113.

38. Fujimoto, J.G., et al., Optical Coherence Tomography: An Emerging Technology for Biomedical Imaging and Optical Biopsy. *Neoplasia (New York, N.Y.)*, 2000. **2**(1-2): p. 9-25.

39. Osiac, E., et al., Optical coherence tomography and Doppler optical coherence tomography in the gastrointestinal tract. *World Journal of Gastroenterology : WJG*, 2011. **17**(1): p. 15-20.

40. Steinman, D., Image-Based Computational Fluid Dynamics Modeling in Realistic Arterial Geometries. *Annals of Biomedical Engineering*, 2002. **30**(4): p. 483-497.

41. Hides, J.A., C.A. Richardson, and G.A. Jull, Use of real-time ultrasound imaging for feedback in rehabilitation. *Manual Therapy*, 1998. **3**(3): p. 125-131.

42. Uemura, H., et al., Usefulness of perflubutane microbubble-enhanced ultrasound in imaging and detection of prostate cancer: phase II multicenter clinical trial. *World Journal of Urology*, 2013. **31**(5): p. 1123-1128.

43. Nwaneshiudu, A., et al., Introduction to Confocal Microscopy. *Journal of Investigative Dermatology*, 2012. **132**(12): p. 1-5.

44. Rosenegger, D.G., et al., A High Performance, Cost-Effective, Open-Source Microscope for Scanning Two-Photon Microscopy that Is Modular and Readily Adaptable. *PLOS ONE*, 2014. **9**(10): p. e110475.

45. Yao, J. and L.V. Wang, Photoacoustic Microscopy. *Laser & Photonics Reviews*, 2013. **7**(5): p. 10.1002/lpor.201200060.

46. Butt, H.-J., B. Cappella, and M. Kappl, Force measurements with the atomic force microscope: Technique, interpretation and applications. *Surface Science Reports*, 2005. **59**(1–6): p. 1-152.

47. Hein, B., K.I. Willig, and S.W. Hell, Stimulated emission depletion (STED) nanoscopy of a fluorescent protein-labeled organelle inside a living cell. *Proceedings of the National Academy of Sciences*, 2008. **105**(38): p. 14271-14276.

48. Fornasiero, E.F. and F. Opazo, Super-resolution imaging for cell biologists. *BioEssays*, 2015. **37**(4): p. 436-451.

49. MacDonald, L., G. Baldini, and B. Storrie, Does Super Resolution Fluorescence Microscopy Obsolete Previous Microscopic Approaches to Protein Co-localization? *Methods in molecular biology (Clifton, N.J.)*, 2015. **1270**: p. 255-275.

50. Betzig, E., et al., Imaging Intracellular Fluorescent Proteins at Nanometer Resolution. *Science*, 2006. **313**(5793): p. 1642-1645.

51. Wilson, S.M. and A. Bacic, Preparation of plant cells for transmission electron microscopy to optimize immunogold labeling of carbohydrate and protein epitopes. *Nature Protocols*, 2012. **7**: p. 1716.

52. Chen, B.-C., et al., Lattice light-sheet microscopy: Imaging molecules to embryos at high spatiotemporal resolution. *Science*, 2014. **346**(6208).

53. Legant, W.R., et al., High-density three-dimensional localization microscopy across large volumes. *Nature Methods*, 2016. **13**: p. 359.

54. Soliman, D., et al., Combining microscopy with mesoscopy using optical and optoacoustic label-free modes. *Scientific Reports*, 2015. **5**: p. 12902.

55. Huang, B., et al., Three-dimensional super-resolution imaging by stochastic optical reconstruction microscopy. *Science*, 2008. **319**(5864): p. 810-813.

56. Wang, J., et al., Domain-decomposition method for parallel lattice Boltzmann simulation of incompressible flow in porous media. *Physical Review E*, 2005. **72**(1): p. 016706.

57. Papavassiliou, D.V., et al., Chapter 23 - Lattice Boltzmann Methods for Bioengineering Applications, in *Numerical Methods and Advanced Simulation in Biomechanics and Biological Processes*. 2018, Academic Press. p. 415-429.

58. Arumuga Perumal, D. and A.K. Dass, A Review on the development of lattice Boltzmann computation of macro fluid flows and heat transfer. *Alexandria Engineering Journal*, 2015. **54**(4): p. 955-971.

59. Chen, S. and G.D. Doolen, Lattice Boltzmann method for fluid flows. *Annual Review of Fluid Mechanics*, 1998. **30**: p. 329-364.

60. Succi, S., The Lattice Boltzmann Equation for Fluid Dynamic and Beyond. 2001, New York: Oxford University Press.

61. Sukop, M.C. and D.T. Thorne, Lattice Boltzmann Modeling: An Introduction for Geoscientists and Engineers. 1st ed. 2006, NewYork: Springer.

62. Aidun, C.K. and J.R. Clausen, Lattice-Boltzmann method for complex flows. *Annual Review of Fluid Mechanics*, 2010. **42**(1): p. 439-472.

63. Lallemand, P. and L.-S. Luo, Theory of the lattice Boltzmann method: Dispersion, dissipation, isotropy, Galilean invariance, and stability. *Physical Review E*, 2000. **61**(6): p. 6546-6562.

64. Cosgrove, J.A., et al., Application of the lattice Boltzmann method to transition in oscillatory channel flow. *Journal of Physics A: Mathematical and General*, 2003. **36**(10): p. 2609.

65. Swift, M.R., et al., Lattice Boltzmann simulations of liquid-gas and binary fluid systems. *Physical Review E*, 1996. **54**(5): p. 5041-5052.

66. Ledesma-Aguilar, R., D. Vella, and J.M. Yeomans, Lattice-Boltzmann simulations of droplet evaporation. *Soft Matter*, 2014. **10**(41): p. 8267-8275.

67. Gabbanelli, S., G. Drazer, and J. Koplik, Lattice Boltzmann method for non-Newtonian (power-law) fluids. *Physical Review E*, 2005. **72**(4): p. 046312.

68. Yoshino, M., et al., A numerical method for incompressible non-Newtonian fluid flows based on the lattice Boltzmann method. *Journal of Non-Newtonian Fluid Mechanics*, 2007. **147**(1–2): p. 69-78.

69. Boyd, J., J. Buick, and S. Green, A second-order accurate lattice Boltzmann non-Newtonian flow model. *Journal of Physics A: Mathematical and General*, 2006. **39**(46): p. 14241.

70. Freitas, R.K. and W. Schröder, Numerical investigation of the three-dimensional flow in a human lung model. *Journal of Biomechanics*, 2008. **41**(11): p. 2446-2457.

71. Kadri, O.E., et al., Numerical Accuracy Comparison of Two Boundary Conditions Commonly used to Approximate Shear Stress Distributions in Tissue Engineering Scaffolds Cultured under Flow Perfusion. *International Journal for Numerical Methods in Biomedical Engineering*, 2018. **34**(11): p. e3132.

72. Williams, C., et al., Time-Dependent Shear Stress Distributions during Extended Flow Perfusion Culture of Bone Tissue Engineered Constructs. *Fluids*, 2018. **3**(2): p. 25.

73. VanGordon, S.B., et al., Effects of Scaffold Architecture on Preosteoblastic Cultures under Continuous Fluid Shear. *Industrial & Engineering Chemistry Research*, 2011. **50**(2): p. 620-629.

74. Voronov, R., et al., Computational modeling of flow-induced shear stresses within 3D salt-leached porous scaffolds imaged via micro-CT. *Journal of Biomechanics*, 2010. **43**(7): p. 1279-86.

75. Voronov, R.S., et al., Distribution of flow-induced stresses in highly porous media. *Applied Physics Letters*, 2010. **97**(2): p. 024101.

76. Voronov, R.S., et al., Efficient Lagrangian scalar tracking method for reactive local mass transport simulation through porous media. *International Journal for Numerical Methods in Fluids*, 2011. **67**(4): p. 501-517.

77. Pham, N.H., et al., Bulk stress distributions in the pore space of sphere-packed beds under Darcy flow conditions. *Physical Review E: Statistical Nonlinear Soft Matter Physics*, 2014. **89**(3): p. 033016.

78. Pham, N.H., et al., Predicting the stress distribution within scaffolds with ordered architecture. *Biorheology*, 2012. **49**(4): p. 235-247.

79. Kolmakov, G.V., et al., Using nanoparticle-filled microcapsules for site-specific healing of damaged substrates: creating a “repair-and-go” system. *ACS Nano*, 2010. **4**(2): p. 1115-1123.

80. Buxton, G.A., et al., Newtonian fluid meets an elastic solid: Coupling lattice Boltzmann and lattice-spring models. *Physical Review E*, 2005. **71**(5): p. 056707.

81. Kwon, Y.W., Development of coupling technique for LBM and FEM for FSI application. *Engineering Computations*, 2006. **23**(8): p. 860-875.

82. Buxton, G.A., C.M. Care, and D.J. Cleaver, A lattice spring model of heterogeneous materials with plasticity. *Modelling and Simulation in Materials Science and Engineering*, 2001. **9**(6): p. 485.

83. Pham, N.H. and D.V. Papavassiliou, Nanoparticle transport in heterogeneous porous media with particle tracking numerical methods. *Computational Particle Mechanics*, 2017. **4**(1): p. 87-100.

84. McNamara, G.R. and G. Zanetti, Use of the Boltzmann-equation to simulate lattice-gas automata. *Physical Review Letters*, 1988. **61**(20): p. 2332-2335.

85. Koelman, J.M.V.A., A simple lattice Boltzmann scheme for Navier-Stokes fluid flow. *Europhysics Letters*, 1991. **15**(6): p. 603.

86. Bhatnagar, P.L., E.P. Gross, and M. Krook, A Model for Collision Processes in Gases. I. Small Amplitude Processes in Charged and Neutral One-Component Systems. *Physical Review*, 1954. **94**(3): p. 511-525.

87. Du, R. and B.-C. Shi, Incompressible multi-relaxation-time lattice Boltzmann model in 3-D space. *Journal of Hydrodynamics, Ser. B*, 2010. **22**(6): p. 782-787.

88. Qian, Y.H., D. D'Humières, and P. Lallemand, Lattice BGK models for Navier-Stokes equation. *Europhysics Letters*, 1992. **17**(6): p. 479-484.

89. Noble, D.R., et al., A consistent hydrodynamic boundary condition for the lattice Boltzmann method. *Physics of Fluids*, 1995. **7**(1): p. 203-209.

90. Kutay, M.E., A.H. Aydilek, and E. Masad, Laboratory validation of lattice Boltzmann method for modeling pore-scale flow in granular materials. *Computers and Geotechnics*, 2006. **33**(8): p. 381-395.

91. Zou, Q. and X. He, On pressure and velocity boundary conditions for the lattice Boltzmann BGK model. *Physics of Fluids*, 1997. **9**(6): p. 1591-1598.

92. Kim, S.H. and H. Pitsch, A generalized periodic boundary condition for lattice Boltzmann method simulation of a pressure driven flow in a periodic geometry. *Physics of Fluids*, 2007. **19**(10): p. 108101.

93. Hashemi, Z., Chapter 22 - The Lattice Boltzmann Modeling: Solving Complex Flows Including Biological Cells, in *Numerical Methods and Advanced Simulation in Biomechanics and Biological Processes*, M. Cerrolaza, S.J. Shefelbine, and D. Garzón-Alvarado, Editors. 2018, Academic Press. p. 391-414.

94. Voronov, R., *Fluid Shear Stress and Nutrient Transport effects via Lattice-Boltzmann and Lagrangian Scalar Tracking Simulations of cell culture media perfusion through artificial bone engineering constructs imaged with microCT[PhD Thesis]*, in *School of Chemical,Biological and materials Engineering*. 2010, University of Oklahoma. p. 131.

95. Velivelli, A.C. and K.M. Bryden, Domain decomposition based coupling between the lattice Boltzmann method and traditional CFD methods—Part I: Formulation and application to the 2-D Burgers' equation. *Advances in Engineering Software*, 2014. **70**: p. 104-112.

96. Park, H., J.H. Park, and S.J. Lee, In vivo measurement of hemodynamic information in stenosed rat blood vessels using X-ray PIV. *Scientific Reports*, 2016. **6**: p. 37985.

97. Sikavitsas, V.I., et al., Mineralized matrix deposition by marrow stromal osteoblasts in 3D perfusion culture increases with increasing fluid shear forces. *Proceedings of the National Academy of Sciences*, 2003. **100**(25): p. 14683-14688.

98. Porter, B., et al., 3-D computational modeling of media flow through scaffolds in a perfusion bioreactor. *Journal of Biomechanics*, 2005. **38**(3): p. 543-549.

99. American Academy of Orthopaedic Surgeons, A.A.O.S. *One in two Americans have a musculoskeletal condition*. ScienceDaily [Science News] 2016 https://www.sciencedaily.com/releases/2016/03/160301114116.htm. Accessed 06/13/2017

100. Black, C.R.M., et al., Bone Tissue Engineering. *Current Molecular Biology Reports*, 2015. **1**(3): p. 132-140.

101. C., D., et al., Bone allografts. *The Journal of Bone and Joint Surgery. British volume*, 2007. **89-B**(5): p. 574-580.

102. Graham, S.M., et al., Biological therapy of bone defects: the immunology of bone allo-transplantation. *Expert Opinion on Biological Therapy*, 2010. **10**(6): p. 885-901.

103. Verbruggen, S.W., T.J. Vaughan, and L.M. McNamara, Fluid flow in the osteocyte mechanical environment: a fluid-structure interaction approach. *Biomechanics and Modeling in Mechanobiology*, 2014. **13**(1): p. 85-97.

104. Guyot, Y., et al., A three-dimensional computational fluid dynamics model of shear stress distribution during neotissue growth in a perfusion bioreactor. *Biotechnology and Bioengineering*, 2015. **112**(12): p. 2591-600.

105. Miyashita, S., et al., Mechanical forces induce odontoblastic differentiation of mesenchymal stem cells on three-dimensional biomimetic scaffolds. *Journal of Tissue Engineering and Regenerative Medicine*, 2017. **11**(2): p. 434-446.

106. Zhao, F., T.J. Vaughan, and L.M. McNamara, Quantification of fluid shear stress in bone tissue engineering scaffolds with spherical and cubical pore architectures. *Biomechanics and Modeling in Mechanobiology*, 2016. **15**(3): p. 561-577.

107. Yourek, G., et al., Shear stress induces osteogenic differentiation of human mesenchymal stem cells. *Regenerative Medicine*, 2010. **5**(5): p. 713-724.

108. Stolberg, S. and K.E. McCloskey, Can shear stress direct stem cell fate? *Biotechnology Progress*, 2009. **25**(1): p. 10-19.

109. Raimondi, M.T., et al., The effect of hydrodynamic shear on 3D engineered chondrocyte systems subject to direct perfusion. *Biorheology*, 2006. **43**(3-4): p. 215-22.

110. Kim, K.M., et al., Shear Stress Induced by an Interstitial Level of Slow Flow Increases the Osteogenic Differentiation of Mesenchymal Stem Cells through TAZ Activation. *PLOS ONE*, 2014. **9**(3): p. e92427.

111. Brindley, D., et al., Bioprocess Forces and Their Impact on Cell Behavior: Implications for Bone Regeneration Therapy. *Journal of Tissue Engineering*, 2011. **2011**: p. 620247.

112. Alvarez-Barreto, J.F., et al., Flow Perfusion Improves Seeding of Tissue Engineering Scaffolds with Different Architectures. *Annals of Biomedical Engineering*, 2007. **35**(3): p. 429-442.

113. Guyot, Y., et al., Coupling curvature-dependent and shear stress-stimulated neotissue growth in dynamic bioreactor cultures: a 3D computational model of a complete scaffold. *Biomechanics and Modeling in Mechanobiology*, 2016. **15**(1): p. 169-180.

114. Hossain, M.S., D.J. Bergstrom, and X.B. Chen, Prediction of cell growth rate over scaffold strands inside a perfusion bioreactor. *Biomechanics and Modeling in Mechanobiology*, 2015. **14**(2): p. 333-344.

115. Bergemann, C., et al., Cellular Nutrition in Complex Three-Dimensional Scaffolds: A Comparison between Experiments and Computer Simulations. *International Journal of Biomaterials*, 2015. **2015**: p. 584362.

116. Olivares, A.L., et al., Finite element study of scaffold architecture design and culture conditions for tissue engineering. *Biomaterials*, 2009. **30**(30): p. 6142-6149.

117. Chen, Y., et al., Design Optimization of Scaffold Microstructures Using Wall Shear Stress Criterion Towards Regulated Flow-Induced Erosion. *Journal of Biomechanical Engineering*, 2011. **133**(8): p. 081008-081008-10.

118. Ali, D. and S. Sen, Finite element analysis of mechanical behavior, permeability and fluid induced wall shear stress of high porosity scaffolds with gyroid and lattice-based architectures. *Journal of the Mechanical Behavior of Biomedical Materials*, 2017. **75**: p. 262-270.

119. Maes, F., et al., Computational models for wall shear stress estimation in scaffolds: a comparative study of two complete geometries. *Journal of Biomechanics*, 2012. **45**(9): p. 1586-92.

120. Maes, F., et al., Modeling fluid flow through irregular scaffolds for perfusion bioreactors. *Biotechnology and Bioengineering*, 2009. **103**(3): p. 621-630.

121. Cioffi, M., et al., Modeling evaluation of the fluid-dynamic microenvironment in tissue-engineered constructs: A micro-CT based model. *Biotechnology and Bioengineering*, 2006. **93**(3): p. 500-510.

122. Cioffi, M., et al., Computational evaluation of oxygen and shear stress distributions in 3D perfusion culture systems: Macro-scale and micro-structured models. *Journal of Biomechanics*, 2008. **41**(14): p. 2918-2925.

123. Hendrikson, W.J., et al., Influence of Additive Manufactured Scaffold Architecture on the Distribution of Surface Strains and Fluid Flow Shear Stresses and Expected Osteochondral Cell Differentiation. *Frontiers in Bioengineering and Biotechnology*, 2017. **5**(6).

124. Zermatten, E., et al., Micro-Computed Tomography Based Computational Fluid Dynamics for the Determination of Shear Stresses in Scaffolds Within a Perfusion Bioreactor. *Annals of Biomedical Engineering*, 2014. **42**(5): p. 1085-1094.

125. Jungreuthmayer, C., et al., A comparative study of shear stresses in collagen-glycosaminoglycan and calcium phosphate scaffolds in bone tissue-engineering bioreactors. *Tissue Engineering Part A*, 2009. **15**(5): p. 1141-9.

126. Campos Marin, A. and D. Lacroix, The inter-sample structural variability of regular tissue-engineered scaffolds significantly affects the micromechanical local cell environment. *Interface Focus*, 2015. **5**(2).

127. Liu, B., et al., Perfusion applied to a 3D model of bone metastasis results in uniformly dispersed mechanical stimuli. *Biotechnology and Bioengineering*, 2017: p. 1-10.

128. Wu, P.-H., et al., Three-dimensional cell migration does not follow a random walk. *Proceedings of the National Academy of Sciences of the United States of America*, 2014. **111**(11): p. 3949-3954.

129. Simmons, A.D., et al., Sensing metabolites for the monitoring of tissue engineered construct cellularity in perfusion bioreactors. *Biosensors and Bioelectronics*, 2017. **90**: p. 443-449.

130. Du, X. and M. Ostoja-Starzewski, On the size of representative volume element for Darcy law in random media. *Proceedings of the Royal Society A: Mathematical, Physical and Engineering Science*, 2006. **462**(2074): p. 2949.

131. Shakhawath Hossain, M., D.J. Bergstrom, and X.B. Chen, A mathematical model and computational framework for three-dimensional chondrocyte cell growth in a porous tissue scaffold placed inside a bi-directional flow perfusion bioreactor. *Biotechnology and Bioengineering*, 2015. **112**(12): p. 2601-2610.

132. Alam, T.A., et al., Image-based modeling: A novel tool for realistic simulations of artificial bone cultures. *Technology*, 2016. **04**(04): p. 229-233.

133. Lakhotia, S. and E.T. Papoutsakis, Agitation Induced Cell Injury in Microcarrier Cultures - Protective Effect of Viscosity Is Agitation Intensity Dependent - Experiments and Modeling. *Biotechnology and Bioengineering*, 1992. **39**(1): p. 95-107.

134. Wyllie, M.R.J. and W.D. Rose, Application of the Kozeny Equation to Consolidated Porous Media. *Nature*, 1950. **165**: p. 972.

135. Ozgumus, T., M. Mobedi, and U. Ozkol, Determination of Kozeny Constant Based on Porosity and Pore to Throat Size Ratio in Porous Medium with Rectangular Rods. *Engineering Applications of Computational Fluid Mechanics*, 2014. **8**(2): p. 308-318.

136. Bacabac, R.G., et al., Nitric oxide production by bone cells is fluid shear stress rate dependent. *Biochemical and Biophysical Research Communications*, 2004. **315**(4): p. 823-829.

137. Bakker, A.D., et al., The production of nitric oxide and prostaglandin E_2 by primary bone cells is shear stress dependent. *Journal of Biomechanics*, 2001. **34**(5): p. 671-677.

138. Kim, J.-H., J.A. Ochoa, and S. Whitaker, Diffusion in anisotropic porous media. *Transport in Porous Media*, 1987. **2**(4): p. 327-356.

139. Efendiev, Y. and T. Hou, Multiscale Finite Element Methods. 1st ed. *Surveys and Tutorials in the Applied Mathematical Sciences*. Vol. 4. 2009, New York: Springer-Verlag New York. XII, 234.

140. Van Bael, S., et al., The effect of pore geometry on the in vitro biological behavior of human periosteum-derived cells seeded on selective laser-melted Ti6Al4V bone scaffolds. *Acta Biomaterialia*, 2012. **8**(7): p. 2824-2834.

141. Habashi Fathi and H.M. M., Computational Fluid Dynamics Techniques. 1995: CRC Press. 872.

142. VanGordon, S.B., *Three-Dimensional Bone Tissue Engineering Strategies Using Polymeric Scaffolds.* 2012, University of Oklahoma,Norman Ok,USA.

143. Melchels, F.P.W., et al., The influence of the scaffold design on the distribution of adhering cells after perfusion cell seeding. *Biomaterials*, 2011. **32**(11): p. 2878-2884.

144. Alvarez-Barreto, J.F. and V.I. Sikavitsas, Improved Mesenchymal Stem Cell Seeding on RGD-Modified Poly(L-lactic acid) Scaffolds using Flow Perfusion. *Macromolecular Bioscience*, 2007. **7**(5): p. 579-588.

145. Du, D., K.S. Furukawa, and T. Ushida, 3D culture of osteoblast-like cells by unidirectional or oscillatory flow for bone tissue engineering. *Biotechnology and Bioengineering*, 2009. **102**(6): p. 1670-1678.

146. Papantoniou, I., et al., Spatial optimization in perfusion bioreactors improves bone tissue-engineered construct quality attributes. *Biotechnology and Bioengineering*, 2014. **111**(12): p. 2560-2570.

147. Campolo, M., F. Curcio, and A. Soldati, Minimal perfusion flow for osteogenic growth of mesenchymal stem cells on lattice scaffolds. *AIChE Journal*, 2013. **59**(8): p. 3131-3144.

148. Sandino, C., et al., Simulation of angiogenesis and cell differentiation in a CaP scaffold subjected to compressive strains using a lattice modeling approach. *Biomaterials*, 2010. **31**(8): p. 2446-2452.

149. Nava, M.M., M.T. Raimondi, and R. Pietrabissa, A multiphysics 3D model of tissue growth under interstitial perfusion in a tissue-engineering bioreactor. *Biomechanics and Modeling in Mechanobiology* 2013. **12**.

150. Checa, S. and P.J. Prendergast, A Mechanobiological Model for Tissue Differentiation that Includes Angiogenesis: A Lattice-Based Modeling Approach. *Annals of Biomedical Engineering*, 2009. **37**(1): p. 129-145.

151. Childers, E.P., et al., 3D printing of resorbable poly(propylene fumarate) tissue engineering scaffolds. *MRS Bulletin*, 2015. **40**(2): p. 119-126.

152. Voronov, R.S., et al., 3D Tissue-Engineered Construct Analysis via Conventional High-Resolution Microcomputed Tomography Without X-Ray Contrast. *Tissue Engineering Part C: Methods*, 2012. **19**(5): p. 327-335.

153. Kasper, F.K., et al., Flow Perfusion Culture of Mesenchymal Stem Cells for Bone Tissue Engineering. *StemBook*. 2008: Harvard Stem Cell Institute,Cambridge.

154. Bancroft, G.N., et al., Fluid flow increases mineralized matrix deposition in 3D perfusion culture of marrow stromal osteoblasts in a dose-dependent manner. *Proceedings of the National Academy of Sciences*, 2002. **99**(20): p. 12600.

155. Porter, J.R., T.T. Ruckh, and K.C. Popat, Bone tissue engineering: A review in bone biomimetics and drug delivery strategies. *Biotechnology Progress*, 2009. **25**(6): p. 1539-1560.

156. McCoy, R.J., C. Jungreuthmayer, and F.J. O'Brien, Influence of flow rate and scaffold pore size on cell behavior during mechanical stimulation in a flow perfusion bioreactor. *Biotechnology and Bioengineering*, 2012. **109**(6): p. 1583-1594.

157. Wendt, D., et al., Oscillating perfusion of cell suspensions through three-dimensional scaffolds enhances cell seeding efficiency and uniformity. *Biotechnology and Bioengineering*, 2003. **84**(2): p. 205-214.

158. Xu, J., et al., Deaths: Final Data for 2016. *National Vital Statistics Report*, 2018. **67**(5): p. 1-76.

159. Benjamin, E.J., et al., Heart Disease and Stroke Statistics—2017 Update: A Report From the American Heart Association. *Circulation*, 2017. **135**(10): p. e146-e603.

160. Johnson, S., et al., Review of Mechanical Testing and Modelling of Thrombus Material for Vascular Implant and Device Design. *Annals of Biomedical Engineering*, 2017. **45**(11): p. 2494-2508.

161. Stalker, T.J., et al., Hierarchical organization in the hemostatic response and its relationship to the platelet-signaling network. *Blood*, 2013. **121**(10): p. 1875.

162. Falati, S., et al., Real-time in vivo imaging of platelets, tissue factor and fibrin during arterial thrombus formation in the mouse. *Nature Medicine*, 2002. **8**: p. 1175.

163. Flaumenhaft, R., Thrombus formation reimagined. *Blood*, 2014. **124**(11): p. 1697-1698.

164. Fogelson, A.L. and K.B. Neeves, Fluid Mechanics of Blood Clot Formation. *Annual review of fluid mechanics*, 2015. **47**: p. 377-403.

165. Wang, W.W. and M.R. King, Multiscale Modeling of Platelet Adhesion and Thrombus Growth. *Annals of Biomedical Engineering*, 2012. **40**(11): p. 2345-2354.

166. Chueh, J.Y., et al., Mechanical Characterization of Thromboemboli in Acute Ischemic Stroke and Laboratory Embolus Analogs. *American Journal of Neuroradiology*, 2011. **32**(7): p. 1237.

167. Teng, Z., et al., Layer- and Direction-Specific Material Properties, Extreme Extensibility and Ultimate Material Strength of Human Abdominal Aorta and Aneurysm: A Uniaxial Extension Study. *Annals of Biomedical Engineering*, 2015. **43**(11): p. 2745-2759.

168. Gasser, T.C., et al., Failure properties of intraluminal thrombus in abdominal aortic aneurysm under static and pulsating mechanical loads. *Journal of Vascular Surgery*, 2008. **48**(1): p. 179-188.

169. O′Leary, S.A., et al., The biaxial mechanical behaviour of abdominal aortic aneurysm intraluminal thrombus: Classification of morphology and the determination of layer and region specific properties. *Journal of Biomechanics*, 2014. **47**(6): p. 1430-1437.

170. Lee, Y.U., et al., Histological and Biomechanical Changes in a Mouse Model of Venous Thrombus Remodeling. *Biorheology*, 2015. **52**(3): p. 235-245.

171. van Dam, E.A., et al., Determination of linear viscoelastic behavior of abdominal aortic aneurysm thrombus. *Biorheology*, 2006. **43**(6): p. 695-707.

172. van Kempen, T.H.S., et al., A constitutive model for developing blood clots with various compositions and their nonlinear viscoelastic behavior. *Biomechanics and Modeling in Mechanobiology*, 2016. **15**: p. 279-291.

173. Slaboch, C.L., et al., Mechano-rheological properties of the murine thrombus determined via nanoindentation and finite element modeling. *Journal of the Mechanical Behavior of Biomedical Materials*, 2012. **10**: p. 75-86.

174. Chih-Chung, H., C. Pay-Yu, and S. Cho-Chiang, Estimating the viscoelastic modulus of a thrombus using an ultrasonic shear-wave approach. *Medical Physics*, 2013. **40**(4): p. 042901.

175. Xie, H., et al., Correspondence of ultrasound elasticity imaging to direct mechanical measurement in aging DVT in rats. *Ultrasound in Medicine & Biology*, 2005. **31**(10): p. 1351-1359.

176. Mfoumou, E., et al., Time-dependent hardening of blood clots quantitatively measured in vivo with shear-wave ultrasound imaging in a rabbit model of venous thrombosis. *Thrombosis Research*, 2014. **133**(2): p. 265-271.

177. Topalov, N.N., et al., Two Types of Procoagulant Platelets Are Formed Upon Physiological Activation and Are Controlled by Integrin alpha(IIb) beta(III). *Arteriosclerosis, Thrombosis, and Vascular Biology*, 2012. **32**(10): p. 2475-2483.

178. Ruf, A. and H. Patscheke, Flow Cytometric Detection of Activated Platelets: Comparison of Determining Shape Change, Fibrinogen Binding, and P-Selectin Expression. *Seminars in Thrombosis and Hemostasis*, 1995. **21**(2): p. 146-151.

179. Chatterjee, M.S., et al., Pairwise agonist scanning predicts cellular signaling responses to combinatorial stimuli. *Nature Biotechnology*, 2010. **28**(7): p. 727-U1737.

180. Bark, D., A. Para, and D. Ku, Correlation of thrombosis growth rate to pathological wall shear rate during platelet accumulation. *Biotechnology and Bioengineering*, 2012. **109**(10): p. 2642-2650.

181. Wu, W.-T., et al., Multi-Constituent Simulation of Thrombus Deposition. *Scientific Reports*, 2017. **7**: p. 42720.

182. Bajd, F. and I. Serša, Mathematical Modeling of Blood Clot Fragmentation During Flow-Mediated Thrombolysis. *Biophysical Journal*, 2013. **104**(5): p. 1181-1190.

183. Tolouei, E., et al., Effect of Hemodynamic Forces on Platelet Aggregation Geometry. *Annals of Biomedical Engineering*, 2011. **39**(5): p. 1403-1413.

184. Tosenberger, A., et al., Modelling of platelet–fibrin clot formation in flow with a DPD–PDE method. *Journal of Mathematical Biology*, 2016. **72**(3): p. 649-681.

185. Yazdani, A., et al., A General Shear-Dependent Model for Thrombus Formation. *PLOS Computational Biology*, 2017. **13**(1): p. e1005291.

186. Pinar, I.P., et al., Methods to Determine the Lagrangian Shear Experienced by Platelets during Thrombus Growth. *PLOS ONE*, 2015. **10**(12): p. e0144860.

187. Xu, Z., et al., A multiscale model of thrombus development. *Journal of The Royal Society Interface*, 2008. **5**(24): p. 705-722.

188. Govindarajan, V., et al., Computational Study of Thrombus Formation and Clotting Factor Effects under Venous Flow Conditions. *Biophysical Journal*, 2016. **110**(8): p. 1869-1885.

189. Xu, S., et al., Model predictions of deformation, embolization and permeability of partially obstructive blood clots under variable shear flow. *Journal of The Royal Society Interface*, 2017. **14**(136).

190. Tokarev, A., et al., *Continuous mathematical model of platelet thrombus formation in blood flow*, in *Russian Journal of Numerical Analysis and Mathematical Modelling*. 2012. p. 191.

191. Kim, O.V., et al., Fibrin networks regulate protein transport during thrombus development. *PLOS Computational Biology*, 2013. **9**(6): p. e1003095.

192. Hiroki, K., et al., A three-dimensional particle simulation of the formation and collapse of a primary thrombus. *International Journal for Numerical Methods in Biomedical Engineering*, 2010. **26**(3-4): p. 488-500.

193. Skorczewski, T., Lindsay C. Erickson, and A.L. Fogelson, Platelet Motion near a Vessel Wall or Thrombus Surface in Two-Dimensional Whole Blood Simulations. *Biophysical Journal*, 2013. **104**(8): p. 1764-1772.

194. Pivkin, I.V., P.D. Richardson, and G. Karniadakis, Blood flow velocity effects and role of activation delay time on growth and form of platelet thrombi. *Proceedings of the National Academy of Sciences of the United States of America*, 2006. **103**(46): p. 17164-17169.

195. Wang, W., N.A. Mody, and M.R. King, Multiscale model of platelet translocation and collision. *Journal of Computational Physics*, 2013. **244**: p. 223-235.

196. Flamm, M.H., et al., Multiscale prediction of patient-specific platelet function under flow. *Blood*, 2012. **120**(1): p. 190-198.

197. Dolan, A.T. and S.L. Diamond, Systems modeling of Ca(2+) homeostasis and mobilization in platelets mediated by IP3 and store-operated Ca(2+) entry. *Biophysical Journal*, 2014. **106**(9): p. 2049-2060.

198. Taylor, J.O., et al., In Vitro Quantification of Time Dependent Thrombus Size Using Magnetic Resonance Imaging and Computational Simulations of Thrombus Surface Shear Stresses. *Journal of Biomechanical Engineering*, 2014. **136**(7): p. 071012-071012-11.

199. Colace, T., R. Muthard, and S.L. Diamond, Thrombus growth and embolism on tissue factor-bearing collagen surfaces under flow: Role of thrombin with and without fibrin. *Arteriosclerosis, Thrombosis, and Vascular Biology*, 2012. **32**(6): p. 1466-1476.

200. Wang, W., et al., Analysis of early thrombus dynamics in a humanized mouse laser injury model. *Biorheology*, 2014. **51**(1): p. 3-14.

201. Welsh, J.D., et al., A systems approach to hemostasis: 1. The interdependence of thrombus architecture and agonist movements in the gaps between platelets. *Blood*, 2014. **124**(11): p. 1808-1815.

202. Borders, J.L. and H.J. Granger, An Optical Doppler Intravital Velocimeter. *Microvascular Research*, 1984. **27**(1): p. 117-127.

203. Granger, D.N., et al., Leukocyte Adherence to Venular Endothelium during Ischemia-Reperfusion. *American Journal of Physiology*, 1989. **257**(5): p. G683-G688.

204. Davis, M.J., Determination of Volumetric Flow in Capillary Tubes Using an Optical Doppler-Velocimeter. *Microvascular Research*, 1987. **34**(2): p. 223-230.

205. Schindelin, J., et al., Fiji: an open-source platform for biological-image analysis. *Nature Methods*, 2012. **9**: p. 676.

206. Thevenaz, P., U.E. Ruttimann, and M. Unser, A pyramid approach to subpixel registration based on intensity. *IEEE Transactions on Image Processing*, 1998. **7**(1): p. 27-41.

207. Li, K., *K. Li, "The image stabilizer plugin for ImageJ*. 2008.

208. Windberger, U., et al., Whole blood viscosity, plasma viscosity and erythrocyte aggregation in nine mammalian species: reference values and comparison of data. *Experimental Physiology*, 2003. **88**(3): p. 431-440.

209. Merrill, E.W. and G.A. Pelletie, Viscosity of Human Blood - Transition from Newtonian to Non-Newtonian. *Journal of Applied Physiology*, 1967. **23**(2): p. 178-182.

210. Kim, M.B. and I.H. Sarelius, Distributions of wall shear stress in venular convergences of mouse cremaster muscle. *Microcirculation*, 2003. **10**(2): p. 167-178.

211. Lipowsky, H.H., Microvascular rheology and hemodynamics. *Microcirculation*, 2005. **12**(1): p. 5-15.

212. Desjardins, C. and B.R. Duling, Microvessel Hematocrit - Measurement and Implications for Capillary Oxygen-Transport. *American Journal of Physiology*, 1987. **252**(3): p. H494-H503.

213. Sriram, K., M. Intaglietta, and D.M. Tartakovsky, Non-Newtonian Flow of Blood in Arterioles: Consequences for Wall Shear Stress Measurements. *Microcirculation (New York, N.Y. : 1994)*, 2014. **21**(7): p. 628-639.

214. Kheyfets, V.O., et al., Patient-Specific Computational Modeling of Blood Flow in the Pulmonary Arterial Circulation. *Computer Methods and Programs in Biomedicine*, 2015. **120**(2): p. 88-101.

215. Nesbitt, W.S., et al., A shear gradient-dependent platelet aggregation mechanism drives thrombus formation. *Nature Medicine*, 2009. **15**(6): p. 665-U146.

216. Sakariassen, K.S., et al., Shear-induced platelet activation and platelet microparticle formation in native human blood. *Thrombosis Research*, 1998. **92**(6): p. S33-S41.

217. Holme, P.A., et al., Shear-induced platelet activation and platelet microparticle formation at blood flow conditions as in arteries with a severe stenosis. *Arteriosclerosis Thrombosis and Vascular Biology*, 1997. **17**(4): p. 646-653.

218. Westerhof, N., N. Stergiopulos, and M.I.M. Noble, Snapshots of Hemodynamics. 2 ed. 2010, USA: Springer US. XIV, 272.

219. Lipowsky, H.H., S. Kovalcheck, and B.W. Zweifach, The distribution of blood rheological parameters in the microvasculature of cat mesentery. *Circulation Research*, 1978. **43**(5): p. 738-749.

220. Taylor, J.O., et al., Development of a computational model for macroscopic predictions of device-induced thrombosis. *Biomechanics and Modeling in Mechanobiology*, 2016. **15**(6): p. 1713-1731.

221. Celi, A., et al., Thrombus formation: direct real-time observation and digital analysis of thrombus assembly in a living mouse by confocal and widefield intravital microscopy. *Journal of Thrombosis and Haemostasis*, 2003. **1**(1): p. 60-68.

222. Brass, L.F., et al., Regulating thrombus growth and stability to achieve an optimal response to injury. *Journal of Thrombosis and Haemostasis*, 2011. **9**(s1): p. 66-75.

223. Tomaiuolo, M., et al., A systems approach to hemostasis: 2. Computational analysis of molecular transport in the thrombus microenvironment. *Blood*, 2014. **124**(11): p. 1816-1823.

224. Zhu, L., et al., Regulated surface expression and shedding support a dual role for semaphorin 4D in platelet responses to vascular injury. *Proceedings of the National Academy of Sciences of the United States of America*, 2007. **104**(5): p. 1621-1626.

225. Ferroni, P., et al., Soluble P-selectin as a marker of in vivo platelet activation. *Clinica Chimica Acta*, 2009. **399**(1-2): p. 88-91.

226. Chung, I., et al., Soluble, platelet-bound, and total P-selectin as indices of platelet activation in congestive heart failure. *Annals of Medicine*, 2009. **41**(1): p. 45-51.

227. Semenov, A.V., et al., Soluble P-selectin - A marker of platelet activation and vessel wall injury. Increase of soluble P-selectin in the blood plasma of patients with myocardial infarction, massive atherosclerosis and primary pulmonary hypertension. *Terapevticheskii Arkhiv*, 2000. **72**(4): p. 15-20.

228. Kiskin, N.I., et al., Protein mobilities and P-selectin storage in Weibel-Palade bodies. *Journal of Cell Science*, 2010. **123**(17): p. 2964-2975.

229. Blann, A.D., S.K. Nadar, and G.Y.H. Lip, The adhesion molecule P-selectin and cardiovascular disease. *European Heart Journal*, 2003. **24**(24): p. 2166-2179.

230. Collins, P.W., et al., Von Willebrand Factor Release and P-Selectin Expression Is Stimulated by Thrombin and Trypsin but not IL-1 in Cultured Human Endothelial Cells. *Thrombosis and Haemostasis*, 1993. **70**(02): p. 346-350.

231. Stalker, T.J., et al., A systems approach to hemostasis: 3. Thrombus consolidation regulates intrathrombus solute transport and local thrombin activity. *Blood*, 2014. **124**(11): p. 1824-1831.